

REF ID: A6566-MA  
DUPLICATE COPY

ARO 26656.6-MA

(2)

# Modeling, Estimation, and Pattern Analysis of Random Texture on 3-D Surfaces

Yoonsik Choe  
R. L. Kashyap

DTIC  
ELECTE  
FEB 25 1991  
S D D

TR-EE-91-4  
January 1991

DISTRIBUTION STATEMENT A  
Approved for public release  
Distribution Unlimited

School of Electrical Engineering  
Purdue University  
West Lafayette, Indiana 47907

91 2 15 165

**MODELING, ESTIMATION, AND PATTERN ANALYSIS  
OF RANDOM TEXTURE ON 3-D SURFACE**

**Technical Report**

**Yoonsik Choe and R.L. Kashyap**

**U.S. Army Research Office**

**Contract DAAL03-89K-0032**

**School of Electrical Engineering  
Purdue University  
West Lafayette, IN 47907**

**Approved for Technical Release**

**Distribution Unlimited**



Accession For	
NTIS	<input checked="" type="checkbox"/>
CRA&I	<input type="checkbox"/>
DRIC	<input type="checkbox"/>
TAB	<input type="checkbox"/>
Unpublished	<input type="checkbox"/>
Justification	
By	
Distribution /	
Availability Codes	
Dist	Availability for Special
A-1	

01 2 1 100

## ABSTRACT

To recover 3-D structure from a shaded and textural surface image involving textures, neither the Shape-from-shading nor the Shape-from-texture analysis is enough, because both radiance and texture information coexist within the scene surface. A new 3-D texture model is developed by considering the scene image as the superposition of a smooth shaded image and a random texture image. To describe the random part, the orthographical projection is adapted to take care of the non-isotropic distribution function of the intensity due to the slant and tilt of a 3-D texture surface, and the Fractional Differencing Periodic (FDP) model is chosen to describe the random texture, because this model is able to simultaneously represent the coarseness and the pattern of the 3-D texture surface, and enough flexible to synthesize both long-term and short-term correlation structures of random texture. Since the object is described by the model involving several free parameters and the values of these parameters are determined directly from its projected image, it is possible to extract 3-D information and texture pattern directly from the image without any pre-processing. Thus, the cumulative error obtained from each pre-processing can be minimized. For estimating the parameters, a hybrid method which uses both the least square and the maximum likelihood estimates is applied and the estimation of parameters and the synthesis are done in frequency domain. Among the texture pattern features which can be obtained from a single surface image, Fractal scaling parameter plays a major role for classifying and/or segmenting the different texture

patterns tilted and slanted due to the 3-dimensional rotation, because of its rotational and scaling invariant properties. Also, since the Fractal scaling factor represents the coarseness of the surface, each texture pattern has its own Fractal scale value, and particularly at the boundary between the different textures, it has relatively higher value to the one within a same texture. Based on these facts, a new classification method and a segmentation scheme for the 3-D rotated texture patterns are developed.

## TABLE OF CONTENTS

	Page
LIST OF TABLES .....	viii
LIST OF FIGURES .....	ix
 CHAPTER 1 - INTRODUCTION AND OVERVIEW.....	 1
1.1. Introduction .....	1
1.2. Modeling Of A Surface Image .....	3
1.3. Fractional Differencing Model .....	4
1.4. Shape From A Shaded And Textured Surface Image .....	5
1.5. Classification Of 3-D Rotated Textures.....	6
1.6. Organization Of The Thesis .....	7
 CHAPTER 2 - MODELING OF A SURFACE IMAGE .....	 9
2.1. Introduction .....	9
2.2. Shape-From-Shading .....	10
2.2.1. Estimation Of Illumination Direction.....	13
2.2.1.1. Pentland's Method .....	13
2.2.1.2. Lee's Method .....	15
2.2.2. Estimation Of Surface Orientation .....	17
2.2.2.1. Horn And Brooks's Method .....	17
2.2.2.2. Chellappa And Frankot's Method ....	18
2.2.2.3. Pentland's Method .....	19
2.2.3. Simulation Results .....	21
2.3. Shape-From-Texture.....	33
2.3.1. Projection .....	34
2.3.1.1. Orthographical Projection.....	35
2.3.1.2. Perspective Projection .....	38

## ABSTRACT

To recover 3-D structure from a shaded and textural surface image involving textures, neither the Shape-from-shading nor the Shape-from-texture analysis is enough, because both radiance and texture information coexist within the scene surface. A new 3-D texture model is developed by considering the scene image as the superposition of a smooth shaded image and a random texture image. To describe the random part, the orthographical projection is adapted to take care of the non-isotropic distribution function of the intensity due to the slant and tilt of a 3-D texture surface, and the Fractional Differencing Periodic (FDP) model is chosen to describe the random texture, because this model is able to simultaneously represent the coarseness and the pattern of the 3-D texture surface, and enough flexible to synthesize both long-term and short-term correlation structures of random texture. Since the object is described by the model involving several free parameters and the values of these parameters are determined directly from its projected image, it is possible to extract 3-D information and texture pattern directly from the image without any pre-processing. Thus, the cumulative error obtained from each pre-processing can be minimized. For estimating the parameters, a hybrid method which uses both the least square and the maximum likelihood estimates is applied and the estimation of parameters and the synthesis are done in frequency domain. Among the texture pattern features which can be obtained from a single surface image, Fractal scaling parameter plays a major role for classifying and/or segmenting the different texture

patterns tilted and slanted due to the 3-dimensional rotation, because of its rotational and scaling invariant properties. Also, since the Fractal scaling factor represents the coarseness of the surface, each texture pattern has its own Fractal scale value, and particularly at the boundary between the different textures, it has relatively higher value to the one within a same texture. Based on these facts, a new classification method and a segmentation scheme for the 3-D rotated texture patterns are developed.

## Page

## APPENDICES

Appendix A.....	158
Appendix B.....	160
Appendix C.....	162
VITA.....	166

## LIST OF TABLES

Table	Page
4.1. True parameter values and the estimated parameter values of the projected Fractional Differencing Periodic model (4.2.3.2.6): The random noise sequence as input data for each synthesized texture patch of size 64×64 was generated from white Gaussian noise with zero mean and variance 10. Estimated values were obtained from these synthesized images by equations (4.3.1.8)-(4.3.1.13).....	96
5.1. The sample mean and variance of parameter $c$ , $\omega_1$ , $\omega_2$ : 16 64×64 sample image data are taken for each different texture classes, and the parameter values are extracted from the first and second-order fractional differencing models (5.3.1-2).....	127
5.2. Database of the first level of classification. $\hat{c}_i$ and $\sigma_i^2$ are the sample mean and the variance of class $i$ , respectively.....	127
5.3. Classification results from the 2-D rotated texture image. (Result indicates the result class after applying 2-level classification method.) .....	129
5.4. Classification results from the orthographically projected texture images. (Result indicates the result class after applying 2-level classification method.) .....	130
5.5. Classification results from the rotated and orthographically projected texture images. (Result indicates the result class after applying 2-level classification method.) .....	132

## LIST OF FIGURES

Figure	Page
2.1. Three Different Directions on 3-D Surface .....	11
2.2. Intensity image of a sphere from the various directions of light source. (a) $\sigma_L = 0.0$ , $\tau_L = 0.0$ (b) $\sigma_L = -0.66$ , $\tau_L = -0.66$ [rad]. (Images are simulated by (2.1.2.1a) and intensity values are normalized between 0 and 255).....	12
2.3. A digitalized tree image sized by 512×512.....	22
2.4. The height function of Figure 2.2: constructed by (a) Horn's method, (b) Frankot's method: Surface orientation for each pixel was obtained from minimizing the cost function (2.2.2.1.1) and (2.2.2.2.2), respectively. ....	23
2.5. A part of the tree image (Figure 2.3) (a) original, (b) Image obtained after convoluting a 5×5 smoothing window to (a), (c) Image obtained after convoluting a 9×9 smoothing window to (a) .....	25
2.6. The height function of Figure 2.5-a: constructed by (a) Horn's method, (b) Frankot's method: Surface orientation for each pixel was obtained from minimizing the cost function (2.2.2.1.1) and (2.2.2.2.2), respectively. ....	26
2.7. The height function of Figure 2.5.-b: constructed by (a) Horn's method, (b) Frankot's method: Surface orientation for each pixel was obtained from minimizing the cost function (2.2.2.1.1) and (2.2.2.2.2), respectively. ....	28
2.8. The height function of Figure 2.5.-c: constructed by (a) Horn's method, (b) Frankot's method: Surface orientation for each pixel was obtained from minimizing the cost function (2.2.2.1.1) and (2.2.2.2.2), respectively. ....	30

Figure	Page
2.9. The height function of Figure 2.5-b, which was constructed by Pentland's method(2.2.2.3.1-5): Closed form solution of the surface orientation was obtained in the frequency domain by the linear approximation method. ....	32
2.10. Coordinate transformation of the orthographic projection (2.3.1.1.4) .....	35
2.11. 2-D grid pattern images: (a) original, (b) Image obtained after projecting the image (Figure 2.10-a) orthographically, with $\sigma = \pi/4$ and $\tau = \pi/8$ in (2.3.1.1.4). (c) Image obtained after projecting the image (Figure 2.10-a) orthographically, with $\sigma = \pi/4$ and $\tau = \pi/8$ in (2.3.1.1.4). ....	37
2.12. Perspective projection.....	38
2.13. Approximation method of perspective projection.....	41
2.14. Synthesized surface shapes over 64×64 sized normal plane patch from (a) A tree image whose surface is covered by the tree bark texture, (b) Pentland's model with the fractal scale $c=0.9$ , (c) Pentland's model with the fractal scale= $1.5$ , (d) 2nd-order AR model with the frequency $\omega_1 = 0.25$ , $\omega_2 = 0.025$ in directions of $m_1, m_2$ , respectively. ....	47
2.15. Surface shapes obtained from Fractional Differencing Periodic model (2.3.2.3.1): (a) Synthesized surface shape over 64×64 sized normal plane patch with the frequency $\omega_1 = 0.25$ , $\omega_2 = 0.025$ and fractal scale $c=1.5$ , $d=0.8$ in direction of $m_1, m_2$ , (b) corresponding image. ....	48
4.1. Superposition of a random and a deterministic functions in 1-D case. ....	70
4.2. 3-D Geometry of the functions $x, y, x', y'$ .....	72
4.3. Sphere images: (a) Height function of a sphere obtained by equation (4.3.2.3) (b) Image obtained by the reflectance map function (4.2.2.3) with $\varepsilon = 100$ (4.3.2), $\sigma_L = -0.66$ , $\tau_L = -0.66$ .....	91

Figure	Page
4.4. Image obtained after projecting texture image orthographically to the sphere surface. (Background texture pattern is generated by Fractional Differencing Periodic model (2.3.2.6) with $\omega_1 = 0.2$ , $\omega_2 = 0.2$ , $c = 0.8$ , $d = 0.8$ ).....	92
4.5. Image of 3-D texture on the surface of a sphere (Image is generated by the composite model (4.3.1) with $\sigma_L = -0.66$ , $\tau_L = -0.66$ )..	93
4.6. 2-D texture images: (a) Image obtained from (4.2.3.2.6) with $\omega_1 = 0.2$ , $\omega_2 = 0.2$ , $c=0.8$ , $d=0.8$ (b) Projected image of the tilted and slanted version of Figure 4.7-a by $-\pi/4$ and $\pi/8$ , respectively.....	95
4.7. Tree images: (a) A 512×512 original image of a part of a tree. (b) A synthesized tree image: Local patch size is 32×32, and each 3-D texture pattern was synthesized by the composite model (4.3.1) with the illumination direction $\sigma_L = -1.3384$ , $\tau_L = -0.0426$ and $\omega_1 = 0.486$ , $\omega_2 = 0.053$ , $c=1.394$ , $d=0.762$ for the random part. 16×16 pixel sized patch was taken from the center of it. The complete image of cylinder (512×512) was obtained by adjoining these 16×16 pixel sized patches. ....	98
5.1. 2-D grid pattern images: (a) Original image, (b) Image obtained after rotating the image (Figure 5.1-a) on the image plane with $\theta = \pi/8$ in (5.2.1), (c) Image obtained after projecting the image (Figure 5.1-a) orthographically, with $\sigma = \pi/4$ and $\tau = \pi/8$ in (5.2.4), (d) Image obtained after projecting the already rotated image (Figure 5.1-b) orthographically, with $\sigma = \pi/4$ and $\tau = \pi/8$ in (5.2.5). ....	105
5.2. Texture pattern images: (a) Original image with $\omega_1 = 0.2$ , $\omega_2 = 0.2$ , and $c=0.8$ in (5.3.2). (b) Image obtained after rotating the image (Figure 5.2-a) on the image plane with $\theta = \pi/4$ in (5.3.1.2). (c) Image obtained after projecting the image (Figure 5.2-a) orthographically, with $\sigma = -\pi/4$ and $\tau = \pi/8$ in (5.3.1.7). (d) Image obtained after projecting the already rotated image (Figure 5.2-b) orthographically, with $\sigma = -\pi/4$ and $\tau = \pi/8$ in (5.3.1.11). ....	114
5.3. Two-level hierarchical classification structure.....	121

Figure	Page
5.4. 256×256 original texture images of training set: (a)grass (b) tree bark (c) straw (d) herringbon weave (e) woolen cloth (f) calf leather (g) beach sand (h) water (i) raffia. ....	125
5.5. 64×64 raffia images rotated by $\theta$ s: (a) $\theta = 20^\circ$ (b) $\theta = 40^\circ$ (c) $\theta = 60^\circ$ (d) $\theta = 80^\circ$ (e) $\theta = 100^\circ$ (f) $\theta = 120^\circ$ (g) $\theta = 140^\circ$ (h) $\theta = 160^\circ$ (i) $\theta = 180^\circ$ .....	128
5.6. 64×64 herringbon texture images projected orthographically from the various tilted slanted texture surface ( $\tau$ , $\sigma$ are the tilted and slanted angles): (a) $\tau = 0^\circ$ , $\sigma = 15^\circ$ (b) $\tau = 0^\circ$ , $\sigma = 30^\circ$ (c) $\tau = 0^\circ$ , $\sigma = 45^\circ$ (d) $\tau = 45^\circ$ , $\sigma = 15^\circ$ (e) $\tau = 45^\circ$ , $\sigma = 30^\circ$ (f) $\tau = 45^\circ$ , $\sigma = 45^\circ$ .....	130
5.7. 64×64 straw texture images rotated and projected orthographically from the various tilted and slanted texture surface ( $\theta$ , $\tau$ , $\sigma$ are the rotated, tilted and slanted angles.): (a) $\theta = 0^\circ$ , $\tau = 0^\circ$ , $\sigma = 15^\circ$ (b) $\theta = 45^\circ$ , $\tau = 0^\circ$ , $\sigma = 30^\circ$ (c) $\theta = 90^\circ$ , $\tau = 0^\circ$ , $\sigma = 45^\circ$ (d) $\theta = 0^\circ$ , $\tau = 45^\circ$ , $\sigma = 15^\circ$ (e) $\theta = 45^\circ$ , $\tau = 45^\circ$ , $\sigma = 30^\circ$ (f) $\theta = 90^\circ$ , $\tau = 45^\circ$ , $\sigma = 45^\circ$ .....	132

## CHAPTER 1

### INTRODUCTION AND OVERVIEW

#### 1.1. Introduction

An important task in computer vision is the recovery of 3-D scene information from single 2-D images. However, this is an ill-posed problem [13, 178], because we have only 2-D information but try to extract 3-D information from it. Therefore, we need additional information for this missing dimension to recover 3-D scene information. To date, researchers have suggested two different ways to handle this lack of information. The first one is the use of shading information in the image [30, 31, 73, 75, 100, 144, 172]. Shading information tells us the direction of the light source and the surface orientation of the object surface. Thus, by formulating the reflectance map function which shows scene radiance as a function of the surface gradient and the distribution of light sources, we can extract 3-D surface information from image data. The second method is the use of texture information [6, 82, 109, 135, 207, 221]. Since texture gradients behave like intensity gradients, the shape of a surface can be inferred from the pattern of a texture on the surface by applying statistical texture analysis.

However, for describing a natural scene image, each of the above approaches have their own limitations. Shading information is meaningful only under the assumption that the surface is smooth enough to have clear radiance information, even

though this situation is rarely encountered in practice. Thus, instead of having clear radiance information, the scene image has texture pattern information due to the complexity of the surface in most cases. This encourages us to study the texture pattern of a 3-D surface. Therefore, the modeling and analysis of texture patterns which contain 3-D information of the surfaces will be the main focus of this thesis.

3-D texture analysis involves at least the several following difficulties. First, for the recovery of 3-D shape from the natural scene, a texture model itself will not be enough to represent the whole surface, because texture analysis requires the surface to be relatively complex to have a statistical property. However, some parts of the surface may not contain clear information about the texture pattern due to dark shading or bright radiance. In other words, we may have a situation such that the radiance information is more dominant than the texture information. Therefore, our model should have an ability to handle both the texture and radiance information at the same time. Second, since the observed texture image is actually the image obtained by projecting the surface image to the image plane, this projected random texture pattern does not have the stationary property any more, even though the original surface normal image can be represented by a stationary random texture pattern. Thus, the conventional 2-D texture models under the assumption of stationarity can not be used. Third, for the classification and texture segmentation purpose, our model should have a 3-D rotational invariant property, since the observed texture pattern may have various looks depending on the viewer's direction. Thus, the classification and/or segmentation scheme for the 3-D rotated texture pattern should have the flexibility to treat different looking textures as being the same without losing the accuracy of the processes.

In this thesis, to solve the difficulties discussed above, a composite model of Shape-from-shading and Shape-from-texture is developed to represent a 3-D surface

image considering the scene image as the superposition of a smooth shaded image and a random texture image. The orthographical projection is adapted to take care of the non-isotropic distribution function due to the slant and tilt of a 3-D texture surface, and the Fractional Differencing Periodic model is chosen because this model is able to simultaneously represent the coarseness and the pattern of the 3-D texture surface with the fractional differencing parameters  $c$ ,  $d$  and the frequency parameters  $\omega_1$ ,  $\omega_2$ . For the classification and segmentation purpose, these fractional differencing parameters play an important role, because those parameters are known to be rotational and scaling invariant. Thus, combining these parameters and directional frequency parameters in the fractional differencing periodic function, we can have the flexibility to handle the rotated and projected texture pattern and the accuracy of the classification. For estimating the parameters, a hybrid method which uses both the least square and the maximum likelihood estimates is applied and the estimation and the synthesis are done in frequency domain.

## 1.2. Modeling Of A Surface Image

Modeling of a 3-D surface image can be broken down into two main categories, Shape-from-shading and Shape-from-texture. The Shape-from-shading model uses the reflectance map which shows scene radiance as a function of the surface gradient and the distribution of light sources to extract 3-D surface information from image data [30,99]. On the other hand, the Shape-from-texture model uses the texture pattern instead of shading to extract 3-D structure [82,109,135]. Since texture gradients behave like intensity gradients, the shape of a surface can be inferred from the pattern of a texture on the surface by applying statistical texture analysis. However, for describing a natural scene image, each of the above approaches has its

own limitation. The Shape-from-shading model is applicable only under the assumption that the surface is smooth enough to have clear radiance information, while the Shape-from-texture model requires the surface to be relatively complex so that texture information can be extracted. Thus, neither model is suitable to represent a natural scene, because both radiance and texture information coexist within the surface of a natural scene. Therefore, a robust technique is needed to handle this shortcoming. Recently, the fractal scaling parameter was introduced to measure the coarseness of the surface, and applied to represent the natural scene surface [47, 132, 151, 173]. However, this fractal model is also not enough to represent the real 3-D texture image, because even though two surfaces are estimated to have the same fractal scales, these surfaces can have different texture patterns. Therefore, in this thesis, the Fractional Differencing Periodic model is chosen to represent the 3-D surface image, because this model is able to simultaneously represent the coarseness and the pattern of the 3-D texture surface with the fractional differencing parameters  $c$ ,  $d$  and the frequency parameters  $\omega_1$ ,  $\omega_2$ .

### 1.3. Fractional Differencing Model

As mentioned previously, the fractional differencing model has an ability to simultaneously represent the coarseness [175] and the pattern of the 3-D texture surface with the fractional differencing parameters  $c$ ,  $d$  and the frequency parameters  $\omega_1$ ,  $\omega_2$ . Also, it has the property of being flexible enough to synthesize both long-term and short-term correlation structures of random texture depending on the values of the fractional differencing parameters [89, 101]. For estimating the parameters, comparing with the fractional Brownian random process model [151], the fractional differencing model has a simple estimation scheme sharing the same properties of the

fractional Brownian process, because while the fractional Brownian process is a continuous process which follows a certain probability distribution, the fractional differencing model is a discrete process which has a linear function of parameters. A hybrid method which uses both the least square and the maximum likelihood estimates is applied and the estimation and the synthesis are done in the frequency domain [67].

#### **1.4. Shape From A Shaded And Textured Surface Image**

In this thesis, a composite model of Shape-from-shading and Shape-from-texture is developed to represent a 3-D surface image considering the scene image as the superposition of a smooth shaded image and a random texture image, that is, the deterministic function  $x(l_1, l_2)$  and the random function  $y(l_1, l_2)$ . Then, the orthographical projection is adapted to take care of the non-isotropic distribution function due to the slant and tilt of a 3-D texture surface. Thus, the Orthographically Projected Fractional Differencing Periodic (OPFDP) model is chosen because this model is able to simultaneously represent the coarseness and the 3-D rotated pattern of the surface with the fractional differencing parameters  $c, d$ , the frequency parameters  $\omega_1, \omega_2$ , and the relationship between different directions of 3-D surface. Since the object is described by a model involving several free parameters and the values of these parameters are determined directly from its projected image, it is possible to extract 3-D information and texture pattern directly from the given intensity values of the image without any pre-processing. Thus, the cumulative error obtained from each pre-processing can be minimized. For estimating the parameters, a hybrid method which uses both the least square and the maximum likelihood estimates is applied and the estimation and the synthesis are done in frequency domain based on the local

patch analysis. By using this model, the integrability problem which might occur in spatial domain analysis can be avoided, because only one inverse Fourier transform needs to be taken at the end of the procedure to get the whole image.

### **1.5. Classification Of 3-D Rotated Textures**

The classification problem can be stated as an allocation of observed texture image data to the one of the pre-defined texture classes. These texture classes can be described by texture features, and then texture features can be the parameters in stochastic model [46, 53, 92], or structural model [142, 216]. Thus, the key step in the classification process is the choice of a set of features which can reduce the dimension of the image data to a computationally reasonable amount of data. The features should be simple and easy to extract from the given data while preserving the classifying information present in the data.

Most classification schemes which have been suggested to date are under the assumption that the test sample data possesses the same surface orientation as the training sample data. Thus, if the orientation of test image is different from the training sample data, for example, in case of a rotated image, the classification performs poorly. This reduces the flexibility of those classification schemes. However, most natural texture images which we can encounter in practice are representing the texture on the 3-D surface, thus, the observed image is a projected surface image onto the 2-D image plane with a 2-D rotated, or 3-D slanted and tilted texture pattern. Therefore, sometimes it is desirable for the classification scheme to have the flexibility that it can classify even rotated or scaled texture to the original class of it. This is a good indication why it is so important to have the rotational and scaling invariant features in our model. In this thesis, a classification method which

can handle arbitrary 3-D rotated samples of textures is developed, i.e., the accuracy of classification is not affected by the 3-D rotation of the test texture. This classification scheme is based on a two-level hierarchical structure. In the first level, a 3-D rotational invariant feature, fractal scale  $c$ , is extracted from the first-order fractional differencing model by applying a least-square estimation method, and this feature is used to classify the test texture image to a class whose members are sharing a similar value of fractal scale. And in the second level, the members of the class are further classified to the final desired subclasses with other texture pattern features,  $\omega_1$  and  $\omega_2$ , which are extracted from the second-order projected fractional differencing model by applying a hybrid method of the least-square estimation and the maximum likelihood estimation. As a result, this multi-level classification scheme saves a reasonable amount of processing time without losing the accuracy of the classification.

## **1.6. Organization Of The Thesis**

Various applications of the Fractional Differencing model have been investigated to represent 3-D texture pattern through this thesis. An important aim of this study is to develop the mathematical model suitable for the 3-D surface image which the radiance and texture information coexist in. The Orthographically Projected Fractional Differencing (OPFD) model developed here performs very well to represent the texture pattern on the 3-D surface, because of the rotational and scaling invariant parameters in it. This rotational and scaling invariant property of these parameters has been successfully applied to segment or classify the rotated and slanted texture plane in the rest of the chapters.

The organization of the thesis is as follows. In chapter 2, two different categories of 3-D surface model, Shape-from-shading and Shape-from-texture, are discussed, and several typical methods of each categories are compared with their simulation results. Two projection methods, orthographical and perspective projection, are also presented to represent the distortion due to the tilt and the slant of the surface. In chapter 3, the Fractional Differencing model suggested in chapter 2 to represent the 3-D texture is discussed in detail, and its estimation scheme based on the Least-Square and Maximum likelihood estimation methods is presented. Chapter 4 presents a composite model of Shape-from-shading and Shape-from-texture to extract the 3-D structure from the surface image which contains the radiance information and the texture information at the same time. This suggested model is directly applied to the given image without any pre-processing, and as a result of this, the errors which might result from each pre-processing are not cumulated. In chapter 5, a classification scheme of *the 3-D rotated textures* is developed based on the fractal scale. This fractal scale is known to be a rotational and scaling invariant parameter, and can be extracted by fitting the given tilted or slanted texture image to the proposed Fractional Differencing model. A multi-level structure of the classification structure is also introduced to reduce the processing time. Finally in chapter 7, the conclusion of this study and the suggested future research are presented.

## CHAPTER 2

### MODELING OF A SURFACE IMAGE

#### 2.1. Introduction

Modeling of a 3-D surface image can be broken down into two main categories, Shape-from-shading and Shape-from-texture. The Shape-from-shading model uses the reflectance map which shows scene radiance as a function of the surface gradient and the distribution of light sources to extract 3-D surface information from image data [30, 73, 75, 100, 144, 172]. On the other hand, Shape-from-texture model uses the texture pattern instead of shading to extract 3-D structure [6, 109, 135, 207, 216, 221]. Since texture gradients behave like intensity gradients, the shape of a surface can be inferred from the pattern of a texture on the surface by applying statistical texture analysis. However, for describing a natural scene image, each of the above approaches has its own limitation. The Shape-from-shading model is applicable only under the assumption that the surface is smooth enough to have clear radiance information, while the Shape-from-texture model requires the surface to be relatively complex so that texture information can be extracted. Thus, neither model is suitable to represent a natural scene, because both radiance and texture information coexist within the surface of a natural scene. Therefore, a robust technique is needed to handle this shortcoming. Recently, the fractal scaling parameter was introduced to measure the coarseness of the surface, and applied to represent the natural scene surface [47, 132, 151, 173]. However, this fractal model is also not enough to

represent the real 3-D texture image, because even though two surfaces are estimated to have the same fractal scales, these surfaces can have different texture patterns. Therefore, in this thesis, the Fractional Differencing Periodic model is chosen to represent the 3-D surface image, because this model is able to simultaneously represent the coarseness and the pattern of the 3-D texture surface with the fractional differencing parameters  $c, d$  and the frequency parameters  $\omega_1, \omega_2$ .

## 2.2. Shape-From-Shading

Pioneering work on the inference of shape-from-shading was done by Horn and his co-workers [30, 99, 100]. To extract 3-D shape from a single 2-D image, they used the reflectance map, which shows the intensity of the image as a function of the surface gradient and the illumination direction. (Figure 2.1 shows the relationship between the different directions and angles.)

$$i(l_1, l_2) = \frac{p \cos \tau_L \sin \sigma_L + q \sin \tau_L \sin \sigma_L + \cos \sigma_L}{(p^2 + q^2 + 1)^{1/2}} \triangleq R(p, q) \quad (2.2.1.a)$$

$$= \sin \sigma \cos \tau \cos \tau_L \sin \sigma_L + \sin \sigma \sin \tau \sin \tau_L \sin \sigma_L + \cos \sigma \cos \sigma_L \quad (2.2.1.b)$$

where  $p = \frac{\partial}{\partial l_1} H(l_1, l_2), q = \frac{\partial}{\partial l_2} H(l_1, l_2)$

$R(p, q)$  : Reflectance map function

$H(l_1, l_2)$  : 3-D shape function from the viewing direction.

$\tau, \sigma$  : Tilt, slant of the surface

$\tau_L, \sigma_L$  : Tilt, slant of the illumination direction

Here, the relationship between  $\tau, \sigma$  and  $p, q$  are

$$\tau = \tan^{-1}\left(\frac{q}{p}\right), \quad \sigma = \cos^{-1} \frac{1}{\sqrt{p^2 + q^2 + 1}} \quad (2.2.2.a)$$

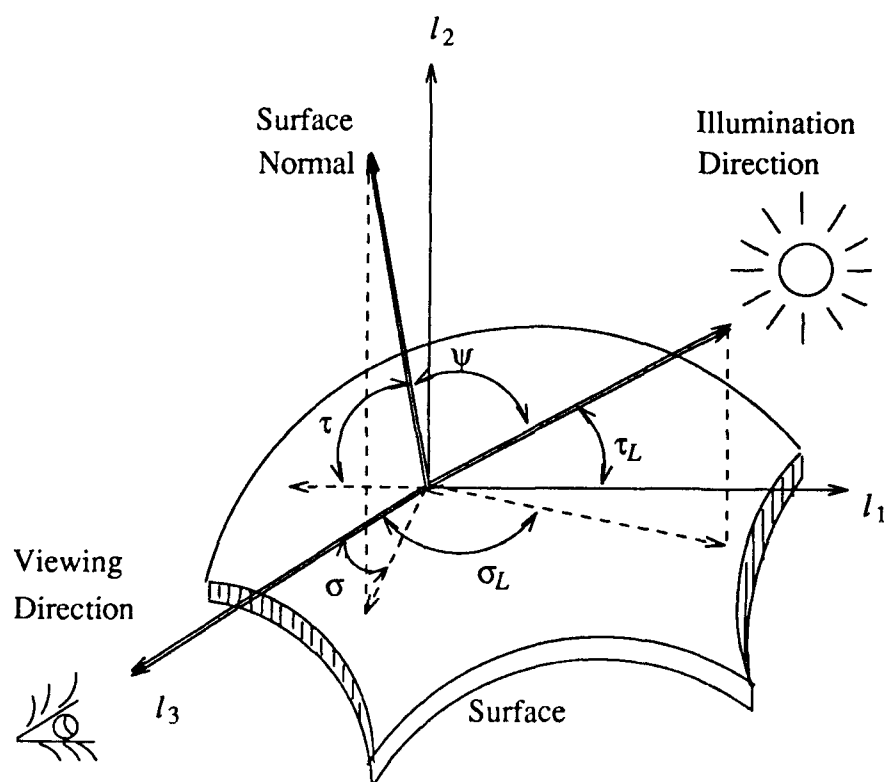


Figure 2.1: Three Different Directions on 3-D Surface

$$p = \tan\sigma\cos\tau, \quad q = \tan\sigma\sin\tau \quad (2.2.2.b)$$

Figure 2.2-a,b were simulated from the equation (2.2.1), assuming that the slope values  $p, q$  in directions of  $l_1, l_2$  and the illumination direction were given.

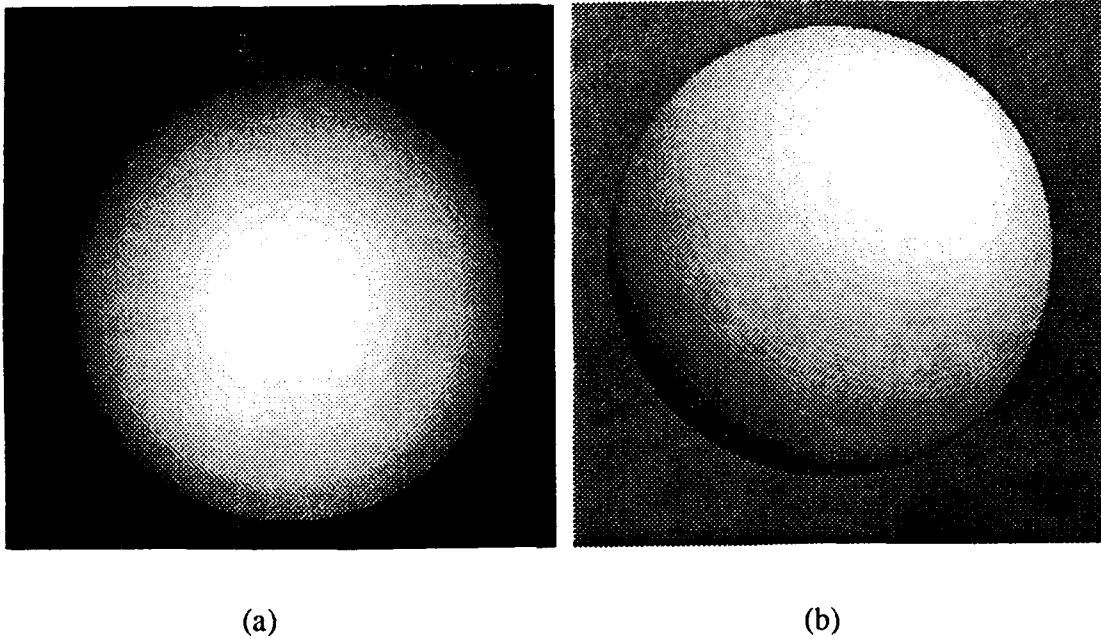


Figure 2.2: Intensity images of a sphere from the various directions of light source. (a)  $\sigma_L = 0.0, \tau_L = 0.0$  (b)  $\sigma_L = -0.66, \tau_L = -0.66$  [rad]. (Images are simulated by (2.1.2.1a) and intensity values are normalized between 0 and 255.)

Construction of 3-D shape can be achieved by solving  $p, q$  in terms of  $i(l_1, l_2)$  at each point, and integrating those values. However, the final integrated shape can be different from the original shape, due to the cumulation of estimation errors. To avoid this type of error, Horn and Brooks [100] developed a calculus of variation method to estimate the surface orientation values, and Pentland [172] suggested local shape analysis which deals with the only local areas instead of a whole image. However, Pentland's technique has severe trouble in integrating all local areas. Recently, Pentland [169] developed another technique to solve the integrability problem. He

suggested analysis in the frequency domain, instead of in the spatial domain. By using this method, the integrability problem can be avoided, because only one inverse Fourier transform needs to be taken at the end of procedure. However, since the calculation of convolution is required in the frequency domain to handle simple multiplication operation of spatial domain, calculation will be complicated. Horn and Brooks' method was improved by Frankot and Chellappa [76] recently, by adding one more constraint of the integrability in addition to the smoothness constraint. The estimation error and the integrability problem can be handled by the image model suggested in this thesis, because our model has a constraint which is from the texture pattern and is analyzed in frequency domain.

### **2.2.1. Estimation Of Illumination Direction**

The first step in estimating local surface orientation is the determination of the illumination direction for the surface,  $L$ , and the constant  $\lambda\mu$  for a particular estimation neighborhood. Estimation methods of illumination direction  $L$  were suggested by Pentland [171], and C-H Lee [144] in different ways.

#### **2.2.1.1. Pentland's Method**

Pentland's approach was based under the assumption that the surface normal of each local patch is isotropically distributed within a scene. Assuming that the distribution of the surface normal is known and the intensity value is measurable for different directions within the image, one could estimate the illumination direction  $L$  using a least square estimation procedure [171]. The solution of this approach follow.

**Theorem 2.1:** Let  $di(l_1, l_2)$  be the first derivative of image intensity at a particular point in the direction  $(dl_1, dl_2)$ , and  $\hat{di}_j$  be the average value of  $di$  over the  $j$ -th patch in direction  $(dl_{1j}, dl_{2j})$ . Then,

$$\begin{bmatrix} \hat{dx}_1 \\ \hat{dx}_2 \\ \vdots \\ \hat{dx}_n \end{bmatrix} = \begin{bmatrix} dl_{11} & dl_{21} \\ dl_{12} & dl_{22} \\ \vdots & \vdots \\ dl_{1n} & dl_{2n} \end{bmatrix} \begin{bmatrix} \hat{L}_{l_1} \\ \hat{L}_{l_2} \end{bmatrix}$$

The proof is in Appendix A.

**Theorem 2.2:** The illumination directions for  $l_1, l_2, l_3$  direction are

$$L_{l_1} = \frac{\hat{L}_{l_1}}{k}, L_{l_2} = \frac{\hat{L}_{l_2}}{k}, L_{l_3} = \sqrt{1 - L_{l_1}^2 - L_{l_2}^2}.$$

where  $k = \sqrt{(\hat{di}^2) - (\hat{di})^2}$

$\hat{di}^2$  : the average value of  $di^2$  for the whole image.

$\hat{di}$  : the average value of  $di$  for the whole image.

and

$$\tau_L = \tan^{-1}\left(\frac{\hat{L}_{l_2}}{\hat{L}_{l_1}}\right), \quad \sigma_L = \cos^{-1} L_{l_3}$$

where  $\tau_L$  : Tilt angle of illumination direction

$\sigma_L$  : Slant angle of illumination direction

The proof is in Appendix B.

Pentland's method is a very good tilt estimator, as well as a very good slant estimator if the slant is below 40 degrees. However, due to the small variance of  $di(l_1, l_2)$ , this method results in a large error in the slant estimation whenever the slant is above 50 degrees. This experimental result has been confirmed by Lee [144] and Ferrie & Levine [73]

#### 2.2.1.2. Lee's Method

Lee suggested a different statistical approach to estimate the illumination direction [144]. By assuming that the slant  $\sigma$  is uniformly distributed over the sphere surface, the probability density function for the slant  $\sigma$  can be obtained by  $(\sin \sigma)/2\pi$ . To determine the expected value of image brightness  $i(l_1, l_2)$ , we should integrate only over the illuminated region, because not all of the sphere is illuminated. Thus, the region of integration should be set based on the foreshortening factor. Also, this region of integration can be different under the condition when the self-shadowed areas is included in the computation of the average. If we include the self-shadowed areas in the computation, we must divide the integral by the whole area,  $\pi$ , of the disc that is the projection of the hemisphere. If, on the other hand we do not include the self-shadowed areas, we divide by the area  $(\pi/2)(1+\cos\sigma_L)$  of the projection of the illuminated part of the hemisphere. Thus, from the integration, we can get the expected values of  $i(l_1, l_2)$  and  $i^2(l_1, l_2)$  as follows:

**Theorem 2.3:** *The slant of illumination direction  $\sigma_L$  satisfies*

$$E[i] = \frac{2\lambda\mu}{3\pi}(\sin\sigma_L + (\pi - \sigma_L)\cos\sigma_L)$$

$$E[i^2] = \frac{(\lambda\mu)^2}{8}(1 + \cos\sigma_L)^2 \quad , \text{when self-shadowed parts are included.}$$

$$E[i] = \frac{4\lambda\mu}{3\pi(1 + \cos\sigma_L)}(\sin\sigma_L + (\pi - \sigma_L)\cos\sigma_L)$$

$$E[i^2] = \frac{(\lambda\mu)^2}{4}(1 + \cos\sigma_L) \quad , \text{when self-shadowed parts are not included.}$$

where  $\lambda\mu$  is constant for the reflectance, and the mathematical expectation is taken over the whole image.

The proof is in Appendix C.

Thus, the slant  $\sigma_L$  can be estimated from above equations by taking the average value of intensities over the whole image for  $E[i]$  and  $E[i^2]$ . The tilt of illumination direction  $\tau_L$  can be also estimated from Theorem 4.1 of [144].

$$\tau_L = \tan^{-1} \left( \frac{\hat{E}[\frac{\partial}{\partial l_2} i(l_1, l_2)]}{\hat{E}[\frac{\partial}{\partial l_1} i(l_1, l_2)]} \right) \quad (2.2.1.2.1)$$

Here, the estimated values  $\hat{E}(\cdot)$  are taken over the whole image by taking the average value of the function.

Lee's method has several advantages over Pentland's method. First, calculation is much simpler, because calculations are required only once over the whole image. Second, we can calculate the slant of illumination direction directly from two equations without knowing the value of  $\lambda\mu$ . Experimental results of Lee's method are

known to be superior to Pentland's for the estimation of both tilt and slant. This has been confirmed by Lee [144] and Ferrie & Levine [73]. Because of these advantages, Lee's method was used to determine the illumination direction for the construction of 3-D shape in this thesis.

### **2.2.2. Estimation Of Surface Orientation**

The extraction of 3-D surface orientation from single 2-D images is an ill-posed problem, because we have only 2-D information but try to extract 3-D information from it. Therefore, we need additional information for this missing dimension to recover 3-D scene information. To date, several approaches have been suggested by researchers to give an additional constraint, such as the integrability, smoothness, etc. The following sections will discuss several approaches among them in detail.

#### **2.2.2.1. Horn And Brooks's Method**

Horn and Brooks [30, 100] developed a calculus of variation method to estimate surface orientation. In the presence of noise, the real values may not be the same as the estimated values that satisfy the image irradiance equation exactly. There will, however, be a surface that minimizes the integral of the square of the error between the expected values and the real values. Thus, the search for a function that minimizes an integral of this error was taken to be the major concern of this calculus of variations. However, this problem is an ill-posed problem, because there are typically an infinite number of surface satisfying this equation. Therefore, the equation needs an additional constraint to have a unique solution. Horn and Brooks proposed the additional constraint of a smoothness criterion [30]. Surface orientation can be

obtained by minimizing the following cost function

$$\begin{aligned} & \iint (i(l_1, l_2) - R(p, q))^2 + \lambda \cdot \left( \left( \frac{\partial^2}{\partial l_1^2} H(l_1, l_2) \right)^2 + 2 \left( \frac{\partial^2}{\partial l_1 \partial l_2} H(l_1, l_2) \right)^2 \right. \\ & \left. + \left( \frac{\partial^2}{\partial l_2^2} H(l_1, l_2) \right)^2 \right) dl_1 dl_2 \end{aligned} \quad (2.2.2.1.1)$$

Horn's method has good estimation results in the presence of noise. However, when the surface is not relatively smooth enough, the result from this method can possess the integrability problem. This lack of integrability can be found from the simulation examples in Section 2.2.3.

#### 2.2.2.2. Chellappa And Frankot's Method

Frankot and Chellappa's method [76, 78] is based on the calculus of variation method of Horn and Brooks. However, this method deals with one more constraint about the integrability. As discussed before, Horn & Brooks added the smoothness constraint to yield the unique solution, but that method can have the lack of integrability. Thus, Frankot and Chellappa proposed an additional constraint to enforce the integrability. This integrability can be achieved by satisfying the following requirement.

$$\frac{\partial^2}{\partial l_1 \partial l_2} H(l_1, l_2) = \frac{\partial^2}{\partial l_2 \partial l_1} H(l_1, l_2) \quad (2.2.2.2.1)$$

There are many conceivable ways of enforcing above equation. One of them is the minimization the following distance measure.

$$\iint ((p - E[p])^2 + (q - E[q])^2) dl_1 dl_2 \quad (2.2.2.2.2)$$

Let  $C$  be the coefficients of the Fourier series expansion of  $H(l_1, l_2)$ ,  $\hat{C}_{l_1}$  and  $\hat{C}_{l_2}$  be the

Fourier coefficients for the expectation values of  $p, q$  (slopes in directions of  $l_1, l_2$ ). Then, the above cost function can be minimized by taking

$$C(\omega) = \frac{-j\omega_{l_1} \hat{C}_{l_1}(\omega) - j\omega_{l_2} \hat{C}_{l_2}(\omega)}{\omega_{l_1}^2 + \omega_{l_2}^2} \quad (.3)$$

Thus, the construction of 3-D shape can be achieved by simply taking the inverse Fourier transform on  $C(\omega)$ .

Frankot and Chellappa's method is a good estimator of surface orientation. From the smoothness constraint and enforcing integrability, the general shape of the 3-D object can be obtained. However, due to too much smoothing, the detail information about the surface may be lost.

### 2.2.2.3. Pentland's Method

The Shape-from-shading problem is known to be mathematically equivalent to a nonlinear first-order partial differential equation in surface elevation. Therefore, it is very difficult to obtain the closed form solution. For this reason, Pentland [169] proposed a linear approximation method to estimate the values, using a Taylor series expansion in  $p, q$  variables up to the second order. Thus,

$$i(l_1, l_2) \cong \cos\sigma_L + p\cos\tau_L \sin\sigma_L + q\sin\tau_L \sin\sigma_L - \frac{\cos\sigma_L}{2}(p^2 + q^2) \quad (2.2.2.3.1)$$

The corresponding DFT of  $i(l_1, l_2)$  is as follows. (after deleting the constant term  $\cos\sigma_L$ )

$$f_i(k_1, k_2) \cong \cos\tau_L \sin\sigma_L f_p(k_1, k_2) + \sin\tau_L \sin\sigma_L f_q(k_1, k_2) - \frac{\cos\sigma_L}{2}(f_p \otimes f_p + f_q \otimes f_q)$$

$$(2.2.2.3.2)$$

Then,  $\hat{f}_p(k_1, k_2)$  and  $\hat{f}_q(k_1, k_2)$  can be represented as the function of  $\hat{f}_H(k_1, k_2)$ , by the approximation of the first derivative of  $H(l_1, l_2)$  function. Thus,  $\hat{f}_i(k_1, k_2)$  can be represented as a function of  $\hat{f}_H(k_1, k_2)$  only, and the height function  $H(l_1, l_2)$  can be constructed by simply taking the inverse Fourier transform of the intensity function  $i(l_1, l_2)$ .

$$\hat{f}_p(k_1, k_2) = j \sin(2\pi \frac{k_1}{N}) \hat{f}_H(k_1, k_2) \quad (2.2.2.3.3)$$

Similarly,

$$\hat{f}_q(k_1, k_2) = j \sin(2\pi \frac{k_2}{N}) \hat{f}_H(k_1, k_2) \quad (2.2.2.3.4)$$

Under the condition  $|p|, |q| < 1$ , the linear term dominates. Thus,

$$\begin{aligned} \hat{f}_i(k_1, k_2) &\equiv \cos\tau_L \sin\sigma_L \hat{f}_p(k_1, k_2) + \sin\tau_L \sin\sigma_L \hat{f}_q(k_1, k_2) \\ &\equiv j \sin\sigma_L (\sin(2\pi \frac{k_1}{N}) \cos\tau_L + \sin(2\pi \frac{k_2}{N}) \sin\tau_L) \hat{f}_H(k_1, k_2) \end{aligned} \quad (2.2.2.3.5)$$

Pentland's method has a nice mathematical formulation because in frequency domain, the equation has only one unknown variable. Thus, this equation has a unique solution. However, the first-order linear approximation yields a big estimation error, while the second-order approximation requires convolution in frequency domain and requires too much computation. This results will be confirmed from the examples in Section 2.2.3.

### 2.2.3. Simulation Results

A  $128 \times 128$  real image of a part of a tree in a grass meadow is considered (Figure 2.3). From this image, the estimation values of the illumination direction  $\sigma_L$ ,  $\tau_L$  was determined to be  $\hat{\sigma}_L = -1.3384$ ,  $\hat{\tau}_L = -4.257899e-02$ , by applying Lee's method. Following Figure 2.4-a,b show the results of the height functions constructed from Horn and Brooks's and Frankot and Chellappa's algorithms, respectively. From these, we can see that Frankot's algorithm gives a nice and smooth height function, while Horn's gives a rough surface but detailed information of the surface. The experiments were repeated for the smoothed part images which were obtained by different sizes of smoothing windows. These experiments could give the idea of how the smoothing affects the results. Figure 2.5-a,b,c depict the part images which are smoothed by the different sizes of window, and Figure 2.6-a,b, Figure 2.7-a,b, and Figure 2.8-a,b also depict the corresponding height functions from each cases by Horn's and Frankot's, respectively. From these experiments, we can see that for the image smoothed by the relatively large size of window, Horn's and Frankot's are getting closer. Pentland's algorithm was not considered here, because of the poor performance from the linear approximation. Figure 2.9 shows the resulting height function constructed from the low-frequency linear approximation method of Pentland for Figure 2.5-b.



Figure 2.3 : A digitalized tree image sized by  $512 \times 512$

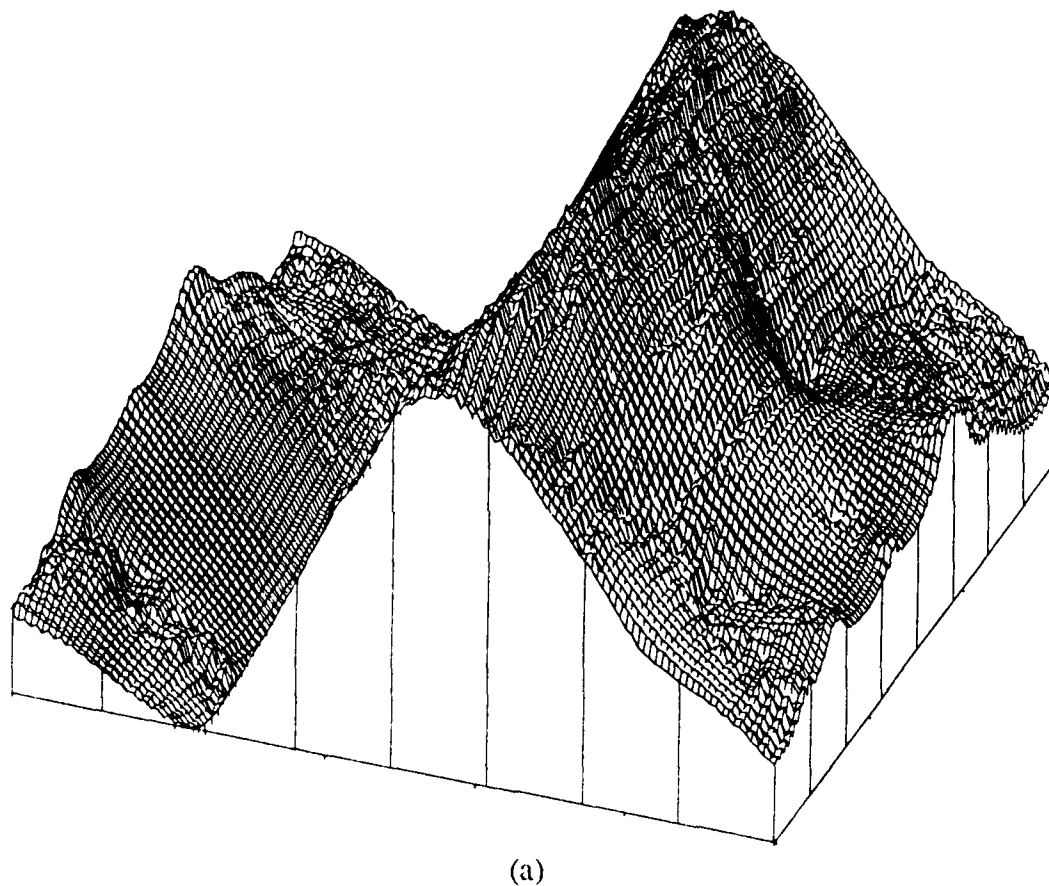
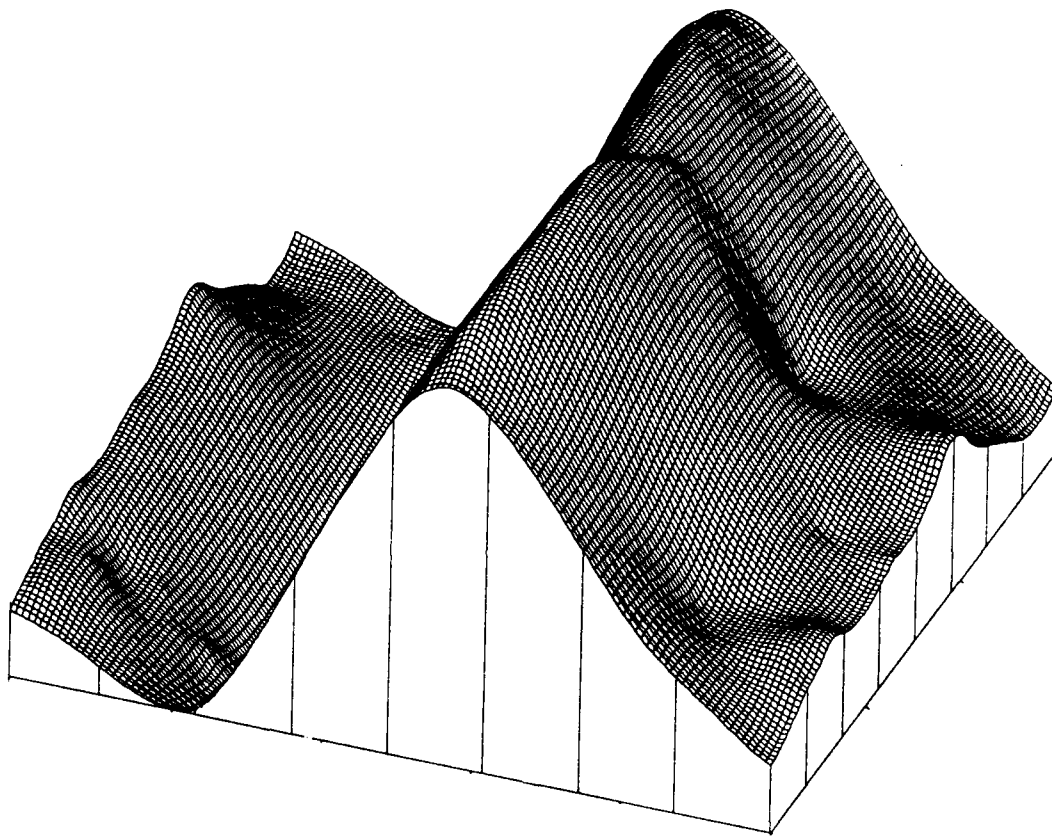


Figure 2.4: The height function of Figure 2.3: constructed by (a) Horn's method, (b) Frankot's method: Surface orientation for each pixel was obtained from minimizing the cost function (2.2.2.1.1) and (2.2.2.2.2), respectively.



(b)

Figure 2.4, continued



(a)



(b)



(c)

Figure 2.5: A part of the tree image (Figure 2.3): (a) original, (b) Image obtained after convoluting a  $5 \times 5$  smoothing window to (a), (c) Image obtained after convoluting a  $9 \times 9$  smoothing window to (a).

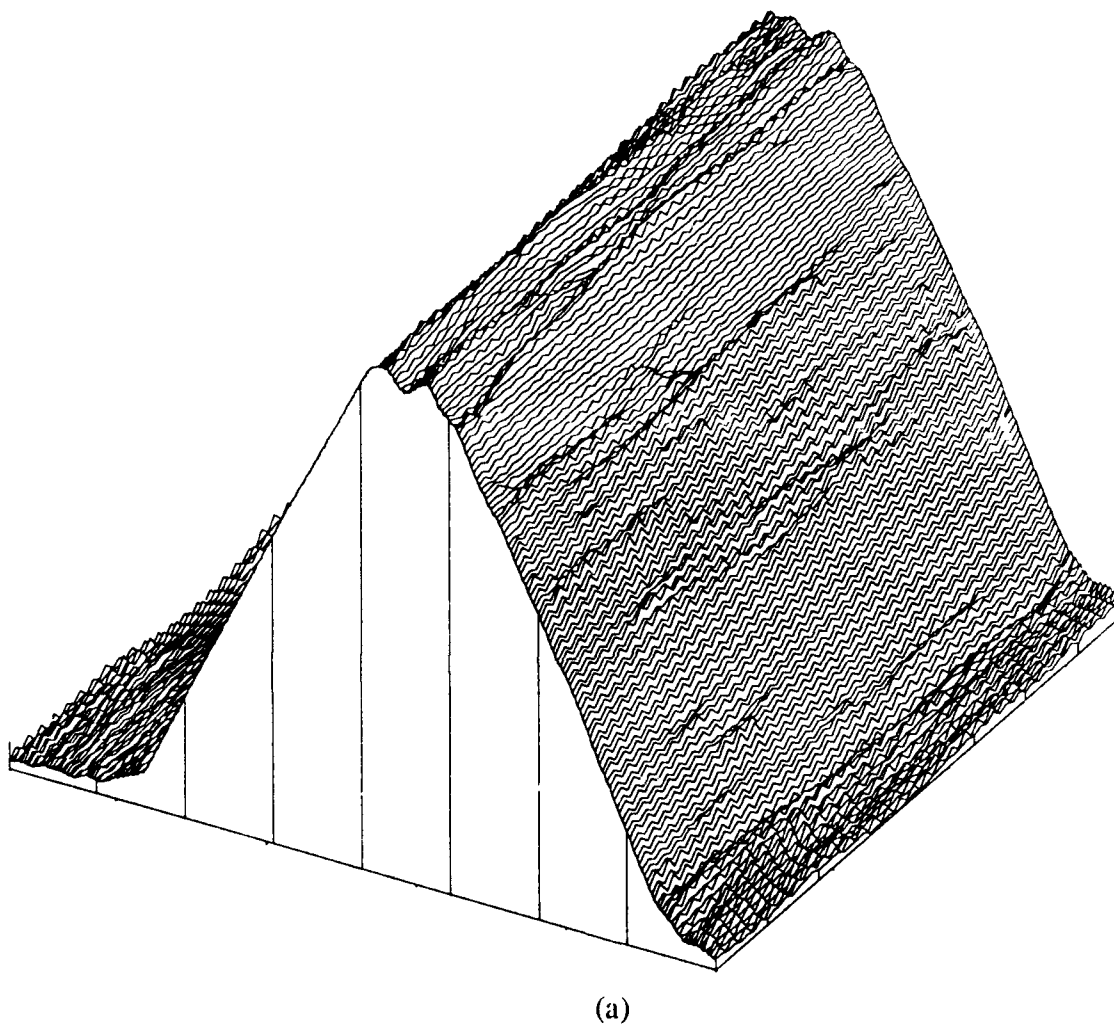
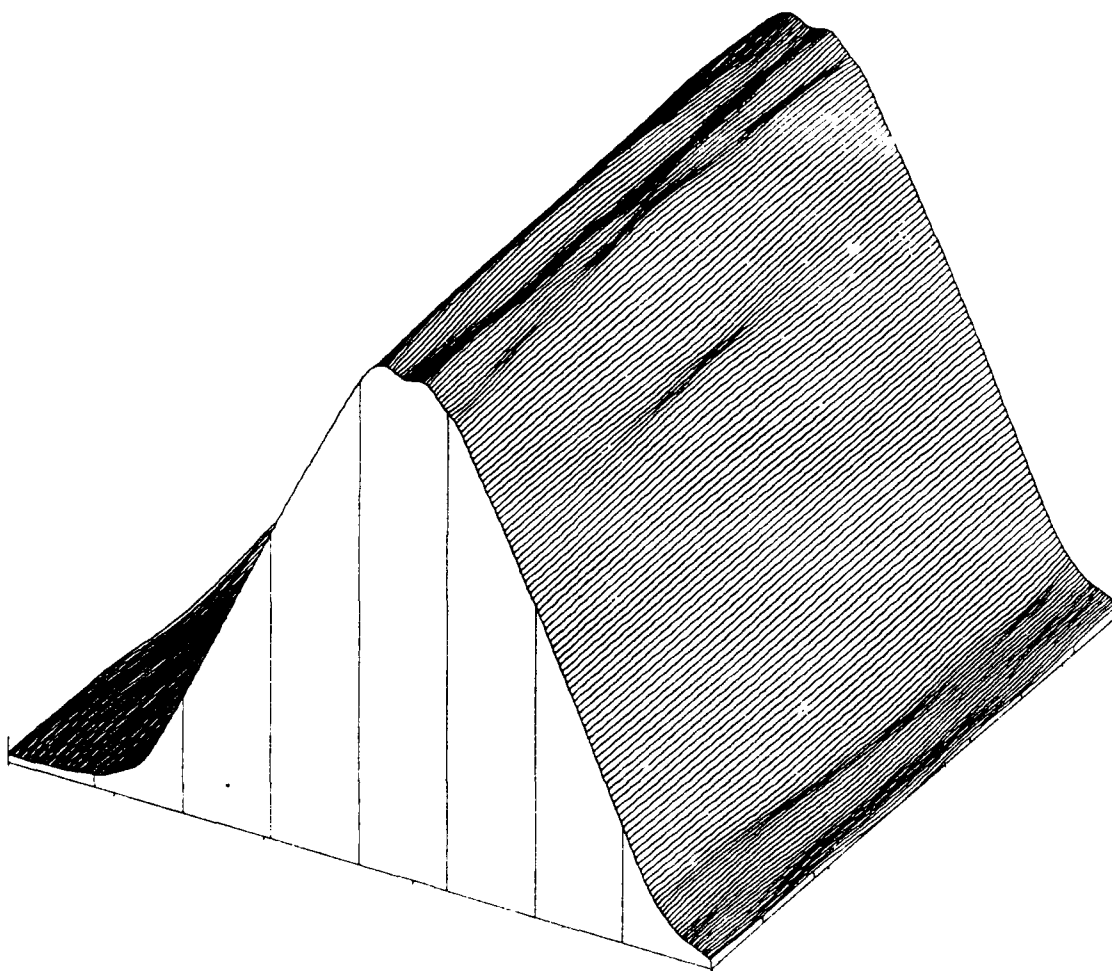


Figure 2.6: The height function of Figure 2.5-a: constructed by (a) Horn's method, (b) Frankot's method: Surface orientation for each pixel was obtained from minimizing the cost function (2.2.2.1.1) and (2.2.2.2.2), respectively.



(b)

Figure 2.6, continued

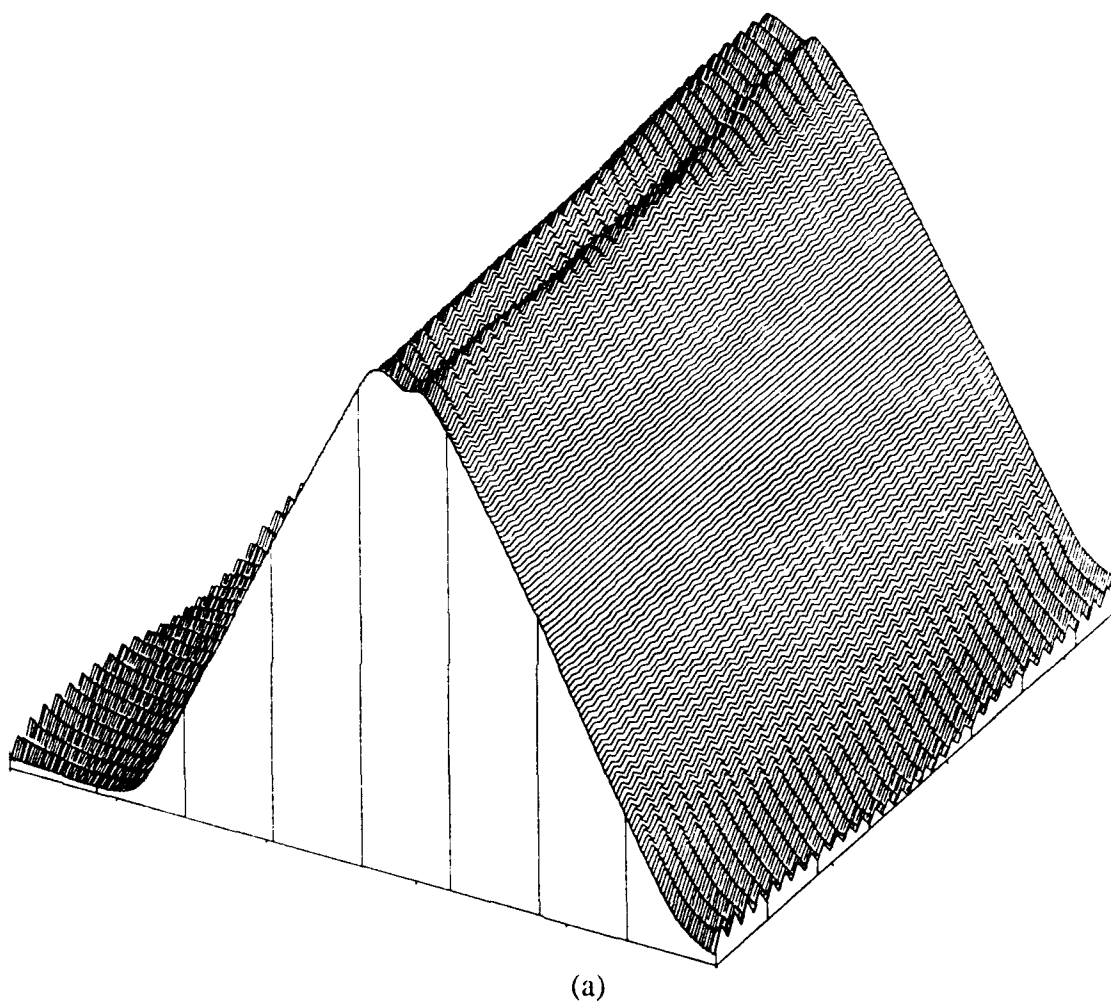
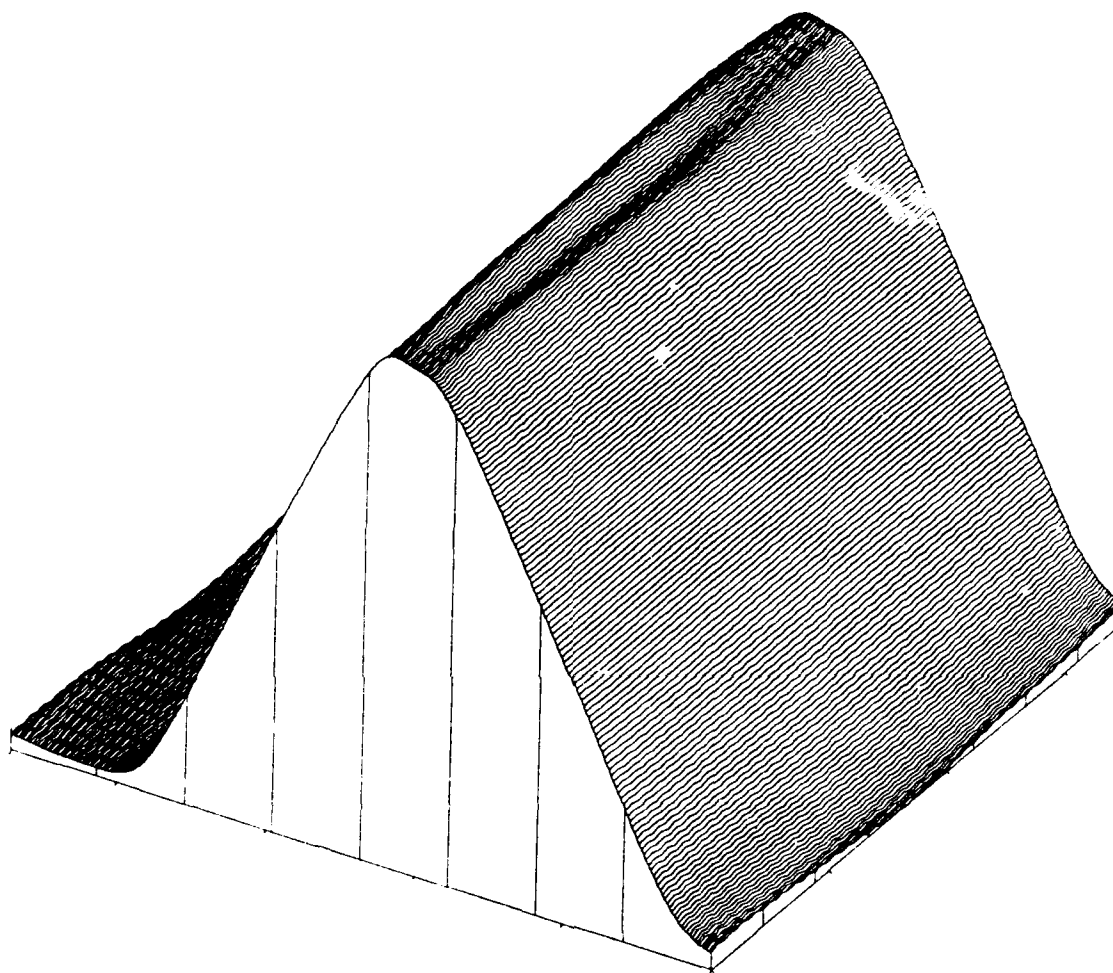


Figure 2.7: The height function of Figure 2.5-b: constructed by (a) Horn's method, (b) Frankot's method: Surface orientation for each pixel was obtained from minimizing the cost function (2.2.2.1.1) and (2.2.2.2.2), respectively.



(b)

Figure 2.7, continued

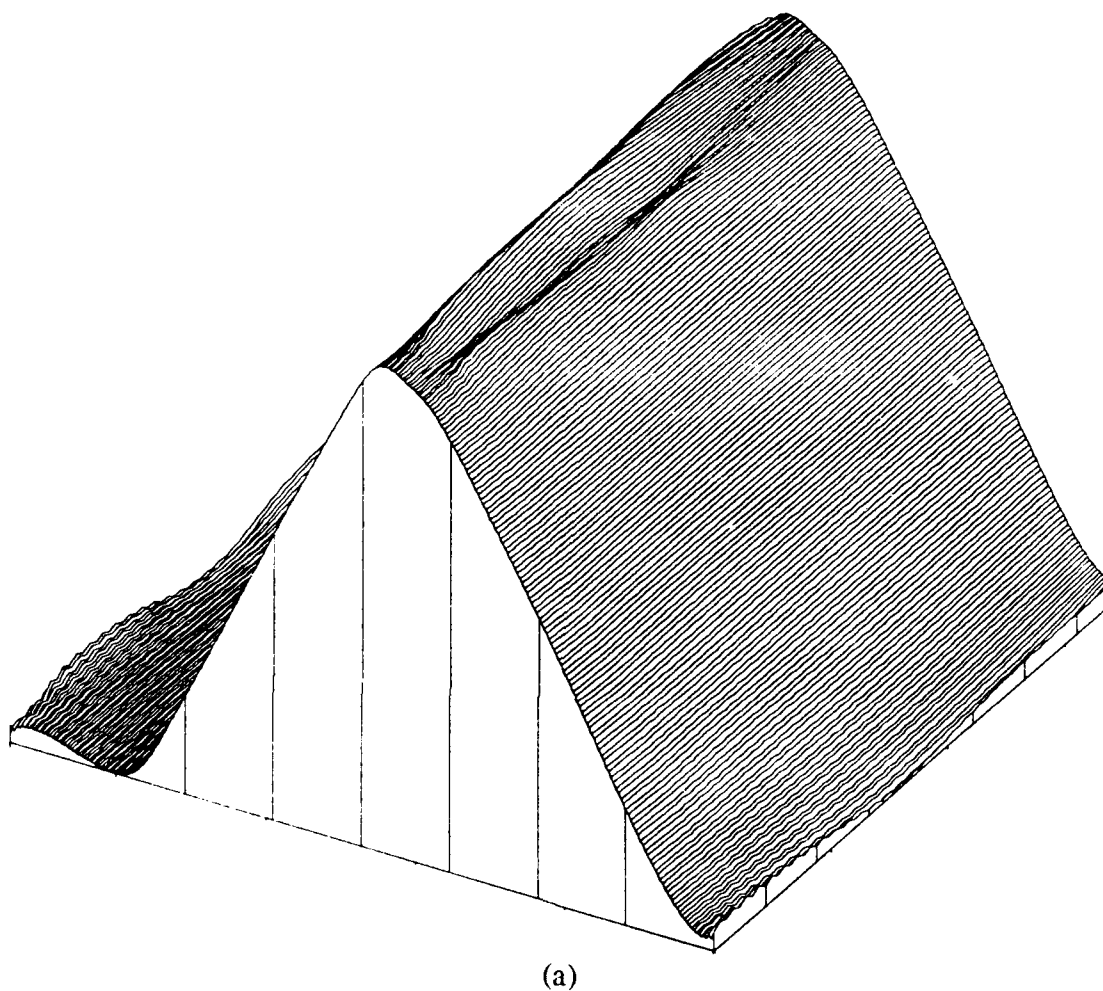


Figure 2.8: The height function of Figure 2.5-c: constructed by (a) Horn's method, (b) Frankot's method: Surface orientation for each pixel was obtained from minimizing the cost function (2.2.2.1.1) and (2.2.2.2.2), respectively.

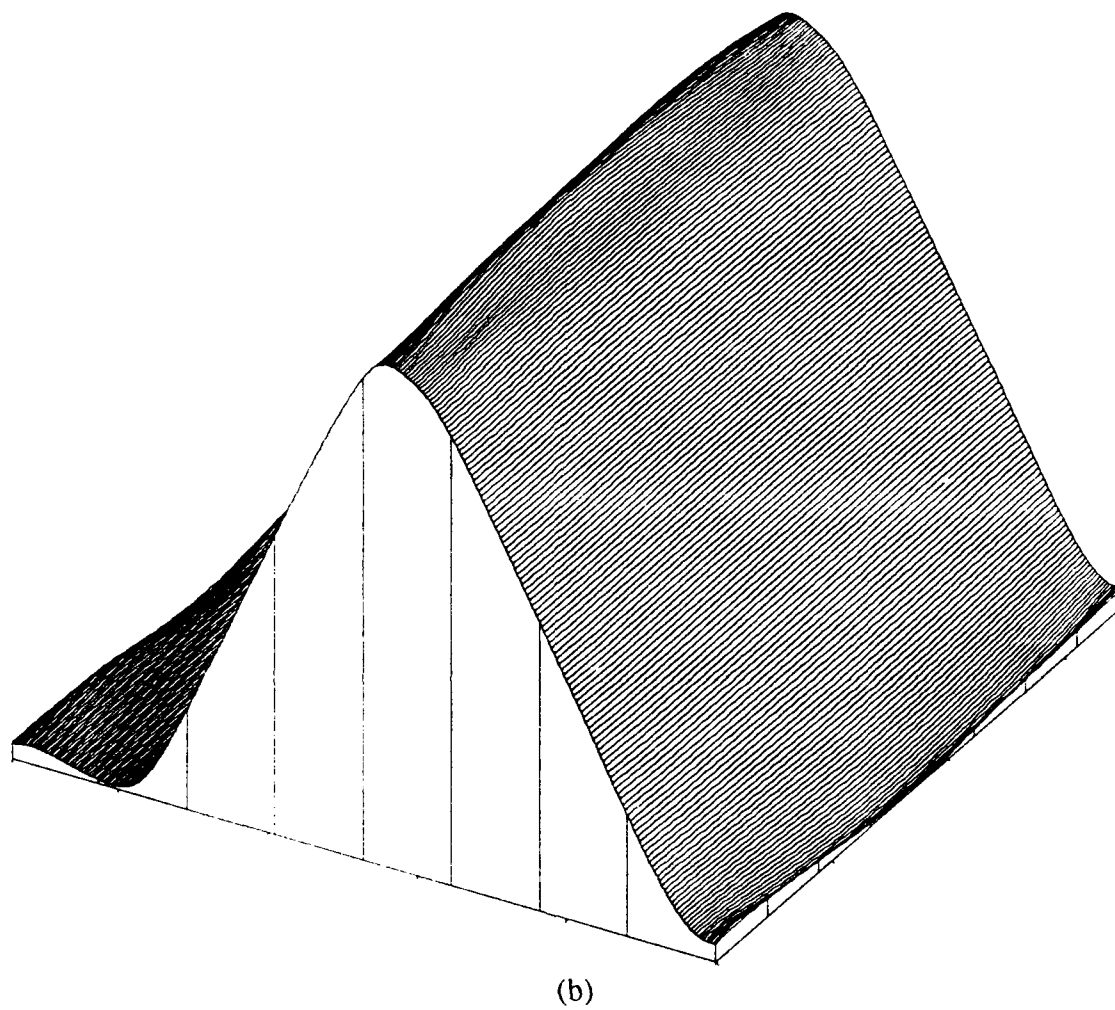


Figure 2.8, continued.

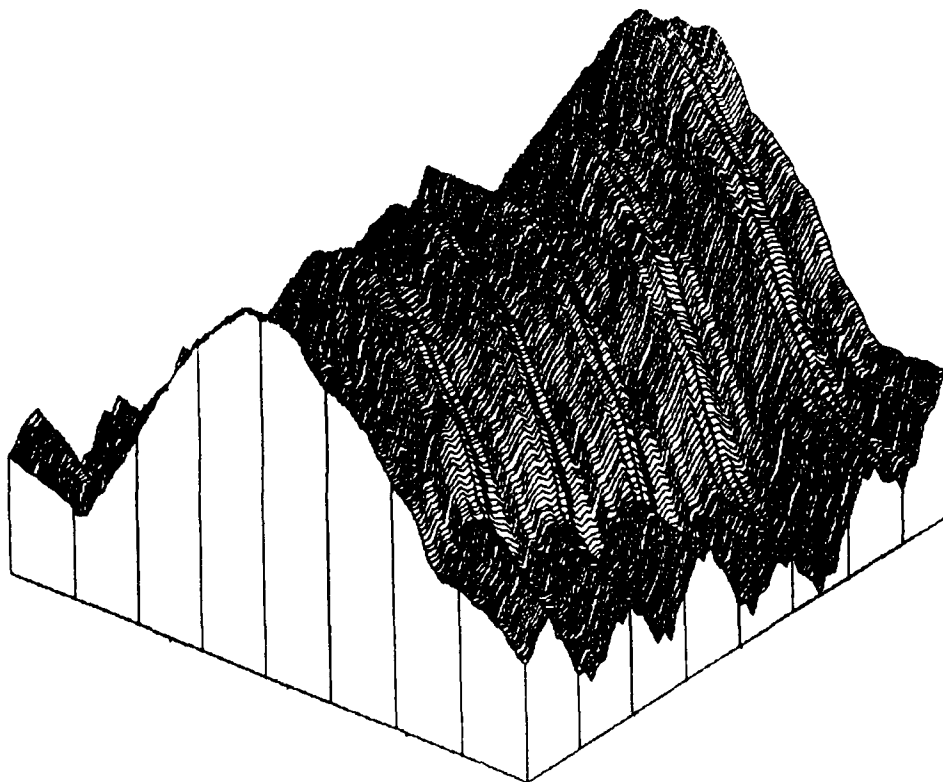


Figure 2.9: The height function of Figure 2.5-b, which was constructed by Pentland's method(2.2.2.3.1-5): Closed form solution of the surface orientation was obtained in the frequency domain by the linear approximation method.

### 2.3. Shape-From-Texture

The Shape-from-texture problem has been studied extensively to recover the 3-D information from a two dimensional image [6, 109, 135, 136, 156, 221] since Gibson first proposed the texture density gradient as the primary basis of surface perception by humans in 1950. Motivated to simulate human perception, he confines the surfaces under consideration to only those whose orientations could be easily perceived from the texture by human eye. However, if the true texture is not isotropic and has a preferred orientation, it mimics a projected image and thus makes it difficult to detect the true orientation. Therefore, to formalize the shape-from-texture problem requires a projection model for the image formation system. Up to now, two kinds of projections called 'orthographical projection' and 'perspective projection' have been used in most of cases. The orthographical projection can be obtained by projecting the object surface to the image plane parallelly without considering the average distance from the camera, while in the perspective projection model, the scene depth is relative to the distance between the object and the camera. Thus, the perspective transformation yields orthographical projection as a special case when the viewpoint is at a point infinitely far from the object surface. Another model required to formalize the shape-from-texture is a random field model. This model should represent the statistical property of the texture on the surface properly, and its parameter estimation scheme should exist. Various types of random field models have been proposed to date to represent the surface covered by texture. Among them, the AR(Auto-Regressive) model [41, 122] is known to be simple enough to estimate and synthesize the texture plane whose statistical pattern is isotropically distributed over the plane. Another noticeable model for the 3-D textured surface is the Fractal model [133, 173]. The fractal model contains a fractal scaling parameter. This fractal scaling parameter can

be a measure of the roughness of the surface and can be considered as a scale and rotational invariant parameter. However, these models have their own limitations in representing the true texture surface. The AR model does not have a long-term persistent memory property, thus, it is not proper for the texture pattern which contains a long-term memory in a certain direction, such as a tree-bark image. On the other hand, the Fractal model has only three variable parameters, mean, variance and fractal scaling. Those are not flexible enough to model the wide range of situations encountered in practice. This conflict can be solved in the fractional differencing periodic model which is suggested in this paper. That is, the fractional differencing periodic model contains four parameters, two frequency parameters, which are similar to the texture pattern parameters in AR model, and two other fractional differencing parameters, which are corresponding to the fractal scaling parameter in the fractal model. Therefore, the fractional differencing periodic model gives more flexibility of modeling.

### **2.3.1. Projection**

As mentioned in previous section, the projection model is basic and necessary to formalize the shape-from-texture problem to represent the slanted and tilted texture surface. To date, there are two different projection models which have been used in most cases. Those are 'Orthographical projection' and 'Perspective projection'. Detail discussion on these will be given in the following sections.

### 2.3.1.1. Orthographical Projection

Consider a plane with a texture on it, and take the  $m_1$ - $m_2$  coordinate system. Put a line passing through the origin, and let  $\tau$  be the angle made from the  $m_1$ -axis. Rotate the plane around the line by angle  $\sigma$  and project the rotated plane orthographically onto the original plane (Figure 2.10).

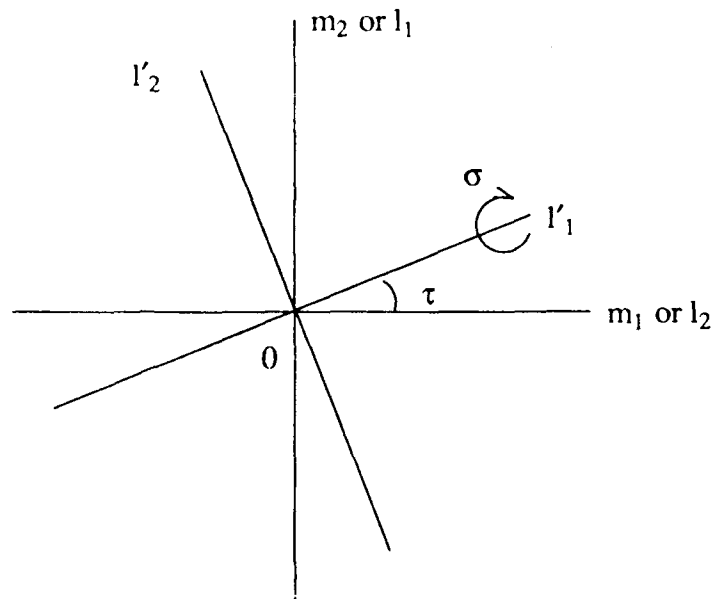


Figure 2.10: Coordinate transformation of the orthographic projection (2.3.1.1.4)

Thus, a new coordinate system from the viewing direction,  $l_1$ - $l_2$ , can be obtained from the following two coordinate transformations.

$$\begin{bmatrix} l'_1 \\ l'_2 \end{bmatrix} = \begin{bmatrix} \cos\tau & -\sin\tau \\ \sin\tau & \cos\tau \end{bmatrix} \begin{bmatrix} m_1 \\ m_2 \end{bmatrix}, \quad (2.3.1.1.1)$$

and

$$\begin{bmatrix} l_1 \\ l_2 \end{bmatrix} = \begin{bmatrix} 1 & 0 \\ 0 & \cos\sigma \end{bmatrix} \begin{bmatrix} l'_1 \\ l'_2 \end{bmatrix} \quad (2.3.1.1.2)$$

Hence, as is well known, the coordinate transformation of the orthographic projection between the  $m_1$ - $m_2$  system and  $l_1$ - $l_2$  system can be given as follows.

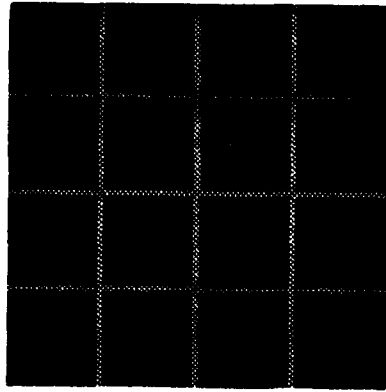
$$\begin{bmatrix} l_1 \\ l_2 \end{bmatrix} = \begin{bmatrix} \cos\tau & -\sin\tau \\ \sin\tau & \cos\tau \end{bmatrix} \begin{bmatrix} 1 & 0 \\ 0 & \cos\sigma \end{bmatrix} \begin{bmatrix} \cos\tau & -\sin\tau \\ \sin\tau & \cos\tau \end{bmatrix}^{-1} \begin{bmatrix} m_1 \\ m_2 \end{bmatrix} \quad (2.3.1.1.3-a)$$

$$= \begin{bmatrix} \cos^2\tau + \cos\sigma \sin^2\tau & (1 - \cos\sigma) \sin\tau \cos\tau \\ (1 - \cos\sigma) \sin\tau \cos\tau & \sin^2\tau + \cos\sigma \cos^2\tau \end{bmatrix} \begin{bmatrix} m_1 \\ m_2 \end{bmatrix} \quad (2.3.1.1.3-b)$$

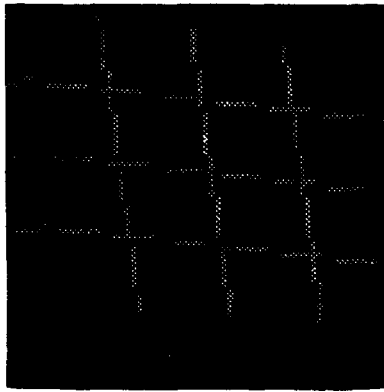
Thus,

$$\begin{bmatrix} m_1 \\ m_2 \end{bmatrix} = \frac{1}{\cos\sigma} \begin{bmatrix} \sin^2\tau + \cos\sigma \cos^2\tau & (\cos\sigma - 1) \sin\tau \cos\tau \\ (\cos\sigma - 1) \sin\tau \cos\tau & \cos^2\tau + \cos\sigma \sin^2\tau \end{bmatrix} \begin{bmatrix} l_1 \\ l_2 \end{bmatrix} \quad (2.3.1.1.4)$$

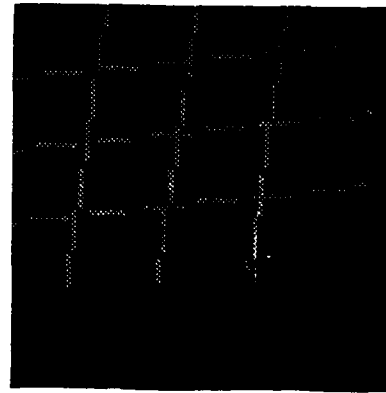
One grid pattern image (Figure 2.11-a) was considered to demonstrate this orthogonal projection. The coordinate transformation was taken to this image with  $\sigma = \frac{\pi}{8}$ ,  $\tau = \frac{\pi}{4}$  and  $\sigma = \frac{\pi}{8}$ ,  $\tau = -\frac{\pi}{4}$ . Figure 2.11-b and Figure 2.11-c depict these transformation respectively.



(a)



(b)



(c)

Figure 2.11: 2-D grid pattern images: (a) Original, (b) Image obtained after projecting the image (Figure 2.11-a) orthographically, with  $\sigma = \pi/4$  and  $\tau = \pi/8$  in (2.3.1.1.4), (c) Image obtained after projecting the image (Figure 2.11-a) orthographically, with  $\sigma = \pi/4$  and  $\tau = -\pi/8$  in (2.3.1.1.4).

### 2.3.1.2. Perspective Projection

The perspective projection acts like a pinhole camera in that the image results from projecting scene points through a single point onto an image plane.

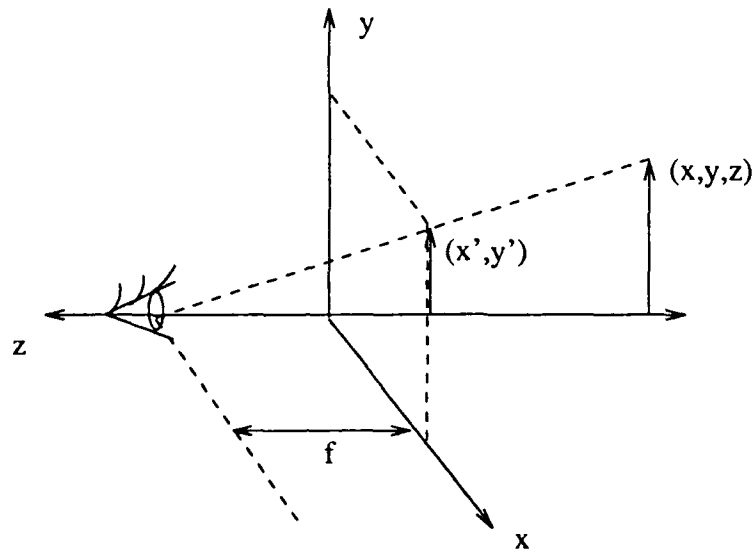


Figure 2.12 : Perspective projection

As in Figure 2.12, if the point of projection corresponds to a viewpoint behind the image plane and the image occurs right side up, the viewpoint is  $+f$  on the  $z$  axis, with  $z = 0$  plane being the image plane upon which the image is projected. Thus, as the image object approaches the viewpoint, its projection gets bigger. In Figure 2.12,  $y'$ , the projected height of the object, is related to its real height  $y$ , its position  $z$ , and the focal length  $f$  by

$$y' = (f/f-z)y \quad (2.3.1.2.1)$$

Similarly

$$x' = (f/f-z)x \quad (2.3.1.2.2)$$

The projected image has  $z=0$  everywhere. However, projecting away the  $z$  component is best considered a separate transformation; the projective transform is usually thought to distort the  $z$  component just as it does the  $x$  and  $y$ . Perspective distortion thus maps  $(x, y, z)$  to

$$(x', y', z') = \left( \frac{fx}{f-z}, \frac{fy}{f-z}, \frac{fz}{f-z} \right) \quad (2.3.1.2.3)$$

Notice that the perspective transformation yields orthographical projection as a special case when the viewpoint is the point at infinity in the  $z$  direction. Then all objects are projected onto the viewing plane with no distortion of their  $x$  and  $y$  coordinates. Another point about the perspective transformation is that if  $z$  is a known function of  $x, y$  and the surface orientation  $\sigma$  and  $\tau$ , the result of the transformations in (2.3.1.2.1) and (2.3.1.2.2) is a nonhomogeneous planar texture. This is important because under orthographical projection a homogeneous texture on a slanted and tilted plane was transformed to another homogeneous texture due to the linearity of the transformation (2.3.1.1.4), while under perspective projection it is not a homogeneous texture any more. Thus, the analysis in the frequency domain by the discrete Fourier transform is no longer valid.

To overcome this difficulty associated with the perspective projection, we can approximate the perspective projection by an affine transformation which is suggested by Aloimonos and Swain [6]. The approximation is done by dividing the projection process into two steps. The first step is projecting the local plane  $Q$  with orientation given by  $\sigma, \tau$  onto the plane  $T$  which is parallel to image plane  $I$ . This projection is performed parallel to the ray  $OG$ , where  $G$  is the center of local plane. The second step is projecting this plane  $T$  perspectively onto the image plane  $I$ . Since the plane  $T$

is parallel to the image plane, this perspective transformation is just a reduction by a factor of  $1/\beta$ . Figure 2.13 depicts this relationship.

Thus, the transformation from surface plane coordinate  $(m_1, m_2)$  to image plane coordinate  $(l_1, l_2)$  with the two step projection process is given by the following affine transformation [6].

$$\begin{bmatrix} l_1 \\ l_2 \end{bmatrix} = \frac{1}{\beta} \begin{bmatrix} \frac{-1+pA}{\sqrt{1+p^2}} & \frac{q(p+A)}{\sqrt{(1+p^2)(1+p^2+q^2)}} \\ \frac{pB}{\sqrt{1+p^2}} & \frac{qB-p^2-1}{\sqrt{(1+p^2)(1+p^2+q^2)}} \end{bmatrix} \begin{bmatrix} m_1 \\ m_2 \end{bmatrix} \quad (2.3.1.2.4)$$

Here, the point  $(A, B, -1)$  is the mass center of the image texel, and  $p, q$  are the same as defined in (2.2.1). Therefore, the non-homogeneous texture due to perspective projection can be approximated by piecewise homogeneous ones, and each local homogeneous texture patch is easily synthesized by using the above linear affine transformation.

### 2.3.2. Random Texture Analysis

For the surface which is covered by a texture pattern, or is relatively complex, the random field model can be applied over the surface normal plane for approximating the surface image. However, differently from the regular 2-D texture analysis, 3-D textural surface image analysis can be enhanced by considering the fractional differencing parameter, (which is the 'fractal scaling parameter' in the terminology of Pentland [173, 176]) which indicates the roughness of the surface, in addition to the texture pattern. In other words, a 3-D textured surface can be represented by the fractal scaling and the texture pattern parameters in a certain random field model. Therefore, the model based on 2-D texture pattern only, such as

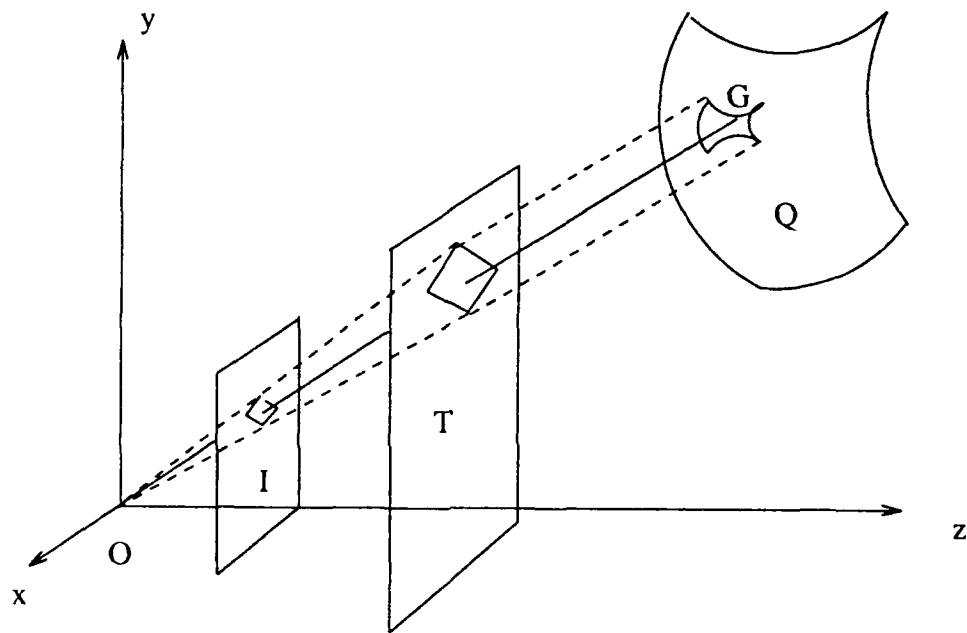


Figure 2.13 : Approximation method of perspective projection

the Auto-Regressive(AR) model [122], or the model based on 2-D fractional Brownian motion process with one fractal scaling parameter, such as Pentland's model [176], has limited modeling ability. That is because the AR model or the fractal model can represent only the texture pattern or the roughness of the surface, thus, either model is not flexible enough to represent the wide range of different texture patterns encountered in practice, especially non-stationary random texture. This limitation can be overcome by using the 2-D FDP (Fractional Differencing Periodic) model which contains both texture pattern and fractal scaling parameters [67].

### 2.3.2.1. Auto-Regressive(AR) Model

The autoregressive model is one of the classical short correlation models. This model is simple but has good modeling performance. Assume that the image intensity follows the autoregressive model. Let  $(l_1, l_2)$  be an index for the coordinate location and  $i(l_1, l_2)$  be the intensity at the coordinate  $(l_1, l_2)$ . Then the auto-regressive model is represented by the following equation.

$$i(l_1, l_2) = \theta^T z(l_1, l_2) + \zeta(l_1, l_2) \quad (2.3.2.1.1)$$

where  $\theta$  is parameter vector and  $z(l_1, l_2)$  is a vector which consists of intensities of the neighbor pixels and unity.  $\{ \zeta(l_1, l_2) \}$  is a two dimensional white noise sequence with variance  $\rho$ .

For example, in case of the Causal Auto-Regressive (CAR) model as a special case of the AR model, the parameter vector  $\theta$  is  $4 \times 1$  column vector and  $z(l_1, l_2)$  is another  $4 \times 1$  column vector which contains three causal neighbors and unity as the elements.

$$z(l_1, l_2) = \begin{bmatrix} i(l_1, l_2-1) \\ i(l_1-1, l_2) \\ i(l_1-1, l_2-1) \\ 1 \end{bmatrix} \quad (2.3.2.1.2)$$

Notice that because of the causality of this model, the resulting two dimensional model has all the convenience of a one dimensional model.

The parameters  $\theta$  and  $\rho$  can be estimated by the least squares method. Let  $\hat{\theta}$  and  $\hat{\rho}$  be the least squares estimators of  $\theta$  and  $\rho$ . Then

$$\hat{\theta} = \left[ \sum_{l_1, l_2} z(l_1, l_2) z(l_1, l_2)^T \right]^{-1} \left[ \sum_{l_1, l_2} z(l_1, l_2) i(l_1, l_2) \right] \quad (2.3.2.1.3)$$

and

$$\hat{\rho} = \frac{1}{N^2} \sum_{l_1, l_2} [i(l_1, l_2) - \hat{\theta}^T z(l_1, l_2)]^2 \quad (2.3.2.1.4)$$

where  $N$  is row and column dimensions of the image.

Therefore, because of the simplicities of estimation and synthesis, the AR model has been used in various applications. However, for the case of 3-D texture surface representation, this model is not enough to handle long-correlated texture pattern in some directions such as a tree bark image, because of its short-correlated property.

### 2.3.2.2. Fractal Model

In 3-D textural surface image, the fractional differencing parameter, which is 'fractal scaling parameter' in the terminology of Pentland [173, 176], indicates the roughness of the surface. That is, as the value of the fractal scaling parameter increases, the model represents a 3-D surface textured more roughly. Typical 2-D fractional Brownian motion surface  $i(l_1, l_2)$ , which was suggested by Pentland,

satisfies the following relationship. Define  $\Delta i_{\Delta r} = |i(l_{12}, l_{22}) - i(l_{11}, l_{21})|$ ,  $\Delta r = \sqrt{(l_{12} - l_{11})^2 + (l_{22} - l_{21})^2}$ . Then

$$E(\Delta i_{\Delta r}) \propto \Delta r^F \quad (2.3.2.2.1)$$

The fractal dimension of the fractional Brownian motion surface is then  $3 - F$  [151, 46]. However, this model is not proper to present 3-D texture pattern because the fractal of surface is assumed to be spatially isotropic, thus, the fractional Brownian motion process with one fractal parameter is not flexible enough to represent the wide range of different texture patterns encountered in practice, especially non-stationary random texture. Also, comparing with other model-based model such as AR model, this model is not practical to be used because it is difficult to estimate the fractal scaling parameter from the given intensity image directly.

### 2.3.2.3. Fractional Differencing Model

The 1-D Fractional Differencing model was suggested by Hosking [101], generalizing the well-known ARIMA model of Box & Jenkins [23], which was originally designed to model a non-stationary random process. This 1-D model was extended to 2-D case by Kashyap and Lapsa [116] later. A typical second-order Fractional Differencing Periodic (FDP) model is as follows.

$$i(l_1, l_2) = (1 - 2\cos\omega_1 z_1^{-1} + z_1^{-2})^{-\frac{c}{2}} \cdot (1 - 2\cos\omega_2 z_2^{-1} + z_2^{-2})^{-\frac{d}{2}} \zeta(l_1, l_2) \quad (2.3.2.3.1)$$

for  $l_1, l_2 = 0, 1, \dots, N-1$ .

The corresponding DFT of this function is

$$I(k_1, k_2) = (1 - 2\cos\omega_1 e^{-j2\pi\frac{k_1}{N}} + e^{-j4\pi\frac{k_1}{N}})^{-\frac{c}{2}} \cdot (1 - 2\cos\omega_2 e^{-j2\pi\frac{k_2}{N}} + e^{-j4\pi\frac{k_2}{N}})^{-\frac{d}{2}} W(k_1, k_2), \quad (2.3.2.3.2)$$

where  $z_i$  is the delay operator associated with  $l_i$ ,  $\zeta(l_1, l_2)$  is an i.i.d. Gaussian sequence, and  $W(k_1, k_2)$  is the corresponding DFT.

This model has four different parameters,  $c$  and  $d$  for the fractal scales and  $\omega_1$  and  $\omega_2$  for the frequencies of pattern in the direction of  $l_1$  and  $l_2$ , respectively. Thus, this model represents the roughness of the surface and the pattern of the texture image at the same time even with the different values for the direction of  $l_1$ ,  $l_2$  separately. Also notice that this random process model has the property of being flexible enough to explain both the long-term and short-term correlation structure of a time series depending on the values of the fractional differencing parameter  $c$ ,  $d$ , and it shares the basic properties with Fractional Brownian motion defined by Mandelbrot [151]. More detailed discussion about estimation scheme and synthesis of this model will be given in the next section.

### 2.3.3. Simulation Results

For the experiment, one tree bark texture on the surface of a tree is considered (Figure 2.14-a). As seen from Figure 2.14-a, the pattern of tree bark texture has different values of frequency and roughness in the horizontal and vertical directions. Thus, it cannot be represented by either Pentland's model or a 2nd-order AR model, because Pentland's model can have only various fractal scales and a 2nd-order AR

model has only directional frequencies. Figure 2.14-b,c show the limitation of Pentland's Fractal models with fractal scale  $c=0.9$  and  $c=1.5$ , respectively, and Figure 2.14-d shows the limitation of a 2nd-order AR model with the directional frequencies  $\omega_1=0.25$  and  $\omega_2=0.025$  in direction of  $m_1, m_2$ .

On the other hand, Figure 2.15 shows how well the Fractional Differencing Periodic (FDP) model fits to the tree bark texture. Here, the directional frequencies  $\omega_1, \omega_2$  and the fractal scales  $c, d$  in FDP model are chosen as 0.25, 0.025, 1.5, 0.8, respectively.

## 2.4. Conclusions

Various models to represent 3-D surface have been considered. The Shape-from-shading model is based on the reflectance map function which shows scene radiance as a function of the surface gradient and the distribution of light sources to extract 3-D surface information. The Shape-from-texture model uses the texture pattern instead of shading to extract 3-D structure. Then, the fractal model was discussed considering a fractal scale to represent the roughness of the surface. Thus, several estimation schemes for the direction of the light, the projection methods, and 2-D statistical texture models have been considered. However, for describing a natural scene image, the above approaches have their own limitations. The Shape-from-shading model is applicable only under the assumption that the surface is smooth enough to have clear radiance information, the Shape-from-texture model requires the surface to be relatively complex so that texture information can be extracted, and the fractal model with one fractal scaling parameter does not have enough flexibility to represent the various texture patterns which we can encounter in practice. To give more flexibility to represent a real surface image and to have an ability to handle the

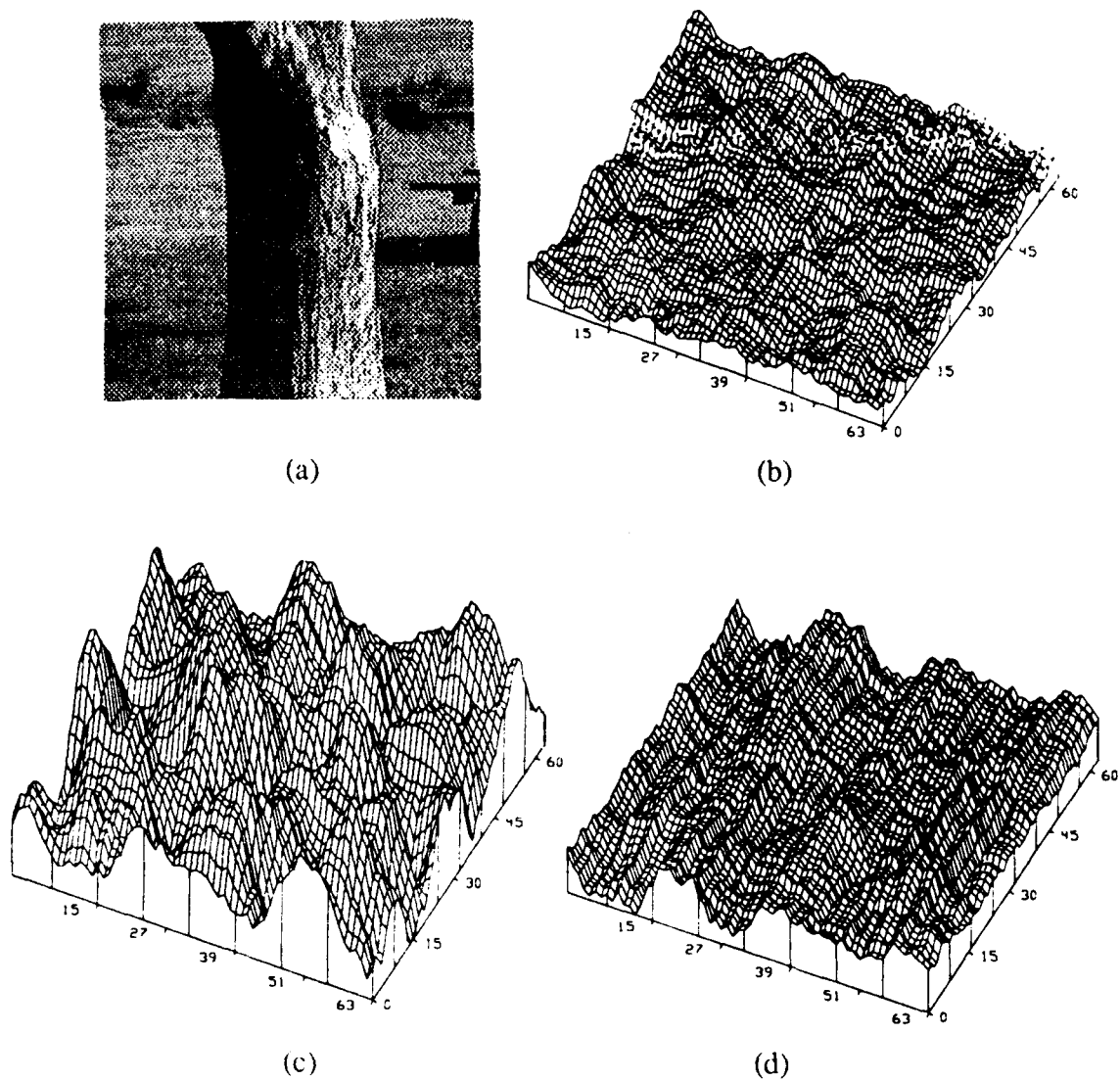


Figure 2.13: Synthesized surface shapes over  $64 \times 64$  sized normal plane patch from (a) A tree image whose surface is covered by the tree bark texture, (b) Pentland's model with the fractal scale  $c=0.9$ , (c) Pentland's model with the fractal scale  $c=1.5$ , (d) 2nd-order AR model with the frequency  $\omega_1=0.25$ ,  $\omega_2=0.025$  in directions of  $m_1$ ,  $m_2$ , respectively.

smooth surface and the textured surface simultaneously, the Fractional Differencing model was suggested in this chapter.

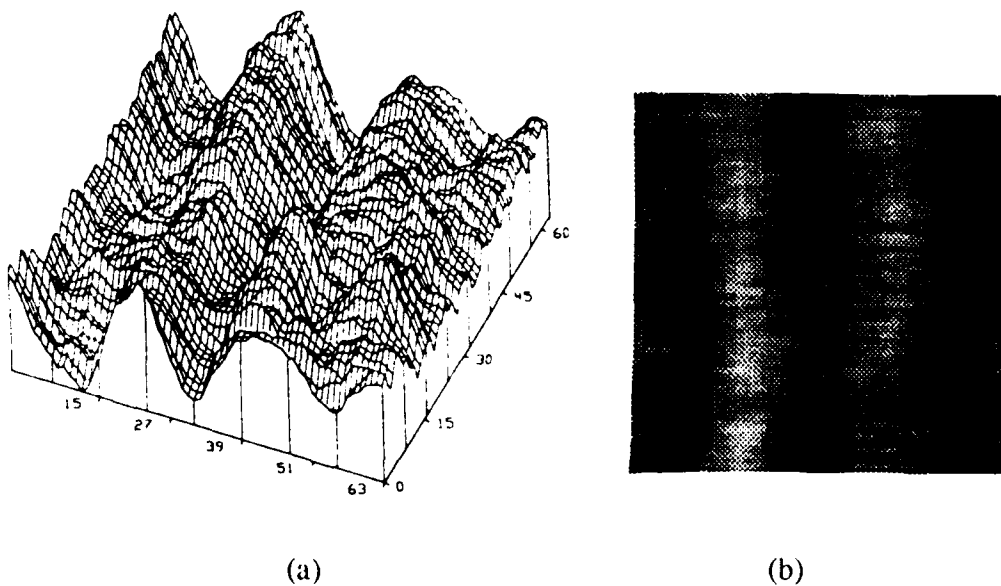


Figure 2.14: Surface shapes obtained from Fractional Differencing Periodic model (2.3.2.3.1): (a) Synthesized surface shape over  $64 \times 64$  sized normal plane patch with the frequency  $\omega_1=0.25$ ,  $\omega_2=0.025$  and the fractal scale  $c=1.5$ ,  $d=0.8$  in direction of  $m_1$ ,  $m_2$ , (b) corresponding surface image.

## CHAPTER 3

### FRACTIONAL DIFFERENCING MODEL AND ESTIMATION

#### 3.1. Introduction

As mentioned previously, the fractional differencing model has an ability to simultaneously represent the coarseness and the pattern of the 3-D texture surface with the fractional differencing parameters  $c$ ,  $d$  and the frequency parameters  $\omega_1$ ,  $\omega_2$ . Also it has the property of being flexible enough to synthesize both long-term and short-term correlation structures of random texture depending on the values of the fractional differencing parameters [101]. For estimating the parameters, comparing with the fractional Brownian random process model [151], the fractional differencing model has a simple estimation scheme sharing the same properties together, because while the fractional Brownian process is a continuous process which follows a certain probability distribution, the fractional differencing model is a discrete process which has a linear function of parameters. A hybrid method which uses both the least square and the maximum likelihood estimates is applied and the estimation and the synthesis are done in frequency domain [67, 127].

### 3.2. Fractional Brownian Model

Brownian motion is a continuous time stochastic process  $B(t)$  with independent Gaussian increments and spectral density  $\omega^{-2}$ . Its derivative is the continuous-time white noise process, which has constant spectral density. Fractional Brownian motion,  $B_F(t)$ , introduced by Mandelbrot and Van Ness [151], is a generalization of these process as follows. Let  $0 < F < 1$  and let  $b_0$  be an arbitrary real number. Define  $B_F(0) = b_0$ ,

$$B_F(t) - B_F(0) = \frac{1}{\Gamma(F + 1/2)} \left\{ \int_{-\infty}^0 [(t-s)^{F-1/2} - (-s)^{F-1/2}] dB(s) \right. \\ \left. + \int_0^t (t-s)^{F-1/2} dB(s) \right\}, \quad \text{for } t > 0, \quad (3.2.1)$$

and similarly for  $t < 0$ . Notice that for  $F = 1/2$ , this definition becomes that of classical Brownian motion  $B(t)$ . This Fractional Brownian motion has the following basic properties [101].

**Property 1:** Fractional Brownian motion with parameter  $F$ , usually  $0 < F < 1$ , is the

$(\frac{1}{2} - F)$ th fractional derivative of Brownian motion.

**Property 2:** The spectral density of fractional Brownian motion is proportional to

$$\omega^{-2F-1}.$$

**Property 3:** The covariance function of fractional Brownian motion is proportional

$$\text{to } |k|^{2F-2}.$$

Thus, the derivative of fractional Brownian motion,  $B'_F(t)$ , may also be thought of as the  $(\frac{1}{2} - F)$ th fractional derivative of continuous-time white noise, to which it reduces

when  $F = \frac{1}{2}$ . One of the possible discrete-time analogues of this continuous-time fractional noise is discrete-time fractional Gaussian noise, which is defined to be a process whose correlation function is the same as that of the process of unit increments  $\Delta B_F(t) = B_F(t) - B_F(t-1)$  of fractional Brownian motion.

However, the modeling ability of fractional Brownian motion noise has sometimes been claimed to be inferior to that of other processes such as the high-order Moving Average (MA) process. This is because of that fractional Brownian model has only three variable parameters, mean, variance and  $F$ , and those are not flexible enough to model the wide range of randomness encountered in practice. Also, it is relatively difficult to estimate parameter  $F$  and to synthesize with it, because of the continuous-time process of this model. Therefore, to give more flexibility of modeling while keeping the same properties as the fractional Brownian model, Fractional Differencing model will be introduced in the next section.

### 3.3. Fractional Differencing Model

#### 3.3.1. 1-D Fractional Differencing Model

The 1-D Fractional Differencing model was suggested by Hosking [101], generalizing the well-known ARIMA model of Box & Jenkins [23], which was originally designed to model a non-stationary random process. A typical 1-D first-order Fractional Differencing model is as follows.

$$y(l) = (1-z^{-1})^{-\frac{c}{2}} \zeta(l) \quad (3.3.1.1)$$

where  $z$  is the delay operator in the direction of  $l$ , and  $\zeta(l)$  is white Gaussian

noise.

This random process model has the property of being flexible to explain both long-term and short-term correlation structures of a time series depending on the values of the fractional differencing parameter  $c$ , and it shares the basic properties with Fractional Brownian motion defined by Mandelbrot [151].

**Theorem 3.3.1.1:** *The spectral density of  $\{y(l)\}$  is  $s(\omega) = (2\sin\frac{1}{2}\omega)^{-c}$  for  $0 < \omega \leq \pi$  and  $s(\omega) \approx \omega^{-c}$  as  $\omega \rightarrow 0$ , assuming that  $\sigma_\zeta^2 = 1$ .*

(Proof) Let  $B(z) = (1-z^{-1})^{-\frac{c}{2}}$ . Then,  $s(z)$  can be written by  $B(z)B^{-1}(z)\sigma_\zeta^2$ . Thus, since  $\sigma_\zeta^2 = 1$ , we have  $s(\omega) = B(e^{j\omega})B(e^{-j\omega})$ . The result follows on substitution of  $B(e^{j\omega}) = (1 - e^{-j\omega})^{-\frac{c}{2}}$ .

■

**Theorem 3.3.1.2:** *The autocovariance function of  $\{y(l)\}$  is*

$$\mathbb{R}_k = 2^{1+\frac{c}{2}} \sin\left(\frac{\pi c}{2}\right) \frac{\Gamma(k+\frac{c}{2})}{\Gamma(k+1-\frac{c}{2})} \cdot \Gamma(1-c), \text{ for } -1 < \frac{c}{2} < \frac{1}{2}, c \neq 0. \quad (3.3.1.2)$$

and the autocorrelation function is given by

$$\rho_k = \frac{\Gamma(1-\frac{c}{2})}{\Gamma(\frac{c}{2})} \cdot \frac{\Gamma(k+\frac{c}{2})}{\Gamma(k+1-\frac{c}{2})} \quad (3.3.1.3)$$

$$\rho_k \approx \frac{\Gamma(1-\frac{c}{2})}{\Gamma(\frac{c}{2})} \cdot k^{c-1} \quad (3.3.1.4)$$

(Proof) The autocovariance, if it exists, will be given by

$$R_k = \int_0^{2\pi} \cos k\omega \, s(\omega) \, d\omega \quad (3.3.1.5)$$

$$= \int_0^{\pi} 2^{-\frac{c}{2}} \cos k\omega (\sin \omega/2)^{-c} \, d\omega. \quad (3.3.1.6)$$

Using the standard formula,

$$\int_0^{\pi} \sin^{\nu-1} x \cos ax \, dx = \frac{\pi \cos a\pi/2}{2^{\nu-1} \cdot \nu \cdot B(\frac{\nu+a+1}{2}, \frac{\nu-a+1}{2})}, \quad (3.3.1.7)$$

we can get (3.3.1.2). Here,  $B(\cdot, \cdot)$  is Beta function. Also, from the definition of the

autocorrelation function,  $\rho_k = \frac{R_k}{R_0}$ . Therefore, (3.3.1.3) follows on substitution of  $R_k$

and  $R_0$ . As  $k \rightarrow \infty$ ,  $\Gamma(k+a)/\Gamma(k+b)$  can be approximated by  $k^{a-b}$ , using the standard approximation derived from Sheppard's formula. Therefore, it follows that the autocorrelation is given by (3.3.1.4). ■

**Definition 3.3.1:** When  $c < 0$ , the Fractional Differencing process (3.3.1.1) has a short-term memory, and when  $c > 0$ , it has a long-term memory.

From Theorem 3.3.1.1 and 3.3.1.2, when  $c > 0$ , the autocorrelation function  $\rho_k$  is positive and decays monotonically and hyperbolically to zero as the lag increases, and the corresponding spectral density  $s(\omega)$  is concentrated at low frequencies:  $s(\omega)$  is a decreasing function of  $\omega$  and  $s(\omega) \rightarrow \infty$  as  $\omega \rightarrow 0$ . Similarly, when  $c < 0$ ,  $s(\omega)$  is dominated at high frequencies:  $s(\omega)$  is an increasing function of  $\omega$  and vanishes at  $\omega = 0$ . Therefore, when  $c < 0$  or  $c > 0$ , the Fractional Differencing process (3.3.1.1) has a short-term or long-term memory, respectively.

**Corollary 3.3.1:** *The Fractional Differencing process is the discrete version of fractional white noise process, and shares the basic properties with Fractional Brownian motion.*

(Proof) Brownian motion is a continuous time stochastic process  $B(t)$  with independent Gaussian increments. Its derivative is the continuous-time white noise process, which has constant spectral density. Fractional Brownian motion,  $B_F(t)$ , is a generalization of these processes. Then, Fractional Brownian motion with parameter  $F$ , usually  $0 < F < 1$ , is equal to the  $(\frac{1}{2} - F)$ th fractional derivative of Brownian motion in Riemann-Liouville sense. The continuous-time fractional noise process is then the derivative of Fractional Brownian motion, thus it may also be thought of as the  $(\frac{1}{2} - F)$ th fractional derivative of continuous-time white noise. Therefore, the Fractional Differencing model (3.3.1.1) is the discrete version of this continuous-time fractional white noise process, and it shares some properties with Fractional Brownian motion [101].

■

### 3.3.2. 2-D Fractional Differencing Model

In 3-D textural surface image, the fractional differencing parameter, which is 'fractal scaling parameter' in the terminology of Pentland [173,176], indicates the roughness of the surface, that is, as the value of the fractal scaling parameter increases, the model represents a 3-D surface textured more roughly. However, Pentland's model based on 2-D fractional Brownian motion process with one fractal scaling parameter has limited modeling ability, because the fractal of surface is assumed to be spatially isotropic. Thus, Pentland's model is not flexible enough to represent the wide range of different texture patterns encountered in practice, especially for the non-stationary random texture. In other words, this model can tell how rough the surface is, but can not tell which pattern the surface is covered with. This limitation can be overcome by using the 2-D Fractional Differencing models as follows.

#### 3.3.2.1. First-order Fractional Differencing Model

As mentioned in previous sections, Pentland's fractional Brownian motion model with one fractal scaling parameter is not flexible enough to present the different texture patterns. However, even from the first-order Fractional Differencing model, we could get more flexibility of modeling, because it contains two different fractal scaling parameters,  $c$ ,  $d$ , in directions of  $l_1$  and  $l_2$ . This model does not require the stationarity of random texture. The typical first-order Fractional Differencing model is as follows.

$$y(l_1, l_2) = (1 - z_1^{-1})^{-\frac{c}{2}} (1 - z_2^{-1})^{-\frac{d}{2}} \zeta(l_1, l_2) \quad (3.3.2.1.1)$$

for  $l_1, l_2 = 0, 1, \dots, N-1$ .

The corresponding DFT of this function is

$$Y(k_1, k_2) = (1 - e^{-j2\pi \frac{k_1}{N}})^{-\frac{c}{2}} (1 - e^{-j2\pi \frac{k_2}{N}})^{-\frac{d}{2}} W(k_1, k_2), \quad (3.3.2.1.2)$$

where  $z_i$  is the delay operator associated with  $l_i$ ,  $\zeta(l_1, l_2)$  is an i.i.d. Gaussian sequence, and  $W(k_1, k_2)$  is the corresponding DFT.

### 3.3.2.2. Second-order Fractional Differencing Periodic Model

The typical second-order Fractional Differencing Periodic (FDP) model is as follows.

$$y(l_1, l_2) = (1 - 2\cos\omega_1 z_1^{-1} + z_1^{-2})^{-\frac{c}{2}} \cdot (1 - 2\cos\omega_2 z_2^{-1} + z_2^{-2})^{-\frac{d}{2}} \zeta(l_1, l_2) \quad (3.3.2.2.1)$$

for  $l_1, l_2 = 0, 1, \dots, N-1$ .

The corresponding DFT of this function is

$$Y(k_1, k_2) = (1 - 2\cos\omega_1 e^{-j2\pi \frac{k_1}{N}} + e^{-j4\pi \frac{k_1}{N}})^{-\frac{c}{2}} \cdot (1 - 2\cos\omega_2 e^{-j2\pi \frac{k_2}{N}} + e^{-j4\pi \frac{k_2}{N}})^{-\frac{d}{2}} W(k_1, k_2), \quad (3.3.2.2.2)$$

where  $z_i$  is the delay operator associated with  $l_i$ ,  $\zeta(l_1, l_2)$  is an i.i.d. Gaussian sequence, and  $W(k_1, k_2)$  is the corresponding DFT.

This model has four different parameters,  $c$  and  $d$  for the fractal scales and  $\omega_1$  and  $\omega_2$  for the frequencies of pattern in the direction of  $l_1$  and  $l_2$ , respectively. Thus, this model represents the roughness of the surface and the pattern of the texture image at the same time even with the different values for the direction of  $l_1, l_2$  separately.

### 3.3.3. Parameter Estimation

Because of the flexibility and the simplicity of Fractional Differencing model, it is attractive in modeling various kinds of time series, including 2-D random texture image. However, the estimation of the fractal scaling parameters  $c, d$  and the frequency parameters  $\omega_1, \omega_2$  is difficult and this difficulty further delayed the application of this model. There have been several approaches for estimating parameters in various kinds of fractional differencing time series since Hosking introduced Fractional Differencing model [101]. For example, Granger and Joyeux [89] approximated this model by a high-order auto-regressive process and estimated the differencing parameter by comparing variances for each different choice of it. Lapsa [121] suggested a maximum-likelihood estimator in the frequency domain and showed the consistency of the estimator. This frequency domain analysis was further studied by Eom, and a hybrid method of least-squares and maximum-likelihood estimations was recently proposed to estimate the fractal scaling parameters and the frequency parameters, respectively [67]. In this thesis, a least-squares or a maximum-likelihood estimation algorithm will be applied to estimate the parameters, based on Eom's algorithm.

### 3.3.3.1. First-order Fractional Differencing Model

The estimation of fractal scaling parameters  $c$  and  $d$  in the first-order fractional differencing model (3.3.2.1.1) can be done by a simple least-square estimation scheme in the frequency domain based on a representation of the logarithm of the process which is linear in the parameters as follows. By applying the logarithm operator to (3.3.2.1.2), we can obtain

$$\begin{aligned} \log |Y(k_1, k_2)| &= -\frac{c}{2} \log |1 - e^{-j2\pi \frac{k_1}{N}}| - \frac{d}{2} \log |1 - e^{-j2\pi \frac{k_2}{N}}| + \log |W(k_1, k_2)| \\ &= -\frac{c}{2} \log |2 \sin(\frac{\pi k_1}{N})| - \frac{d}{2} \log |2 \sin(\frac{\pi k_2}{N})| + \log |W(k_1, k_2)| \end{aligned} \quad (3.3.3.1.1)$$

$$= -\frac{c}{2} \log |2 \sin(\frac{\pi k_1}{N})| - \frac{d}{2} \log |2 \sin(\frac{\pi k_2}{N})| - \alpha + V(k_1, k_2)$$

$$, \text{ for } k_1, k_2 = 0, 1, \dots, N-1 \quad (3.3.3.1.2)$$

where  $\alpha = -E[\log |W(k_1, k_2)|]$  and  $V(k_1, k_2) = \log |W(k_1, k_2)| + \alpha$ .

Then  $\theta = (c, d, \alpha)^T$  can be estimated by minimizing the following cost function.

$$\begin{aligned} J(\theta, \omega_1, \omega_2) &= \sum_{k_1=0}^{N-1} \sum_{k_2=0}^{\lfloor N/2 \rfloor} (\log |Y(k_1, k_2)| + \frac{c}{2} \log |2 \sin \frac{\pi k_1}{N}| \\ &\quad + \frac{d}{2} \log |2 \sin \frac{\pi k_2}{N}| + \alpha)^2 \end{aligned} \quad (3.3.3.1.3)$$

$$= \sum_{k_1=0}^{N-1} \sum_{k_2=0}^{\lfloor N/2 \rfloor} (\log |Y(k_1, k_2)| - \theta^T Q(k_1, k_2))^2 \quad (3.3.3.1.4)$$

Here,

$$Q(k_1, k_2) = \begin{bmatrix} \frac{-1}{2} \log |2 \sin \frac{\pi k_1}{N}| \\ \frac{-1}{2} \log |2 \sin \frac{\pi k_2}{N}| \\ -1 \end{bmatrix} \quad (3.3.3.1.5)$$

Thus, the estimated values will be

$$[\hat{c}, \hat{d}, \hat{\alpha}]^T = \left( \sum_{k_1=0}^{N-1} \sum_{k_2=0}^{\lfloor N/2 \rfloor} Q(k_1, k_2) Q^T(k_1, k_2) \right)^{-1} \left( \sum_{k_1=0}^{N-1} \sum_{k_2=0}^{\lfloor N/2 \rfloor} Q(k_1, k_2) \log |Y(k_1, k_2)| \right) \quad (3.3.3.1.6)$$

### 3.3.3.2. Second-order Fractional Differencing Periodic Model

The estimation of parameters in the Fractional Differencing Periodic model (3.3.2.2.1) can be done in the frequency domain [127].

For estimation, all parameters can be estimated directly from the given data  $Y(k_1, k_2)$ , if we can obtain the likelihood function of  $|Y(k_1, k_2)|$ . Then, since the noise sequence  $\zeta(l_1, l_2)$  is assumed to be white Gaussian,  $W(k_1, k_2)$  and  $Y(k_1, k_2)$  follow the Rayleigh distribution as in the following theorem.

**Theorem 3.3.3.1:** *The modulus of the DFT of the noise sequence,  $\{|W(k_1, k_2)|, k_1=0, 1, \dots, N-1, k_2=0, 1, \dots, \lfloor N/2 \rfloor\}$  and  $\{|Y(k_1, k_2)|, k_1=0, 1, \dots, N-1,$*

$k_2=0,1,\dots,\left\lfloor N/2 \right\rfloor\}$  are the white sequences with the following Rayleigh densities.

$$f_{|W(k_1,k_2)|}(W) = \begin{cases} \frac{2W}{\rho N^2} \exp\left\{-\frac{W^2}{\rho N^2}\right\} & , W \geq 0 \\ 0 & , \text{otherwise} \end{cases}$$

$$f_{|Y(k_1,k_2)|}(Y) = \begin{cases} \frac{2s_{k_1,k_2}^2 Y(k_1,k_2)}{\rho N^2} \exp\left\{-\frac{s_{k_1,k_2}^2 Y^2(k_1,k_2)}{\rho N^2}\right\} & , Y(k_1,k_2) \geq 0 \\ 0 & , \text{otherwise} \end{cases}$$

where

$$s_{k_1,k_2} = \left| 2\cos\left(\frac{2\pi k_1}{N}\right) - 2\cos\omega_1 \right|^{\frac{c}{2}} \left| 2\cos\left(\frac{2\pi k_2}{N}\right) - 2\cos\omega_2 \right|^{\frac{d}{2}}$$

(Proof) Let  $W(k_1,k_2)$  be the DFT of a white noise sequence  $\zeta(l_1,l_2)$  with a normal distribution, that is,

$$\zeta(l_1,l_2) \sim N(0,\rho) \quad , \text{for } l_1,l_2 = 1,2,\dots,N \quad (3.3.3.2.1)$$

Then,  $W(k_1,k_2)$  will follow another normal distribution as follows [27].

$$W(k_1,k_2) \sim N(N \cdot E[\zeta(l_1,l_2)], \rho N^2) \quad (3.3.3.2.2)$$

$$\sim N(0, \rho N^2) \quad (3.3.3.2.3)$$

and

$$\text{Re}(W(k_1,k_2)), \text{Im}(W(k_1,k_2)) \sim N\left(0, \frac{\rho N^2}{2}\right) \quad (3.3.3.2.4)$$

where  $\text{Re}(W)$  and  $\text{Im}(W)$  are the real and the imaginary parts of  $W(k_1,k_2)$ , respectively.

Now, consider the density function of  $|W(k_1, k_2)|$ . Since  $W(k_1, k_2)$  is a complex, defining  $W$  be  $W(k_1, k_2)$ ,

$$|W(k_1, k_2)| = \sqrt{\text{Re}^2(W) + \text{Im}^2(W)} \quad (3.3.3.2.5)$$

Define  $\phi = \tan^{-1}(\frac{\text{Im}(W)}{\text{Re}(W)})$ . Then, we can have the following relations.

$$\text{Re}(W) = |W(k_1, k_2)| \cos\phi \quad (3.3.3.2.6)$$

$$\text{Im}(W) = |W(k_1, k_2)| \sin\phi, \text{ for } |W| > 0 \quad (3.3.3.2.7)$$

Thus, the joint probability density of  $|W|$  and  $\phi$  can be obtained from the Jacobian and the joint probability density of  $\text{Re}(W)$  and  $\text{Im}(W)$  as follows.

$$f_{|W|, \phi}(|W|, \phi) = \frac{1}{\text{Jacobian}} f_{\text{Re}(W), \text{Im}(W)}(\text{Re}(W), \text{Im}(W)) \text{ , for } |W| > 0 \quad (3.3.3.2.8)$$

$$= |W| f_{\text{Re}(W)}(|W| \cos\phi) f_{\text{Im}(W)}(|W| \sin\phi) \quad (3.3.3.2.9)$$

$$= \frac{|W|}{\pi \rho N^2} e^{-\frac{(\text{Re}^2(W) + \text{Im}^2(W))}{\rho N^2}} \quad (3.3.3.2.10)$$

$$\text{where Jacobian} = \begin{vmatrix} \frac{\partial |W|}{\partial \text{Re}(W)} & \frac{\partial |W|}{\partial \text{Im}(W)} \\ \frac{\partial \phi}{\partial \text{Re}(W)} & \frac{\partial \phi}{\partial \text{Im}(W)} \end{vmatrix} \quad (3.3.3.2.11)$$

$$= \frac{1}{|W|} \quad (3.3.3.2.12)$$

Therefore, since  $|W|$  and  $\phi$  are independent, and the density function of  $\phi$ ,  $f_\phi(\phi)$ , is

$$\frac{1}{2\pi},$$

$$f_{|W|, \phi}(|W|, \phi) = f_{|W|}(|W|) \cdot f_\phi(\phi) \quad (3.3.3.2.13)$$

and

$$f_{|W|}(W) = \begin{cases} \frac{2W}{\rho N^2} \exp\left(\frac{-W^2}{\rho N^2}\right) & , W \geq 0 \\ 0 & , otherwise \end{cases} \quad (3.3.3.2.13)$$

Now, set

$$s_{k_1, k_2} = \left| 2\cos\left(\frac{2\pi k_1}{N}\right) - 2\cos\omega_1 \right|^{\frac{c}{2}} \left| 2\cos\left(\frac{2\pi k_2}{N}\right) - 2\cos\omega_2 \right|^{\frac{d}{2}} \quad (3.3.3.2.14)$$

Then, we can have

$$|Y(k_1, k_2)| = s_{k_1, k_2}^{-1} |W(k_1, k_2)| \quad (3.3.3.2.15)$$

Thus, the density function of  $|Y(k_1, k_2)|$  can be represented by following equations.

$$f_{|Y(k_1, k_2)|}(Y) = s_{k_1, k_2} f_{|W(k_1, k_2)|}(s_{k_1, k_2} Y(k_1, k_2)) \quad (3.3.3.2.16)$$

$$= \begin{cases} \frac{2s_{k_1, k_2}^2 Y(k_1, k_2)}{\rho N^2} \exp\left\{ \frac{-s_{k_1, k_2}^2 Y^2(k_1, k_2)}{\rho N^2} \right\} & , Y(k_1, k_2) \geq 0 \\ 0 & , otherwise \end{cases}$$

■

From these probabilistic properties, the estimation of parameters can be done by a hybrid method of Least Square and Maximum Likelihood estimations, which was suggested by Eom [67]. For LS estimation, if the values of parameters  $\omega_1, \omega_2$  are set, then  $\theta = (c, d, \alpha)^T$  can be estimated by minimizing the following cost function.

$$J(\theta, \omega_1, \omega_2) = \sum_{k_1=0}^{N-1} \sum_{k_2=0}^{\lfloor N/2 \rfloor} \left( \log |Y(k_1, k_2)| + \frac{c}{2} \log \left| 2\cos\frac{2\pi k_1}{N} - 2\cos\omega_1 \right| \right.$$

$$+ \frac{d}{2} \log \left| 2 \cos \frac{2\pi k_2}{N} - 2 \cos \omega_2 \right| + \alpha)^2 \quad (3.3.3.2.17)$$

$$= \sum_{k_1=0}^{N-1} \sum_{k_2=0}^{\lfloor N/2 \rfloor} (\log |Y(k_1, k_2)| - \theta^T Q(k_1, k_2))^2 \quad (3.3.3.2.18)$$

where  $\alpha = -E[\log |W(k_1, k_2)|]$ ,  $\theta = (c, d, \alpha)^T$ .

Here,

$$Q(k_1, k_2) = \begin{bmatrix} -\frac{1}{2} \log \left| 2 \cos \frac{2\pi k_1}{N} - 2 \cos \omega_1 \right| \\ -\frac{1}{2} \log \left| 2 \cos \frac{2\pi k_2}{N} - 2 \cos \omega_2 \right| \\ -1 \end{bmatrix} \quad (3.3.3.2.19)$$

Thus, the estimated values will be

$$[\hat{c}, \hat{d}, \hat{\alpha}]^T = \left( \sum_{k_1=0}^{N-1} \sum_{k_2=0}^{\lfloor N/2 \rfloor} Q(k_1, k_2) Q^T(k_1, k_2) \right)^{-1} \left( \sum_{k_1=0}^{N-1} \sum_{k_2=0}^{\lfloor N/2 \rfloor} Q(k_1, k_2) \log |Y(k_1, k_2)| \right) \quad (3.3.3.2.20)$$

Also, ML estimators of  $\omega_1, \omega_2$  can be calculated by maximizing the log-likelihood function  $L(Y; \theta, \omega_1, \omega_2)$  with  $\hat{\alpha}$  estimated from above.

$$\begin{aligned} L(Y; \theta, \omega_1, \omega_2) &= \sum_{k_1=0}^{N-1} \sum_{k_2=0}^{\lfloor N/2 \rfloor} \log |Y(k_1, k_2)| - \sum_{k_1=0}^{N-1} \sum_{k_2=0}^{\lfloor N/2 \rfloor} \log \left( \frac{\rho N^2}{2} \right) \\ &+ \frac{c}{2} N \sum_{k_1=0}^{N-1} \log \left| 2 \left( \cos \frac{2\pi k_1}{N} - \cos \omega_1 \right) \right| + d N \sum_{k_2=0}^{\lfloor N/2 \rfloor} \log \left| 2 \left( \cos \frac{2\pi k_2}{N} - \cos \omega_2 \right) \right| \end{aligned}$$

$$- \frac{1}{\rho N^2} \sum_{k_1=0}^{N-1} \sum_{k_2=0}^{\lfloor N/2 \rfloor} \left| 2 \cos \frac{2\pi k_1}{N} - \cos \omega_1 \right|^c \cdot \left| 2 \cos \frac{2\pi k_2}{N} - \cos \omega_2 \right|^d \cdot |Y(k_1, k_2)|^2 \quad (3.3.3.2.21)$$

where  $\rho$  is a variance of  $\zeta(l_1, l_2)$  and can be estimated by the following equation in mean square sense.

$$\hat{\rho} = \frac{1}{N^2} \exp \left\{ \gamma - 2\hat{\alpha} - \frac{\pi^2}{6N^2} \right\} \quad (3.3.3.2.22)$$

where  $\gamma$  is Euler's constant ( $= 0.5772157$ ) [67].

Therefore, the estimation scheme can be summarized as follows:

(Estimation Algorithm)

- Step 1: Choose resonant frequencies  $\omega_1, \omega_2$  in the range of  $[0, \frac{\pi}{2}]$ .
- Step 2: With the given values of  $\omega_1$  and  $\omega_2$ , estimate  $c$ ,  $d$ , and  $\alpha$  by LS estimation algorithm (3.3.3.2.20).
- Step 3: Using  $\hat{\alpha}$ , compute the estimate of the variance of  $\rho$ ,  $\zeta(l_1, l_2)$ , by equation (3.3.3.2.22).
- Step 4: Using the estimates  $\hat{c}$ ,  $\hat{d}$  and  $\hat{\rho}$  found in Steps 2 and 4, maximize the likelihood function given by (3.3.3.2.21) with respect to  $\omega_1$  and  $\omega_2$ .
- Step 5: Using the estimates  $\hat{\omega}_1$  and  $\hat{\omega}_2$ , repeat Step 2 to Step 4 until the estimates have no significant change in successive iterations.

### 3.4. Conclusions

In this chapter, various types of Fractional Differencing model have been considered and compared with the Fractional Brownian model. The Fractional Brownian model has been used for measuring the roughness of a surface by researchers. However, the modeling ability of Fractional Brownian motion noise is limited, because this model has only three variable parameters, mean, variance and fractal scale  $F$ , thus, those are not enough to model the wide range of randomness encountered in practice. Also, it is relatively difficult to estimate the fractal scale  $F$  and to synthesize with it, because of its continuous-time process. To give more flexibility of modeling keeping the same properties of Fractional Brownian motion process, the Fractional Differencing model is suggested. The Fractional Differencing model is a discrete version of the Fractional Brownian model. Thus, this model shares the same properties of the Fractional Brownian process and has a relatively simple structure. In this model, Fractal scale can have two different values in the directions of  $x$  and  $y$ , and this gives more flexibility for modeling non-isotropic distributed random texture. Additionally, this model can be extended to the second-order of process to provide another pair of frequency parameters  $\omega_1, \omega_2$ . Using this 2nd-order Fractional Differencing model, the roughness and the texture pattern of a surface can be represented simultaneously. Parameter estimation schemes for each model are also developed based on the least-square estimation and the maximum likelihood estimation.

## **CHAPTER 4**

### **SHAPE FROM A SHADED AND TEXTURED SURFACE IMAGE**

#### **4.1. Introduction**

An important task in computer vision is the recovery of 3-D scene information from single 2-D images. 3-D analysis of an image can be broken down into two main categories, Shape-from-shading and Shape-from-texture. The Shape-from-shading technique uses the reflectance map which shows scene radiance as a function of the surface gradient and the distribution of light sources to extract 3-D surface information from image data [99, 144, 172]. On the other hand, the Shape-from-texture analysis technique uses the texture pattern instead of shading to extract 3-D structure. Since texture gradients behave like intensity gradients, the shape of a surface can be inferred from the pattern of a texture on the surface by applying statistical texture analysis [6, 135, 206, 221].

However, for describing a natural scene image, each of the above approaches has its own limitation. The Shape-from-shading technique is applicable only under the assumption that the surface is smooth enough to have clear radiance information, while the Shape-from-texture technique requires the surface to be relatively complex so that texture information can be extracted. Thus, neither technique is suitable to recover 3-D structure information from a natural scene, because both radiance and

texture information coexist within the surface of a natural scene. Therefore, a robust technique is needed to handle this shortcoming. Recently, the fractal scaling parameter was introduced to measure the coarseness of the surface, and applied to represent the natural scene surface [176]. However, this fractal model is not enough to represent the real 3-D texture image, because even though two surfaces are estimated to have the same fractal scales, these surfaces can have different texture patterns.

In this chapter, a composite model of Shape-from-shading and Shape-from-texture is developed to represent a 3-D surface image considering the scene image as the superposition of a smooth shaded image and a random texture image. The orthographical projection is adapted to take care of the non-isotropic distribution function due to the slant and tilt of a 3-D texture surface, and the Fractional Differencing Periodic model is chosen because this model is able to simultaneously represent the coarseness and the pattern of the 3-D texture surface with the fractional differencing parameters  $c$ ,  $d$  and the frequency parameters  $\omega_1$ ,  $\omega_2$ , and it has the property of being flexible enough to synthesize both long-term and short-term correlation structures of random texture depending on the values of the fractional differencing parameter  $c$  and  $d$ . Since the object is described by a model involving several free parameters and the values of these parameters are determined directly from its projected image, it is possible to extract 3-D information and texture pattern directly from the given intensity values of the image without any pre-processing. Thus, the cumulative error obtained from each pre-processing can be minimized. For estimating the parameters, a hybrid method which uses both the least square and the maximum likelihood estimates is applied and the estimation and the synthesis are done in frequency domain based on the local patch analysis. By using this model, the integrability problem which might occur in spatial domain analysis can be avoided,

because only one inverse Fourier transform needs to be taken at the end of procedure to get the whole image.

The organization of this chapter is as follows. In section 4.2., we introduce the image model  $i(l_1, l_2)$  which is obtained by superposing the deterministic function  $x(l_1, l_2)$  and the random function  $y(l_1, l_2)$ , and the relationship between the different directions of a 3-D surface. In section 4.2.1-3, an estimation scheme for the illumination direction, the modified reflectance map function for  $x(l_1, l_2)$ , and the orthographically projected Fractional Differencing Periodic function for  $y(l_1, l_2)$  are introduced. Section 4.3.1 outlines the estimation scheme for the parameters in the composite model. Section 4.3.2 then discusses some simulation results carried out to demonstrate the performance of the proposed algorithm, followed by Section 4.4 which concludes the paper.

## 4.2. Model Of 3-D Texture Surface Image

The surface shape is usually defined in terms of the viewer's coordinate system. This system has axes  $l_1, l_2, l_3$  with the  $l_3$  axis in the viewing direction. The observed intensity function  $i(l_1, l_2)$  of local shape of a 3-D surface can be considered as the sum of a deterministic function  $x(l_1, l_2)$ , and a statistical random function  $y(l_1, l_2)$ , whose expected value is zero:

$$i(l_1, l_2) = x(l_1, l_2) + y(l_1, l_2) \quad (4.2.1)$$

and

$$E \{i(l_1, l_2)\} = x(l_1, l_2) \quad (4.2.2)$$

Thus,  $x(l_1, l_2)$  can be simply estimated by smoothing, i.e., taking the average of intensity values in the proper size of window. Then  $y(l_1, l_2)$  can be estimated by

subtracting this function from the original image  $i(l_1, l_2)$ . Figure 4.1 shows this superposition in a simple 1-D case. Note that these intensity functions do not represent the actual shape of image, because the shading variations are caused by changes in surface orientation relative to the illumination direction  $\mathbf{L}$ . Therefore,  $x(l_1, l_2)$  and  $y(l_1, l_2)$  need to be projected to the illumination direction to extract the shape information.

Let  $\sigma_L, \tau_L$  be the slant and tilt of illumination direction  $\mathbf{L}$  in the coordination system with  $l_1, l_2, l_3$ . The direction  $\mathbf{L}$  induces a coordinate system with axes  $i_1, i_2, i_3$ , and this is derived from the following transformation.

$$\begin{bmatrix} i_1 \\ i_2 \\ i_3 \end{bmatrix} = \begin{bmatrix} \cos\sigma_L \cos\tau_L & \cos\sigma_L \sin\tau_L & -\sin\tau_L \\ -\sin\tau_L & \cos\tau_L & 0 \\ \sin\sigma_L \cos\tau_L & \sin\sigma_L \sin\tau_L & \cos\sigma_L \end{bmatrix} \begin{bmatrix} l_1 \\ l_2 \\ l_3 \end{bmatrix} \quad (4.2.3)$$

Here,  $i_3$  is the illumination direction  $\mathbf{L}$ , and  $l_3$  is the viewing direction.

The surface normal,  $\mathbf{N}$ , is another important direction of 3-D geometry. If we define a new coordinate system with axes,  $m_1, m_2, m_3$ , having the  $m_3$ -axis in the surface normal direction, these axes can be derived from the coordinate system of viewing direction, i.e.,  $l_1, l_2, l_3$ , by using a coordination transform similar to the above with different values of tilt  $\tau$  and slant  $\sigma$ .

$$\begin{bmatrix} l_1 \\ l_2 \\ l_3 \end{bmatrix} = \begin{bmatrix} \cos\sigma \cos\tau & \cos\sigma \sin\tau & -\sin\tau \\ -\sin\tau & \cos\tau & 0 \\ \sin\sigma \cos\tau & \sin\sigma \sin\tau & \cos\sigma \end{bmatrix} \begin{bmatrix} m_1 \\ m_2 \\ m_3 \end{bmatrix} \quad (4.2.4)$$

Refer Figure 2.1 for the relations between these three different directions and the four different tilt and slant parameters,  $\sigma_L, \tau_L, \sigma$ , and  $\tau$ .

Let  $x'(m_1, m_2)$  and  $y'(m_1, m_2)$  be a deterministic and a random function respectively, defined on the surface normal image plane, i.e.,  $m_3=0$ . Then,

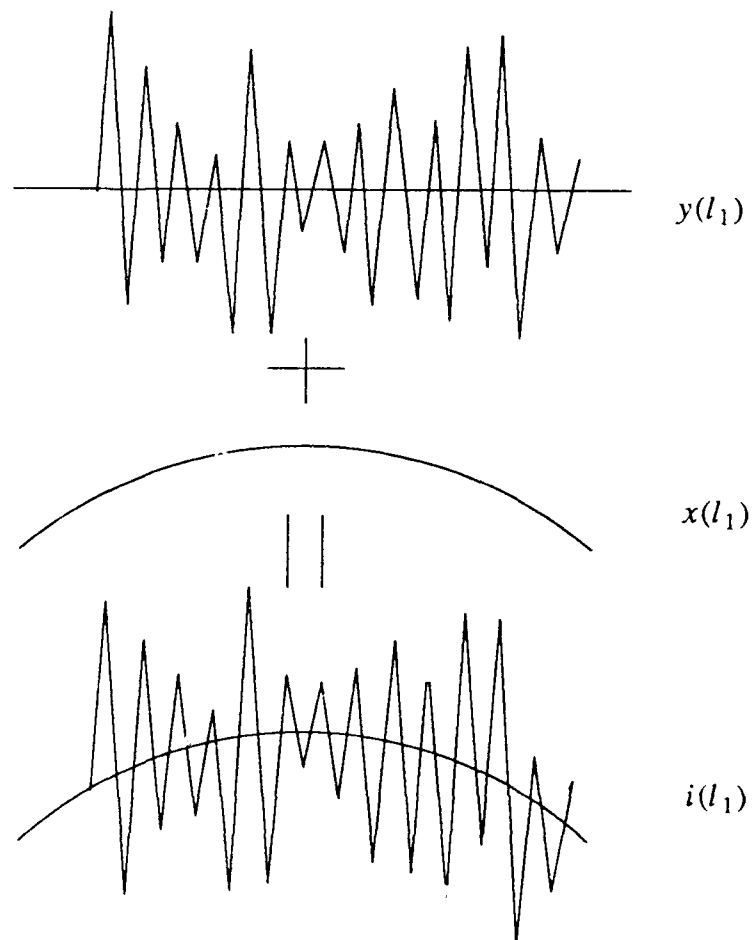


Figure 4.1: Superposition of a random and a deterministic functions in 1-D case.

$z'(m_1, m_2)$ , defined as the sum of these two functions, is merely the depth function  $z$ , observed from the surface normal. However, note that  $y'(m_1, m_2)$  is not the rotated function of  $y(l_1, l_2)$  but the projected function of  $y(l_1, l_2)$  to the  $m_1-m_2$  plane so that they may satisfy the superposition property. Figure 4.2 depicts these relations between functions.

#### 4.2.1. Model Of The Deterministic Component $x$

As discussed before, a 3-D surface image can be considered to be the superposition of a texture image and a smooth shaded image. This smooth shaded image can be represented by the deterministic function  $x(l_1, l_2)$ . Thus, if the illumination direction values for the whole image are given, the surface orientation parameters slant,  $\sigma$ , and tilt,  $\tau$ , can be estimated from  $x(l_1, l_2)$  representing a smooth surface by Shape-from-shading analysis.

Pioneering work on the inference of shape-from-shading was done by Horn [99] and his co-workers. To extract the 3-D shape function  $H(\cdot, \cdot)$  from a single 2-D image, they used the reflectance map, which shows the intensity of the image as a function of the surface gradient and the illumination direction.

$$x(l_1, l_2) = \frac{p \cos \tau_L \sin \sigma_L + q \sin \tau_L \sin \sigma_L + \cos \sigma_L}{(p^2 + q^2 + 1)^{1/2}} \triangleq R(p, q) \quad (4.2.2.1)$$

where  $R(p, q)$  : Reflectance map function

$$p = \frac{\partial}{\partial l_1} H(l_1, l_2), \quad q = \frac{\partial}{\partial l_2} H(l_1, l_2)$$

$H(l_1, l_2)$  : 3-D shape function from the viewing direction.

$\tau_L, \sigma_L$  : Tilt, slant of the illumination direction

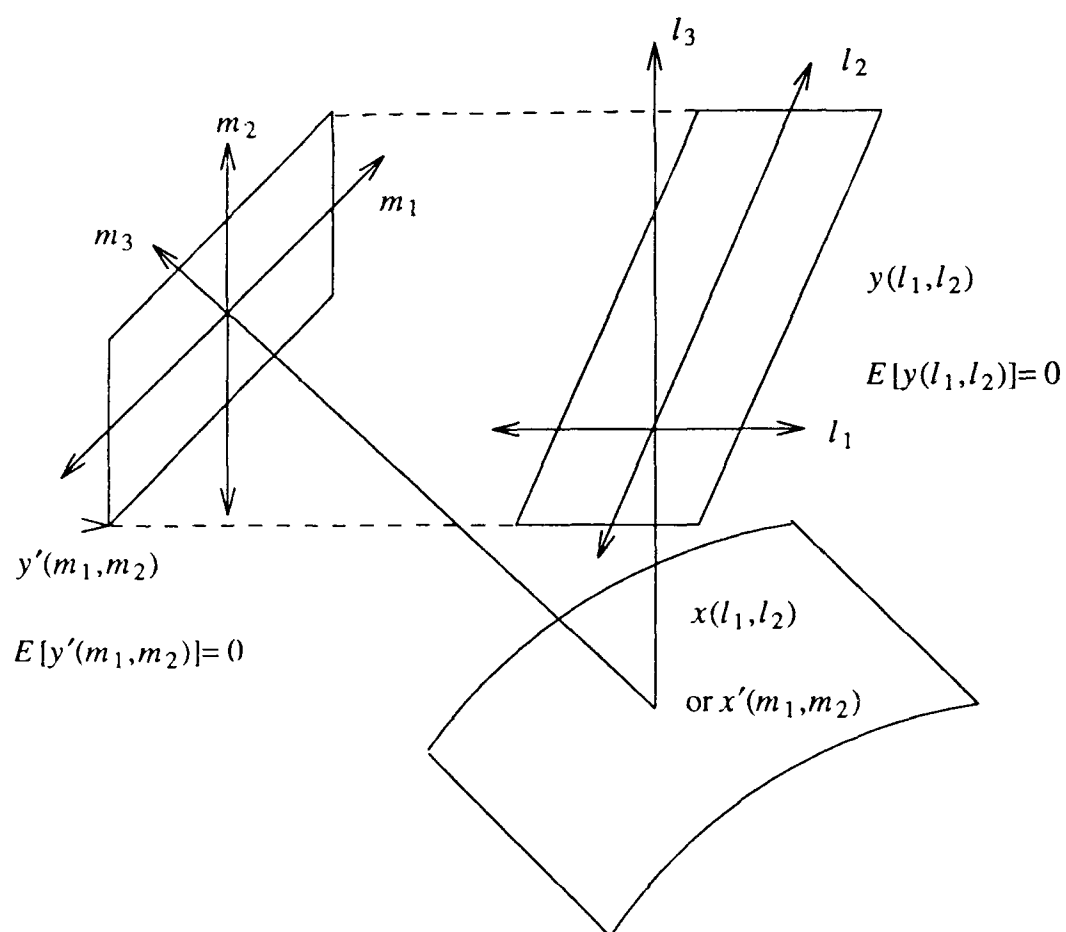


Figure 4.2: 3-D Geometry of the functions  $x$ ,  $y$ ,  $x'$ ,  $y'$ .

Here, from the relationship between the tilt  $\tau$ , the slant  $\sigma$  of the surface and  $p, q$

$$\tau = \tan^{-1}\left(\frac{q}{p}\right), \quad \sigma = \cos^{-1} \frac{1}{\sqrt{p^2+q^2+1}} \quad (4.2.2.2.a)$$

$$p = \tan\sigma\cos\tau, \quad q = \tan\sigma\sin\tau, \quad (4.2.2.2.b)$$

we can modify (4.2.2.1) to the function of  $\sigma, \tau, \sigma_L$ , and  $\tau_L$  as

$$x(l_1, l_2) = \sin\sigma\cos\tau\cos\tau_L\sin\sigma_L + \sin\sigma\sin\tau\sin\tau_L\sin\sigma_L + \cos\sigma\cos\sigma_L \quad (4.2.2.3)$$

Construction of 3-D shape can be achieved by solving  $\sigma, \tau$  in terms of  $x(l_1, l_2)$  at each point, and integrating those values. However, this approach needs the solutions of at least two difficult problems. First, this is an ill-posed problem because there are two unknown parameters and only one equation to be solved. Thus, we need an additional constraint to have a unique solution. Second, the final integrated shape can be different from the original shape, due to the cumulation of estimation errors.

To get a unique solution, the calculus of variation methods were used by minimizing the estimation error after adding one constraint for the smoothness [100] or integrability [76]. To handle the cumulative error, Pentland [172] suggested local shape analysis which deals with only the local areas instead of a whole image. However, Pentland's technique has severe trouble in integrating all local area surface information. Recently, Pentland [169] developed another technique for solving the integrability problem. He suggested analysis in the frequency domain, instead of in the spatial domain. By using this method, the integrability problem can be avoided, because only one inverse Fourier transform needs to be taken at the end of the procedure. However, since the calculation of a convolution is required in the frequency domain to handle a simple multiplication operation in the spatial domain, calculation will be complicated. In this paper, these ill-posed and the integrability

problems will be handled by an additional constraint from the texture pattern and frequency domain analysis, respectively. (This will be discussed in detail later.)

#### 4.2.2. Model Of The Random Component $y$

The random component  $y(l_1, l_2)$  of the intensity function  $i(l_1, l_2)$  can not be simply obtained by taking coordinate transformation to  $y'(m_1, m_2)$ , defined on the surface normal plane image. Because the random function  $y(l_1, l_2)$  was assumed to be a 2-D random function, whose expectation value,  $E[y(l_1, l_2)]$ , is zero, to satisfy the superposition properties, this function should rather be considered as the function obtained after projecting  $y'(m_1, m_2)$  to the viewer's direction (as shown in Figure 4.2). Thus, if we can model  $y'(m_1, m_2)$  properly,  $y(l_1, l_2)$  will be obtained by projecting this to the viewer's direction  $L$ .

##### 4.2.2.1. Fractional Differencing Periodic Model For $y'(m_1, m_2)$

The random function  $y'(m_1, m_2)$ , defined on the surface normal plane image, can be approximated by a 2-D random field model, which is distributed over the surface normal plane (as shown in Figure 4.1). Note that since this model is based on a 2-D texture model, it will fit the plane surface more than any other shape of surface. Thus, we apply this model to the local shape of the image because the local shape will be closer and closer to the plane surface when we take a smaller patch.

Among the various random field models, the Fractional Differencing Periodic model is chosen to represent this random texture surface in this chapter. This random process model has the property of being flexible enough to explain both long-term and

short-term correlation structures of a time series depending on the values of the fractional differencing parameter  $c$ , that is, when  $c < 0$ , the fractional differencing process has a short-term memory, and when  $c > 0$ , it has a long-term memory (Theorem 3.3.1). Also it shares the basic properties with Fractional Brownian motion defined by Mandelbrot [151] (Theorem 3.3.2).

In 3-D textural surface image, the fractional differencing parameter, which is 'fractal scaling parameter' in the terminology of Pentland [173,176], indicates the roughness of the surface, that is, as the value of the fractal scaling parameter increases, the model represents a 3-D surface textured more roughly. However, Pentland's 2-D model with one fractal scaling parameter has limited modeling ability, because the fractal of surface is assumed to be spatially isotropic. Thus, Pentland's model is not flexible enough to represent the wide range of different texture patterns encountered in practice, especially non-stationary random texture. In other words, this model can tell how rough the surface is, but can not tell which pattern the surface is covered with. This limitation can be overcome by using the 2-D Fractional Differencing Periodic model as follows [67].

$$y'(m_1, m_2) = (1 - 2\cos\omega_1 z'_1{}^{-1} + z'_1{}^{-2})^{-\frac{c}{2}} \cdot (1 - 2\cos\omega_2 z'_2{}^{-1} + z'_2{}^{-2})^{-\frac{d}{2}} \zeta'(m_1, m_2) \quad (4.2.3.1.1)$$

for  $m_1, m_2 = 0, 1, \dots, N-1$ .

The corresponding DFT of this function is

$$Y'(k_1, k_2) = (1 - 2\cos\omega_1 e^{-j2\pi\frac{k_1}{N}} + e^{-j4\pi\frac{k_1}{N}})^{-\frac{c}{2}}$$

$$\cdot (1 - 2\cos\omega_2 e^{-j2\pi\frac{k_2}{N}} + e^{-j4\pi\frac{k_2}{N}})^{-\frac{d}{2}} W'(k_1, k_2), \quad (4.2.3.1.2)$$

where  $z'_i$  is the delay operator associated with  $m_i$ ,  $\zeta'(m_1, m_2)$  is an i.i.d. Gaussian sequence, and  $W'(k_1, k_2)$  is the corresponding DFT.

This model has four different parameters,  $c$  and  $d$  for the fractal scales and  $\omega_1$  and  $\omega_2$  for the frequencies of pattern in the direction of  $m_1$  and  $m_2$ , respectively. Thus, this model represents the roughness of the surface and the pattern of the texture image at the same time even with the different values for the direction of  $m_1, m_2$  separately.

#### 4.2.2.2 Orthographically Projected Fractional Differencing Periodic Model For $y(l_1, l_2)$

The statistical model of the intensity function  $y(l_1, l_2)$  cannot be simply obtained by rotating the coordinate axes because the expected values of both  $y'(m_1, m_2)$  and  $y(l_1, l_2)$  must be zero over the planes to satisfy the superposition properties. Therefore, such a function  $y(l_1, l_2)$  that satisfies this requirement can be obtained by projecting function  $y'(m_1, m_2)$  orthographically to the viewer's image plane. Figure 4.2 shows this projection.

A new coordinate system of the orthographically projected image from the viewing direction,  $l_1-l_2$ , can be obtained from the following two coordinate transformations.

$$\begin{bmatrix} l'_1 \\ l'_2 \end{bmatrix} = \begin{bmatrix} \cos\tau & -\sin\tau \\ \sin\tau & \cos\tau \end{bmatrix} \begin{bmatrix} m_1 \\ m_2 \end{bmatrix}, \quad (4.2.3.2.1)$$

and

$$\begin{bmatrix} l_1 \\ l_2 \end{bmatrix} = \begin{bmatrix} 1 & 0 \\ 0 & \cos\sigma \end{bmatrix} \begin{bmatrix} l'_1 \\ l'_2 \end{bmatrix} \quad (4.2.3.2.2)$$

Here,  $\tau$  is the angle between  $m_1$  and  $l'_1$  axes and  $\sigma$  is the rotational angle based on  $l'_1$ -axis (Refer Figure 2.10).

Hence, the coordinate transformation of the orthographic projection between the  $m_1$ - $m_2$  system and  $l_1$ - $l_2$  system can be given as follows [110].

$$\begin{bmatrix} l_1 \\ l_2 \end{bmatrix} = \begin{bmatrix} \cos\tau & -\sin\tau \\ \sin\tau & \cos\tau \end{bmatrix} \begin{bmatrix} 1 & 0 \\ 0 & \cos\sigma \end{bmatrix} \begin{bmatrix} \cos\tau & -\sin\tau \\ \sin\tau & \cos\tau \end{bmatrix}^{-1} \begin{bmatrix} m_1 \\ m_2 \end{bmatrix} \quad (4.2.3.2.3)$$

$$= \begin{bmatrix} \cos^2\tau + \cos\sigma \sin^2\tau & (1 - \cos\sigma)\sin\tau\cos\tau \\ (1 - \cos\sigma)\sin\tau\cos\tau & \sin^2\tau + \cos\sigma \cos^2\tau \end{bmatrix} \begin{bmatrix} m_1 \\ m_2 \end{bmatrix} \quad (4.2.3.2.4)$$

Thus,

$$\begin{bmatrix} m_1 \\ m_2 \end{bmatrix} = \frac{1}{\cos\sigma} \begin{bmatrix} \sin^2\tau + \cos\sigma \cos^2\tau & (\cos\sigma - 1)\sin\tau\cos\tau \\ (\cos\sigma - 1)\sin\tau\cos\tau & \cos^2\tau + \cos\sigma \sin^2\tau \end{bmatrix} \begin{bmatrix} l_1 \\ l_2 \end{bmatrix} \quad (4.2.3.2.5)$$

A more detailed discussion on the orthographical projection and some examples to demonstrate this projection were given in section 2.3.1.1 (Figure 2.11).

As a result of the coordinate transform (4.2.3.2.5), the model of intensity function  $y(l_1, l_2)$  can be obtained from the Fractional Differencing Periodic model of  $y'(m_1, m_2)$  as follows.

Let

$$y(l_1, l_2) = (1 - 2\cos\omega_1 z_1^{-1} + z_1^{-2})^{-\frac{c}{2}} (1 - 2\cos\omega_2 z_2^{-1} + z_2^{-2})^{-\frac{d}{2}} \zeta(l_1, l_2) \quad (4.2.3.2.6)$$

where  $z_1, z_2$  are the delay operators, corresponding to  $l_1$  and  $l_2$ , respectively.

By the definition of DFT,  $W(k_1, k_2)$  corresponding to white noise sequence  $\zeta(l_1, l_2)$  is

$$W(k_1, k_2) = \sum_{m_1=0}^{N-1} \sum_{m_2=0}^{N-1} \zeta(l_1, l_2) \exp[-j\frac{2\pi}{N}(m_1 k_1 + m_2 k_2)] \quad (4.2.3.2.7)$$

and, from (4.2.3.2.5),

$$\begin{aligned} W(k_1, k_2) = \sum_{l_1=0}^{N-1} \sum_{l_2=0}^{N-1} \zeta(l_1, l_2) \exp[-j\frac{2\pi}{N \cos\sigma} [((\sin^2\tau + \cos\sigma \cos^2\tau)k_1 \\ + (\cos\sigma - 1)\sin\tau \cos\tau k_2)l_1 + ((\cos\sigma - 1)\sin\tau \cos\tau k_1 \\ + (\cos^2\tau + \cos\sigma \sin^2\tau)k_2)l_2]] \end{aligned} \quad (4.2.3.2.8)$$

Thus, as in [111], we can define

$$z_1 = z'_1 \frac{\sin^2\tau + \cos\sigma \cos^2\tau}{\cos\sigma} z'_2 \frac{(\cos\sigma - 1)\sin\tau \cos\tau}{\cos\sigma} \quad (4.2.3.2.9a)$$

$$z_2 = z'_1 \frac{(\cos\sigma - 1)\sin\tau \cos\tau}{\cos\sigma} z'_2 \frac{\cos^2\tau + \cos\sigma \sin^2\tau}{\cos\sigma} \quad (4.2.3.2.9b)$$

and

$$n_1 = \frac{1}{\cos\sigma} [(\sin^2\tau + \cos\sigma \cos^2\tau)k_1 + (\cos\sigma - 1)\sin\tau \cos\tau k_2], \quad (4.2.3.2.10a)$$

$$n_2 = \frac{1}{\cos\sigma} [(\cos\sigma - 1)\sin\tau \cos\tau k_1 + (\cos^2\tau + \cos\sigma \sin^2\tau)k_2] \quad (4.2.3.2.10b)$$

Thus, from the orthographical projection, we can set

$$W(k_1, k_2) = W'(n_1, n_2) \quad (4.2.3.2.11)$$

Therefore, with these relations, we can have the projected version of  $Y'(k_l, k_2)$ , which is DFT of  $y(l_1, l_2)$  as follows.

$$Y(k_1, k_2) = (1 - 2\cos\omega_1 e^{-j2\pi\frac{n_1}{N}} + e^{-j4\pi\frac{n_1}{N}})^{-\frac{c}{2}} \cdot (1 - 2\cos\omega_2 e^{-j2\pi\frac{n_2}{N}} + e^{-j4\pi\frac{n_2}{N}})^{-\frac{d}{2}} W(k_1, k_2) \quad (4.2.3.2.12)$$

Note that the fractal scaling parameters  $c$  and  $d$  remain same as the ones before projecting because of their scaling invariance property [101, 125].

#### 4.3. Projected Texture On The 3-D Surface

As discussed in previous chapters, the intensity function of an image,  $i(l_1, l_2)$ , can be represented by the superposition of a deterministic function  $x(l_1, l_2)$  and a random function  $y(l_1, l_2)$ . Therefore, if we can estimate all parameters, that is,  $\sigma, \tau$  for the surface orientation and  $c, d, \omega_1, \omega_2$  for the pattern of texture from the intensity function  $z$  directly, then we can get better estimates than the ones from the separate procedures for each  $x$  and  $y$  function. It is obvious that the estimation error from one procedure will cause another estimation error, thus, the errors will be cumulated. For that reason, in this chapter, a composite model of Shape-from-shading and Shape-from-texture will be discussed.

Consider the reflectance map function (4.2.2.3) for  $x$  and the 2-D orthographically projected Fractional Differencing Periodic model (4.2.3.2.6) for  $y$ . Then the intensity function  $z$  can be represented by

$$i(l_1, l_2) = \epsilon [\sin\sigma \cos\tau \cos\tau_L \sin\sigma_L + \sin\sigma \sin\tau \sin\tau_L \sin\sigma_L + \cos\sigma \cos\sigma_L] \\ + (1 - 2\cos\omega_1 z_1^{-1} + z_1^{-2})^{-\frac{c}{2}} (1 - 2\cos\omega_2 z_2^{-1} + z_2^{-2})^{-\frac{d}{2}} \xi(l_1, l_2) \quad (4.3.1)$$

where  $\epsilon$  is the normalization factor, and  $z_1$  and  $z_2$  are same as defined by (4.2.3.2.9a) and (4.2.3.2.9b), respectively.

Here, notice that the normalization factor  $\epsilon$  should be multiplied to the reflectance map function  $R(\sigma, \tau)$ , because  $R(\sigma, \tau)$  is the normalized function which has maximum value 1. Because our model is based on the assumption that each patch is a slanted and tilted plane, the value of the deterministic function  $x(l_1, l_2)$  is a constant over each patch, the best guess of the value of  $\epsilon$  is the maximum value among the average intensities of the patches,

$$\epsilon = \underset{i=1, \dots, M}{\text{Maximum}} \left[ \frac{1}{N'^2} \sum_{l_1=1}^{N'} \sum_{l_2=1}^{N'} i_i(l_1, l_2) \right] \quad (4.3.2)$$

where,  $M$ : Total number of patches in the whole image.

$N'$ : Size of the patch

$i_i(\cdot, \cdot)$ : Intensity function of the  $i$ -th patch.

Therefore, the value of  $\epsilon$  can be estimated from the whole image, before the actual procedure on each patch. Thus, we assume  $\epsilon$  to be given, just as the illumination directions  $\sigma_L, \tau_L$ .

The DFT of (4.3.1) will be

$$I(k_1, k_2) = X(k_1, k_2) + Y(k_1, k_2) \quad (4.3.3) \\ = N^2 \epsilon [\sin\sigma \cos\tau \cos\tau_L \sin\sigma_L + \sin\sigma \sin\tau \sin\tau_L \sin\sigma_L + \cos\sigma \cos\sigma_L] \delta(k_1, k_2)$$

$$+ (1-2\cos\omega_1 e^{-j2\pi\frac{n_1}{N}} + e^{-j4\pi\frac{n_1}{N}})^{-\frac{c}{2}} (1-2\cos\omega_2 e^{-j2\pi\frac{n_2}{N}} + e^{-j4\pi\frac{n_2}{N}})^{-\frac{d}{2}} W(k_1, k_2) \quad (4.3.4)$$

where  $n_1, n_2$  are same as defined by (4.2.3.2.10a), (4.2.3.2.10b), and

$$\delta(k_1, k_2) = \begin{cases} 1 & , \text{if } k_1, k_2 = 0 \\ 0 & , \text{otherwise} \end{cases} \quad (4.3.5)$$

#### 4.3.1 Estimation Of The Parameters $c, d, \omega_1, \omega_2, \sigma, \tau$

The estimation of parameters in this projected Fractional Differencing Periodic model (4.3.4) can be done in the frequency domain, modifying the techniques suggested in [127]. This frequency domain analysis has an advantage over the spatial domain analysis. Since we need only to take the inverse Fourier transform to get the whole image at the end of procedures, we can avoid the integrability problem which might occur in spatial domain analysis when the estimated surface orientation from each local shape has an error.

For estimation, all parameters can be estimated directly from the given data  $I(k_1, k_2)$ , if we can obtain the likelihood function of  $|Y(k_1, k_2)|$ , from the relationship

$$Y(k_1, k_2) = I(k_1, k_2) - X(k_1, k_2). \quad (4.3.1.1)$$

Then, since the noise sequence  $\zeta'(m_1, m_2)$  is assumed to be white Gaussian,  $W(k_1, k_2)$  and  $Y(k_1, k_2)$  follow the Rayleigh distribution as in the following theorem.

**Theorem 4.3.1:** The modulus of the DFT of the noise sequence,  $\{|W(k_1, k_2)|, k_1=0, 1, \dots, N-1, k_2=0, 1, \dots, \lfloor N/2 \rfloor\}$  and  $\{|Y(k_1, k_2)|, k_1=0, 1, \dots, N-1, k_2=0, 1, \dots, \lfloor N/2 \rfloor\}$  are the white sequences with the following Rayleigh densities.

$$f_{|W(k_1, k_2)|}(W) = \begin{cases} \frac{2W}{\rho N^2} \exp\left\{-\frac{W^2}{\rho N^2}\right\} & , W \geq 0 \\ 0 & , \text{otherwise} \end{cases}$$

$$f_{|Y(k_1, k_2)|}(Y) = \begin{cases} \frac{2s_{k_1, k_2}^2 Y^2(k_1, k_2)}{\rho N^2} \exp\left\{-\frac{s_{k_1, k_2}^2 Y^2(k_1, k_2)}{\rho N^2}\right\} & , Y(k_1, k_2) \geq 0 \\ 0 & , \text{otherwise} \end{cases}$$

where

$$s_{k_1, k_2} = \left| 2\cos\left(\frac{2\pi n_1}{N}\right) - 2\cos\omega_1 \right|^{\frac{c}{2}} \left| 2\cos\left(\frac{2\pi n_2}{N}\right) - 2\cos\omega_2 \right|^{\frac{d}{2}}$$

(Proof) Let  $W'(k_1, k_2)$  be the DFT of a white noise sequence  $\zeta'(m_1, m_2)$  with a normal distribution, that is,

$$\zeta'(m_1, m_2) \sim N(0, \rho) \quad , \text{for } m_1, m_2 = 1, 2, \dots, N \quad (4.3.1.2)$$

Then,  $W'(k_1, k_2)$  will follow another normal distribution as follows [26].

$$W'(k_1, k_2) \sim N(N \cdot E[\zeta'(m_1, m_2)], \rho N^2) \quad (4.3.1.3.a)$$

$$\sim N(0, \rho N^2) \quad (4.3.1.3.b)$$

and

$$\text{Re}(W'(k_1, k_2)), \text{Im}(W'(k_1, k_2)) \sim N(0, \frac{\rho N^2}{2}) \quad (4.3.1.4)$$

where  $\text{Re}(W')$  and  $\text{Im}(W')$  are the real and the imaginary parts of  $W'(k_1, k_2)$ , respectively.

Define new coordinate systems,  $(l_1, l_2)$  and  $(n_1, n_2)$ , which can be obtained from the coordinate transformations (4.2.3.2.5), (4.2.3.2.10). Thus, based on the new coordinate system, a new noise sequence  $\zeta(l_1, l_2)$  which has the corresponding DFT,  $W(k_1, k_2)$ , can be defined. As defined before, since the density function of  $\text{Re}(W'(k_1, k_2))$  or  $\text{Im}(W'(k_1, k_2))$  follows a normal distribution and the coordinate transformations are the linear transformations, the density function of  $\zeta(l_1, l_2), \text{Re}(W(k_1, k_2))$  will follow the same normal distributions to the ones of  $\zeta'(m_1, m_2), \text{Re}(W'(k_1, k_2))$ . That is,

$$\zeta(l_1, l_2) \sim N(0, \rho) \quad , \text{for } l_1, l_2 = 1, 2, \dots, N \quad (4.3.1.5)$$

and

$$\text{Re}(W(n_1, n_2)), \text{Im}(W(n_1, n_2)) \sim N(0, \frac{\rho N^2}{2}) \quad (4.3.1.6)$$

Now, consider the density function of  $|W(n_1, n_2)|$ . Since  $W(n_1, n_2)$  is a complex, defining  $W$  be  $W(n_1, n_2)$ ,

$$|W(n_1, n_2)| = \sqrt{\text{Re}^2(W) + \text{Im}^2(W)} \quad (4.3.1.7)$$

Define  $\phi = \tan^{-1}(\frac{\text{Im}(W)}{\text{Re}(W)})$ . Then, we can have the following relations.

$$\text{Re}(W) = |W(n_1, n_2)| \cos \phi \quad (4.3.1.8.a)$$

$$\text{Im}(W) = |W(n_1, n_2)| \sin \phi \quad , \text{for } |W| > 0 \quad (4.3.1.8.b)$$

Thus, the joint probability density of  $|W'|$  and  $\phi$  can be obtained from the Jacobian

and the joint probability density of  $\text{Re}(W')$  and  $\text{Im}(W')$  as follows.

$$f_{|W| \phi}(|W|, \phi) = \frac{1}{\text{Jacobian}} f_{\text{Re}(W) \text{Im}(W)}(\text{Re}(W), \text{Im}(W)) \quad , \text{for } |W| > 0 \quad (4.3.1.9.a)$$

$$= |W| f_{\text{Re}(W)}(|W| \cos \phi) f_{\text{Im}(W)}(|W| \sin \phi) \quad (4.3.1.9.b)$$

$$= \frac{|W|}{\pi \rho N^2} e^{\frac{-(\text{Re}^2(W) + \text{Im}^2(W))}{\rho N^2}} \quad (4.3.1.9.c)$$

$$\text{where Jacobian} = \begin{vmatrix} \frac{\partial |W|}{\partial \text{Re}(W)} & \frac{\partial |W|}{\partial \text{Im}(W)} \\ \frac{\partial \phi}{\partial \text{Re}(W)} & \frac{\partial \phi}{\partial \text{Im}(W)} \end{vmatrix} \quad (4.3.1.10.a)$$

$$= \frac{1}{|W|} \quad (4.3.1.10.b)$$

Therefore, since  $|W|$  and  $\phi$  are independent, and the density function of  $\phi$ ,  $f_\phi(\phi)$ , is

$$\frac{1}{2\pi},$$

$$f_{|W| \phi}(|W|, \phi) = f_{|W|}(|W|) \cdot f_\phi(\phi) \quad (4.3.1.11)$$

and

$$f_{|W|}(W) = \begin{cases} \frac{2W}{\rho N^2} \exp\left(\frac{-W^2}{\rho N^2}\right) & , W \geq 0 \\ 0 & , \text{otherwise} \end{cases} \quad (4.3.1.12)$$

Now, set

$$s_{k_1, k_2} = \left| 2\cos\left(\frac{2\pi n_1}{N}\right) - 2\cos\omega_1 \right|^{\frac{c}{2}} \left| 2\cos\left(\frac{2\pi n_2}{N}\right) - 2\cos\omega_2 \right|^{\frac{d}{2}} \quad (4.3.1.13)$$

Then, from the definition of  $n_i$ , (2.3.2.10), we can have

$$|Y(k_1, k_2)| = s_{k_1, k_2}^{-1} |W(k_1, k_2)| \quad (4.3.1.14)$$

$$= s_{k_1, k_2}^{-1} |W'(n_1, n_2)| \quad (4.3.1.15)$$

Thus, the density function of  $|Y(k_1, k_2)|$  can be represented by following equations.

$$f_{|Y(k_1, k_2)|}(Y) = s_{k_1, k_2} f_{|W(k_1, k_2)|}(s_{k_1, k_2} Y(k_1, k_2)) \quad (4.3.1.16)$$

$$= \begin{cases} \frac{2s_{k_1, k_2}^2 Y(k_1, k_2)}{\rho N^2} \exp \left\{ \frac{-s_{k_1, k_2}^2 Y^2(k_1, k_2)}{\rho N^2} \right\} & , Y(k_1, k_2) \geq 0 \\ 0 & , \text{otherwise} \end{cases}$$

■

From these probabilistic properties, the estimation of parameters can be done by a hybrid method of Least Square and Maximum Likelihood estimations, which was suggested by Eom [67]. For LS estimation, if the values of the illumination direction  $\sigma_L$ ,  $\tau_L$  and the normalization factor  $\epsilon$  are given, and parameters  $\omega_1$ ,  $\omega_2$ ,  $\sigma$ ,  $\tau$  are set, then  $\theta = (c, d, \alpha)^T$  can be estimated by minimizing the following cost function.

$$\begin{aligned} J(\theta, \omega_1, \omega_2) = & \sum_{k_1=0}^{N-1} \sum_{k_2=0}^{\lfloor N/2 \rfloor} (\log |I(k_1, k_2) - N^2 \epsilon [\sin \sigma \cos \tau \cos \tau_L \sin \sigma_L \\ & + \sin \sigma \sin \tau \sin \tau_L \sin \sigma_L + \cos \sigma \cos \sigma_L] \delta(k_1, k_2)| \\ & + \frac{c}{2} \log |2 \cos \frac{2\pi[(\sin^2 \tau + \cos \sigma \cos^2 \tau)k_1 + (\cos \sigma - 1) \sin \tau \cos \tau k_2]}{N \cos \sigma} - 2 \cos \omega_1| \end{aligned}$$

$$+ \frac{d}{2} \log \left| 2 \cos \frac{2\pi[(\cos\sigma-1)\sin\tau\cos\tau k_1 + (\cos^2\tau + \cos\sigma\sin^2\tau)k_2]}{N\cos\sigma} - 2\cos\omega_2 \right| + \alpha)^2 \quad (4.3.1.17)$$

$$= \sum_{k_1=0}^{N-1} \sum_{k_2=0}^{\lfloor N/2 \rfloor} (\log |I(k_1, k_2)| - N^2 \epsilon [\sin\sigma \cos\tau \cos\tau_L \sin\sigma_L + \sin\sigma \sin\tau \sin\tau_L \sin\sigma_L + \cos\sigma \cos\sigma_L] \delta(k_1, k_2)) - \theta^T Q(k_1, k_2))^2 \quad (4.3.1.18)$$

where  $\alpha = -E[\log |W(k_1, k_2)|]$ ,  $\theta = (c, d, \alpha)^T$ .

Here,

$$Q(k_1, k_2) = \begin{bmatrix} -\frac{1}{2} \log \left| 2 \cos \frac{2\pi[(\sin^2\tau + \cos\sigma \cos^2\tau)k_1 + (\cos\sigma - 1)\sin\tau \cos\tau k_2]}{N\cos\sigma} - 2\cos\omega_1 \right| \\ -\frac{1}{2} \log \left| 2 \cos \frac{2\pi[(\cos\sigma - 1)\sin\tau \cos\tau k_1 + (\cos^2\tau + \cos\sigma \sin^2\tau)k_2]}{N\cos\sigma} - 2\cos\omega_2 \right| \\ -1 \end{bmatrix} \quad (4.3.1.19)$$

Thus, the estimated values will be

$$[\hat{c}, \hat{d}, \hat{\alpha}]^T = \left( \sum_{k_1=0}^{N-1} \sum_{k_2=0}^{\lfloor N/2 \rfloor} Q(k_1, k_2) Q^T(k_1, k_2) \right)^{-1} \left( \sum_{k_1=0}^{N-1} \sum_{k_2=0}^{\lfloor N/2 \rfloor} Q(k_1, k_2) \log |Z(k_1, k_2)| - N^2 \epsilon [\sin\sigma \cos\tau \cos\tau_L \sin\sigma_L + \sin\sigma \sin\tau \sin\tau_L \sin\sigma_L + \cos\sigma \cos\sigma_L] \delta(k_1, k_2) \right) \quad (4.3.1.20)$$

Also, ML estimators of  $\omega_1$ ,  $\omega_2$ ,  $\sigma$ ,  $\tau$  can be calculated by maximizing the log-likelihood function  $L(Y; \theta, \omega_1, \omega_2)$  with  $\hat{\alpha}$  estimated from above.

$$\begin{aligned}
L(Y; \theta, \omega_1, \omega_2) = & \sum_{k_1=0}^{N-1} \sum_{k_2=0}^{\lfloor N/2 \rfloor} \log |I(k_1, k_2) - N^2 \epsilon [\sin \sigma \cos \tau \cos \tau_L \sin \sigma_L \\
& + \sin \sigma \sin \tau \sin \tau_L \sin \sigma_L + \cos \sigma \cos \sigma_L] \delta(k_1, k_2)| - \sum_{k_1=0}^{N-1} \sum_{k_2=0}^{\lfloor N/2 \rfloor} \log \left( \frac{\rho N^2}{2} \right) \\
& + \frac{c}{2} N \sum_{k_1=0}^{N-1} \log \left| 2 \left( \cos \frac{2\pi[(\sin^2 \tau + \cos \sigma \cos^2 \tau)k_1 + (\cos \sigma - 1) \sin \tau \cos \tau k_2]}{N \cos \sigma} - \cos \omega_1 \right) \right| \\
& + d N \sum_{k_2=0}^{\lfloor N/2 \rfloor} \log \left| 2 \left( \cos \frac{2\pi[(\cos \sigma - 1) \sin \tau \cos \tau k_1 + (\cos^2 \tau + \cos \sigma \sin^2 \tau)k_2]}{N \cos \sigma} - \cos \omega_2 \right) \right| \\
& - \frac{1}{\rho N^2} \sum_{k_1=0}^{N-1} \sum_{k_2=0}^{\lfloor N/2 \rfloor} \left| 2 \left( \cos \frac{2\pi[(\sin^2 \tau + \cos \sigma \cos^2 \tau)k_1 + (\cos \sigma - 1) \sin \tau \cos \tau k_2]}{N \cos \sigma} - \cos \omega_1 \right) \right|^c \\
& \cdot \left| 2 \left( \cos \frac{2\pi[(\cos \sigma - 1) \sin \tau \cos \tau k_1 + (\cos^2 \tau + \cos \sigma \sin^2 \tau)k_2]}{N \cos \sigma} - \cos \omega_2 \right) \right|^d \\
& \cdot |I(k_1, k_2) - N^2 \epsilon [\sin \sigma \cos \tau \cos \tau_L \sin \sigma_L + \sin \sigma \sin \tau \sin \tau_L \sin \sigma_L + \cos \sigma \cos \sigma_L] \delta(k_1, k_2)|^2
\end{aligned} \tag{4.3.1.21}$$

where  $\rho$  is a variance of  $\zeta(l_1, l_2)$  and can be estimated by the following equation in the mean square sense.

$$\hat{\rho} = \frac{1}{N^2} \exp \left\{ \gamma - 2\hat{\alpha} - \frac{\pi^2}{6N^2} \right\} \tag{4.3.1.22}$$

where  $\gamma$  is Euler's constant ( $= 0.5772157$ ) [67].

Therefore, the estimation scheme can be summarized as follows:

(Estimation Algorithm)

- Step 1: Estimate the illumination direction  $\sigma_L$ ,  $\tau_L$  and the normalization factor  $\epsilon$  from the whole image, by (Theorem 4.2.1) and (4.3.17), respectively.
- Step 2: For each patch, choose resonant frequencies  $\omega_1$ ,  $\omega_2$  in the range of  $[0, \frac{\pi}{2}]$ , and the surface orientation parameters  $\sigma$ ,  $\tau$  in the range of  $[-\frac{\pi}{2}, \frac{\pi}{2}]$ .
- Step 3: With the given values of  $\omega_1$ ,  $\omega_2$ ,  $\sigma$  and  $\tau$ , estimate  $c$ ,  $d$ , and  $\alpha$  by LS estimation algorithm (4.3.1.20).
- Step 4: Using  $\hat{\alpha}$ , compute the estimate of the variance of  $\rho$ ,  $\zeta(l_1, l_2)$ , by equation (4.3.1.22).
- Step 5: Using the estimates  $\hat{c}$ ,  $\hat{d}$  and  $\hat{\rho}$  found in Step 3 and 4, maximize the likelihood function given by (4.3.1.21) with respect to  $\omega_1$ ,  $\omega_2$ ,  $\sigma$ , and  $\tau$ .
- Step 6: Using the estimates  $\hat{\omega}_1$ ,  $\hat{\omega}_2$ ,  $\hat{\sigma}$  and  $\hat{\tau}$ , repeat Step 3 to Step 5 until the estimates have no significant change in successive iterations.

The results from computer simulation will be discussed in the next section.

## 4.3.2 Experimental Results

### 4.3.2.1. 3-D Texture On A Sphere Surface

In this experiment, a whole image which contains the shade and texture on a 3-D sphere surface was constructed using our proposed 3-D texture model, and this was compared with the images which were obtained by either applying the reflectance map function or by projecting the texture pattern only. Since our model is a composite of

the Shape-from-shading and the Shape-from-texture models, the constructed image will look more natural than the ones from either the Shape-from-shading or the Shape-from-texture technique. For this experiment, the texture pattern was chosen as the Fractional Differencing Periodic model (4.2.3.2.6) with the parameter values,  $\omega_1 = 0.2$ ,  $\omega_2 = 0.2$ ,  $c = 0.8$ , and  $d = 0.8$ . From the given illumination direction  $\sigma_L, \tau_L$ , and the surface orientations of sphere,  $\sigma, \tau$ , the 3-D surface of a sphere covered by the chosen texture pattern was synthesized. Here, the illumination direction was chosen as  $\sigma_L = -0.66$ ,  $\tau_L = -0.66$ , and the surface orientations  $\sigma(i_1, i_2), \tau(i_1, i_2)$  of the  $(i_1, i_2)$ th patch was given by

$$\sigma(i_1, i_2) = \begin{cases} \tan^{-1} \left( \frac{\partial H(l_1, l_2) / \partial l_2}{\partial H(l_1, l_2) / \partial l_1} \right) |_{i_1, i_2} & , \text{if } H(l_1, l_2) \geq 63 \\ 0 & , \text{otherwise} \end{cases} \quad (4.3.2.1)$$

and

$$\tau(i_1, i_2) = \begin{cases} \cos^{-1} \frac{1}{\sqrt{(\partial H / \partial l_1)^2 |_{i_1, i_2} + (\partial H / \partial l_2)^2 |_{i_1, i_2} + 1}} & , \text{if } H(l_1, l_2) \geq 63 \\ 0 & , \text{otherwise} \end{cases} \quad (4.3.2.2)$$

where the height function  $H(l_1, l_2)$  is given by

$$H(l_1, l_2) = 15^2 - l_1^2 - l_2^2 \quad (4.3.2.3)$$

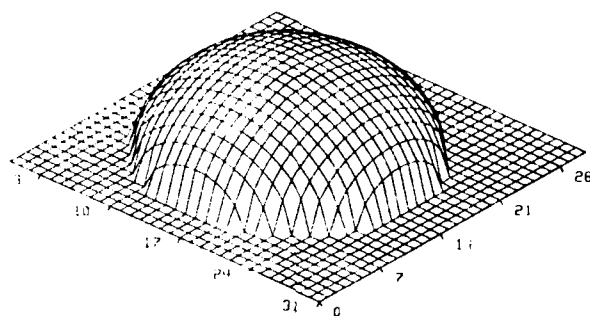
In this experiment, each 3-D texture pattern was synthesized on  $32 \times 32$  pixel sized planar patch, and  $16 \times 16$  pixel sized patch was taken from the center. The complete image of sphere ( $512 \times 512$ ) was obtained by adjoining these  $16 \times 16$  pixel sized patches. Figure 4.3-a,b show the 3-D shape of a hemisphere and the corresponding sphere image obtained by the reflectance map function (4.2.2.3) with the parameter values  $\sigma_L = -0.66$ ,  $\tau_L = -0.66$ ,  $\epsilon = 100$  (4.3.2), and Figure 4.4 shows the orthographically projected texture image based on the given sphere surface with

equation (4.2.3.2.6). Finally, with the composite model of the projected texture image and the reflectance map function (4.3.1), an image of 3-D texture on the surface of a sphere was synthesized (Figure 4.5).

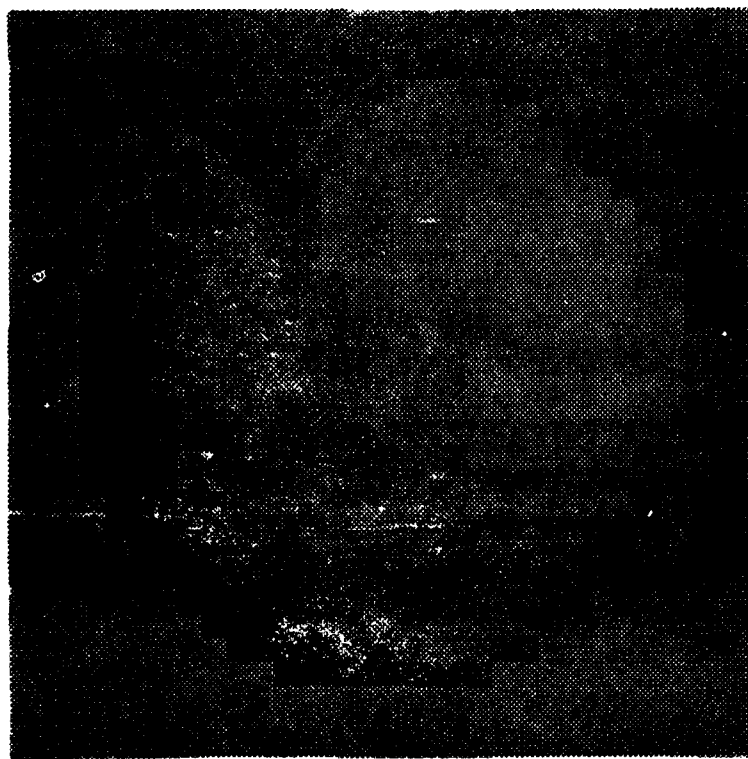
Here, Figure 4.3 and Figure 4.4 illustrate that neither the Shape-from-shading nor the Shape-from-texture technique is suitable for representing the natural scene. Figure 4.3 does not contain any detail information about the surface pattern, while Figure 4.4 does not contain any shade. Thus it is difficult to see the sphere in either Figure 4.3 or Figure 4.4. Figure 4.5, however, illustrates the sphere image with texture pattern on its surface clearly, thus shows our model's capability to represent the 3-D textural surface.

#### 4.3.2.2. Parameter Estimation

From this experiment, we want to show how accurate the estimated results are. Since each small patch is assumed to be a tilted and slanted texture plane and the whole image is obtained by adjoining these patches, our proposed 3-D texture model will fit each small image patch and the surface orientation parameter will be estimated based on each patch. Thus, in this experiment, we will consider single patches of texture patterns which represent the tilted and slanted texture planes. From these patches the parameter values of the model (4.3.1) will be estimated by the proposed estimation scheme, and compared with the true values. For this experiment, three different 2-D texture patterns sized  $64 \times 64$  were generated by equation (4.3.1) with the different values of parameters  $\omega_1$ ,  $\omega_2$ ,  $c$ , and  $d$ . Then, the projected images of the slanted and tilted texture planes were synthesized with the different values of the surface orientation  $\sigma$ ,  $\tau$  in equation (4.3.4), and zero mean white Gaussian noise with variance 10 was added to each image. The values of the illumination direction  $\sigma_L$ ,  $\tau_L$



(a)



(b)

Figure 4.3: Sphere images: (a) Height function of a sphere obtained by equation (4.3.2.3) (b) Image obtained by the reflectance map function (4.2.2.3) with  $\epsilon=100$  (4.3.2),  $\sigma_L = -0.66$ ,  $\tau_L = -0.66$

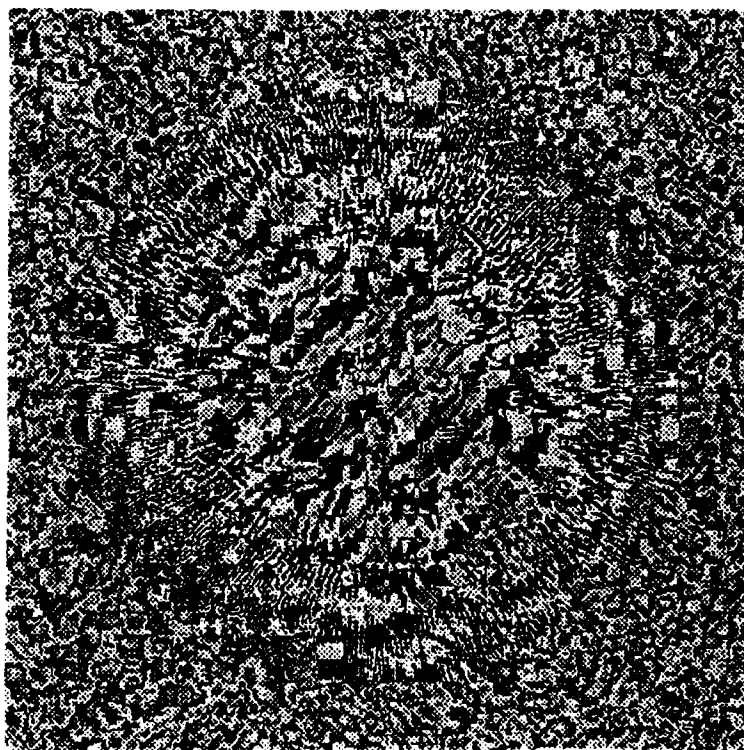


Figure 4.4: Image obtained after projecting texture image orthographically to the sphere surface. (Background texture pattern is generated by Fractional Differencing Periodic model (2.3.2.6) with  $\omega_1=0.2$ ,  $\omega_2=0.2$ ,  $c=0.8$ ,  $d=0.8$ )

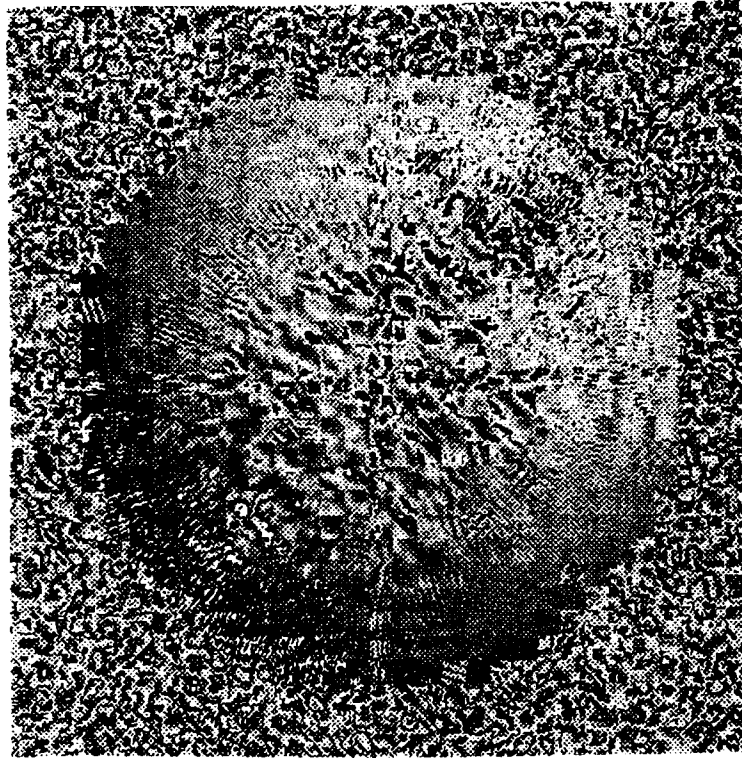
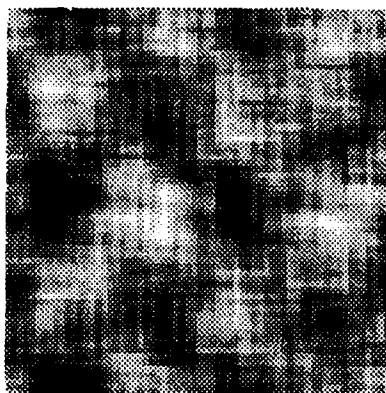


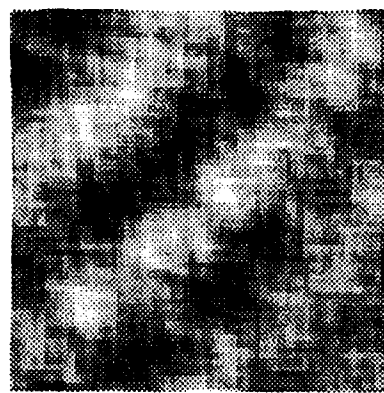
Figure 4.5: Image of 3-D texture on the surface of a sphere (Image is generated by the composite model (4.3.1) with  $\sigma_L = -0.66$ ,  $\tau_L = -0.66$ )

and the normalization factor  $\epsilon$  was given by  $\frac{\pi}{8}$ ,  $\frac{\pi}{4}$ , and 100, respectively. Thus, since the intensity value of a plane surface will be constant all over the patch, the deterministic part of equation (4.3.4) was considered as a constant, and added to the random field part. For the estimation, the hybrid method of Least Square and Maximum Likelihood estimation, which was discussed in previous section, was used to estimate parameters.

Figure 4.6-a shows one of the 2-D texture pattern which was generated by equations (4.2.3.2.6)-(4.2.3.2.12) with the values of  $\omega_1$ ,  $\omega_2$ ,  $c$ ,  $d$  as 0.2, 0.2, 0.8, 0.8, respectively, and Figure 4.6-b shows the projected image of the version of Figure 4.6-a tilted and slanted by  $-\frac{\pi}{4}$  and  $\frac{\pi}{8}$ , respectively. As can be seen from Figure 4.6-a and Figure 4.6-b, due to the slanting, the distance between the dark spots along the normal direction of the tilted axis (the tilted axis is the North-west to South-east diagonal) reduces considerably (thus producing almost a continuous dark band along that direction in Figure 4.6-b). Here, the 2-D texture model does not fit the pattern in Figure 4.6-b, since this pattern has a non-isotropic random texture distribution due to the tilt and slant. Note that this synthesis technique does not require an interpolation after projecting. Because the white Gaussian random noise will still be white Gaussian noise after projecting, the random noise as input data can be generated for the projected model directly. From these three different 3-D texture patches, we have estimates close to the true values. [Table 4.1] Also shown in the parentheses are absolute deviations from the true values. Therefore, we can say that the height function and the texture pattern of whole image can be estimated properly from this local patch estimation process.



(a)



(b)

Figure 4.6: 2-D texture images: (a) Image obtained from (4.2.3.2.6) with  $\omega_1=0.2$ ,  $\omega_2=0.2$ ,  $c=0.8$ ,  $d=0.8$  (b) Projected image of the tilted and slanted version of Figure 4.6-a by  $-\pi/4$  and  $\pi/8$ , respectively

Table 4.1: True parameter values and the estimated parameter values of the projected Fractional Differencing Periodic model (4.2.3.2.6): The random noise sequence as input data for each synthesized texture patch of size  $64 \times 64$  was generated from white Gaussian noise with zero mean and variance 10. Estimated values were obtained from these synthesized images by equations (4.3.1.8)-(4.3.1.13).

Patches	True Values					
	$\omega_1$	$\omega_2$	c	d	$\sigma$	$\tau$
Patch 1	0.2	0.2	0.8	0.8	0.4	0.78
Patch 2	0.2	0.2	0.4	0.8	0.78	0.78
Patch 3	0.2	0.4	0.6	0.8	0.2	0.6

Patches	Estimated Values					
	$\hat{\omega}_1$	$\hat{\omega}_2$	$\hat{c}$	$\hat{d}$	$\hat{\sigma}$	$\hat{\tau}$
Patch 1	0.204 (0.004)	0.208 (0.008)	0.803 (0.003)	0.807 (0.007)	0.393 (0.007)	0.744 (0.036)
Patch 2	0.219 (0.019)	0.232 (0.032)	0.357 (0.043)	0.716 (0.084)	0.812 (0.032)	0.673 (0.107)
Patch 3	0.191 (0.009)	0.378 (0.022)	0.620 (0.020)	0.589 (0.211)	0.299 (0.099)	0.598 (0.002)

#### 4.3.2.3. Tree Image

A 512×512 real image of a part of a tree, which contains shade and texture on surface was considered (Figure 4.7-a). From the whole image, the estimation values of the illumination direction  $\sigma_L$ ,  $\tau_L$  were determined to be  $\hat{\sigma}_L = -1.3384$ ,  $\hat{\tau}_L = -0.0426$ , by applying Lee's method. Then, for this experiment, several local patches of size 32×32 were taken from the tree surface, and the parameter values were estimated by applying our projected Fractional Differencing Periodic model (4.3.1) and estimation scheme (4.3.1.7)-(4.3.1.13). Average estimated values of the parameters were obtained as  $\omega_1 = 0.486$ ,  $\omega_2 = 0.053$ ,  $c = 1.394$ ,  $d = 0.762$ . A Synthesized tree surface image with the given illumination direction was constructed by projecting this texture pattern on a cylinder surface (Figure 4.7-b). This image looks very similar to the original tree image, and shows the ability of our model to represent a non-stationary texture pattern such as a tree bark on tree surface.

#### 4.4. Conclusions

In this chapter, a composite model of Shape-from-shading and Shape-from-texture based on a 2-D orthographically projected Fractional Differencing Periodic model was developed to represent a 3-D surface image which contains information about both radiance and texture. This composite model has several advantages over the conventional approaches. First, as compared to the Shape-from-shading techniques, this model always gives unique and more accurate solutions for the surface orientation parameter values, because of the additional constraint from the texture function part. Also, by using this analysis, the integrability problem which might occur in spatial domain analysis can be avoided, because only one inverse

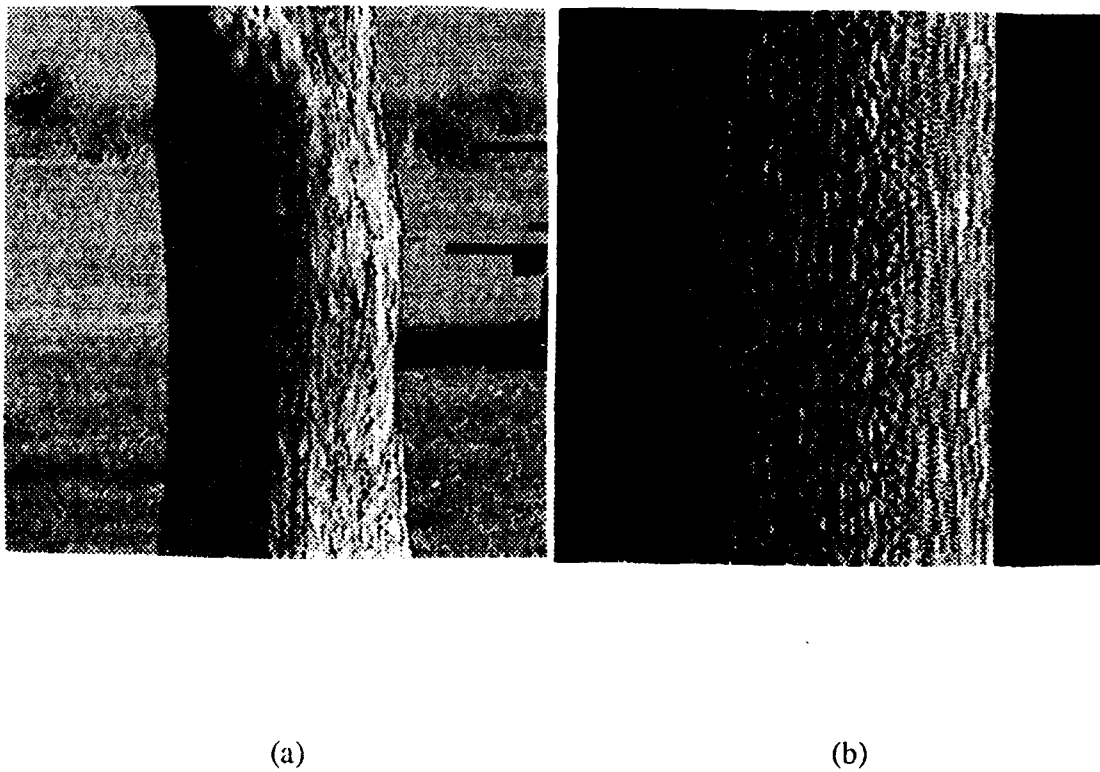


Figure 4.7: Tree images: (a) A 512×512 original image of a part of a tree. (b) A synthesized tree image: Local patch size is 32×32, and each 3-D texture pattern was synthesized by the composite model (4.3.1) with the illumination direction  $\sigma_L = -1.3384$ ,  $\tau_L = -0.0426$  and  $\omega_1 = 0.486$ ,  $\omega_2 = 0.053$ ,  $c = 1.394$ ,  $d = 0.762$  for the random part. 16×16 pixel sized patch was taken from the center of it. The complete image of cylinder (512×512) was obtained by adjoining these 16×16 pixel sized patches.

Fourier transform needs to be taken at the end of procedure to get the whole image. Second, as compared to the Shape-from-texture techniques, the Fractional Differencing model has the property of being flexible enough to explain both the long-term and the short-term correlation structure of the texture pattern, thus, it has a superior ability to model different textures encountered in practice. The orthographical projection adds the additional flexibility to represent the 3-D rotated texture due to the slant and the tilt of a surface normal plane. The estimation scheme for the parameters was based on the hybrid method of least square and maximum likelihood estimations.

## **CHAPTER 5**

### **CLASSIFICATION OF 3-D ROTATED TEXTURES**

#### **5.1. Introduction**

Texture classification has been the focus of interest to many researchers [53,92,126,216]. The classification problem can be stated as allocation of an observed texture image data to the one of the pre-defined texture classes. These texture classes can be described by texture features, and then texture features can be the parameters in stochastic [53,92,126] or structural models [216]. Thus, the key step in classification process is the choice of a set of features which can reduce the dimension of the image data to a computationally reasonable amount of data. Preferable features should be those that are simple and easy to extract from the given data while preserving the classifying information present in it.

Most of classification schemes which have been suggested up to date are under the assumption that the test sample data possesses the same surface orientation as the training sample data. Thus, if the orientation of test image is different from the training sample data, for example, in case of a rotated image, the classification performs poorly. This reduces the flexibility of those classification schemes. However, most of natural texture images which we encounter in practice represent the texture of 3-D surfaces. Thus, the observed image is a projected surface image onto

the 2-D image plane with a 2-D rotated, or 3-D slanted and tilted texture pattern. Therefore, it is desirable that the classification scheme have the flexibility to classify even rotated or scaled texture to the original class of it. This is a good indication why it is so important to have the rotational and scaling invariant features in our model. Up to date, several approaches have been reported for the rotational invariant classification scheme [53, 126]. However, those approaches have their own limitations of classification. Khotanzad's method [126] is based on the four different discrete directions instead of an arbitrary angle of the rotational direction, thus, with this classification scheme, the rotated texture pattern with an arbitrary angle can not be classified. Cohen's model [53] uses a coordinate transformation for the rotation and the slant of texture surface, and a ML estimation method is adapted to extract the texture pattern parameters in an AR model and the surface orientation parameters simultaneously. However, because of the complexity of the estimation scheme and the limitation of AR model to represent the surface, this approach may not be practical. In this chapter, a multi-level classification method which can handle arbitrary 3-D rotated samples of textures is developed based on fractional differencing models with a fractal scaling parameter. Since the fractal scale is known to be a rotational and scaling invariant parameter, the accuracy of classification will not be affected by 3-D rotation of the test texture, by using these models. In first level of classification, the textures are classified by the first-order Fractional Differencing model with a fractal scale parameter, and in second level, classification is completed with the additional frequency parameters of the second-order Fractional Differencing periodic model. This multi-level classification scheme has at least following advantages over the conventional approaches [46, 53, 126]. First, since the fractal scale parameter of the first-order Fractional Differencing model can be estimated by a simple Least-square estimation method, the processing time can be dramatically reduced. Second, the

ambiguity, which may be caused by using only one classification parameter, particularly when the values of parameter are close enough for the different textures, can be removed by considering the additional parameters in second-order model. Even though the estimation scheme for these additional parameters is based on ML estimation, the classification process is much simpler compared with other approaches based on ML estimation, e.g. Cohen's [53], because only a small number of texture patterns in same sub-class, which is already classified based on the fractal scale value in first level, need to be classified.

The organization of this chapter is as follows. In section 5.2, the 3-D rotated texture is defined by the linear coordinate transformations. Section 5.3 introduces the Fractional Differencing model with a fractal scaling parameter to represent the rotated and slanted texture surface, and section 5.4 discussed its parameter estimation scheme based on LS and ML estimation methods. In section 5.5, a multi-level 3-D rotational invariant classification scheme is introduced. Section 5.6 then discusses some simulation results carried out to demonstrate the performance of the proposed algorithms, followed by section 5.7 which concludes this chapter.

## **5.2. 3-D Rotated Texture**

To represent a 3-D rotated texture, we need two different sets of coordinate transformations. First one is the 2-D rotational coordinate transformation and second one is the orthographical projection coordinate transformation. The 2-D rotational coordinate transformation is needed to represent a texture image rotated on the 2-D image plane, and the orthographical coordinate transformation is needed to represent an orthographically projected texture surface onto the image plane due to the slant and tilt of texture surface. Here, notice that for the image whose texture pattern is

distributed isotropically over the surface without any directional trend, the 2-D rotational coordinate transformation is not required, because the 2-D rotation will not affect the pattern of the texture.

The coordinate system  $(l'_1, l'_2)$  which is rotated on the image plane through an angle  $\theta$  clockwise can be obtained from the original coordinate system  $(l_1, l_2)$  by the following simple coordinate transformation.

$$\begin{bmatrix} l'_1 \\ l'_2 \end{bmatrix} = \begin{bmatrix} \cos\theta & -\sin\theta \\ \sin\theta & \cos\theta \end{bmatrix} \begin{bmatrix} l_1 \\ l_2 \end{bmatrix} . \quad (5.2.1)$$

And a texture surface plane slanted and tilted by  $\sigma$  and  $\tau$  can be represented by the orthographical projection. First, take the  $m_1$ - $m_2$  coordinate system over the surface plane. Put a line passing through the origin, and let  $\tau$  be the angle made from the  $m_1$ -axis. Rotate the plane around the line by angle  $\sigma$  and project the rotated plane orthographically onto the image plane. Thus, a new coordinate system from the viewing direction,  $l_1$ - $l_2$ , can be obtained from the following two coordinate transformations.

$$\begin{bmatrix} ll_1 \\ ll_2 \end{bmatrix} = \begin{bmatrix} \cos\tau & -\sin\tau \\ \sin\tau & \cos\tau \end{bmatrix} \begin{bmatrix} m_1 \\ m_2 \end{bmatrix} , \quad (5.2.2)$$

and

$$\begin{bmatrix} l_1 \\ l_2 \end{bmatrix} = \begin{bmatrix} 1 & 0 \\ 0 & \cos\sigma \end{bmatrix} \begin{bmatrix} ll_1 \\ ll_2 \end{bmatrix} . \quad (5.2.3)$$

Hence, as is well known [110], the coordinate transformation of the orthographic projection between the  $m_1$ - $m_2$  system and  $l_1$ - $l_2$  system can be given as follows.

$$\begin{bmatrix} l_1 \\ l_2 \end{bmatrix} = \begin{bmatrix} \cos\tau & -\sin\tau \\ \sin\tau & \cos\tau \end{bmatrix} \begin{bmatrix} 1 & 0 \\ 0 & \cos\sigma \end{bmatrix} \begin{bmatrix} \cos\tau & -\sin\tau \\ \sin\tau & \cos\tau \end{bmatrix}^{-1} \begin{bmatrix} m_1 \\ m_2 \end{bmatrix} \quad (5.2.4a)$$

$$= \begin{bmatrix} \cos^2\tau + \cos\sigma\sin^2\tau & (1-\cos\sigma)\sin\tau\cos\tau \\ (1-\cos\sigma)\sin\tau\cos\tau & \sin^2\tau + \cos\sigma\cos^2\tau \end{bmatrix} \begin{bmatrix} m_1 \\ m_2 \end{bmatrix} \quad (5.2.4b)$$

Therefore, a texture plane coordinate system ( $l''_1, l''_2$ ) obtained after rotating, slanting and tilting with arbitrary angles can be represented by combining both 2-D rotational coordinate transformation (5.2.1) and the orthographical projection coordinate transformation (5.2.4) as follows.

$$\begin{bmatrix} l''_1 \\ l''_2 \end{bmatrix} = \begin{bmatrix} \cos\theta & -\sin\theta \\ \sin\theta & \cos\theta \end{bmatrix} \begin{bmatrix} \cos^2\tau + \cos\sigma\sin^2\tau & (1-\cos\sigma)\sin\tau\cos\tau \\ (1-\cos\sigma)\sin\tau\cos\tau & \sin^2\tau + \cos\sigma\cos^2\tau \end{bmatrix} \begin{bmatrix} m_1 \\ m_2 \end{bmatrix} \quad (5.2.5a)$$

$$= \begin{bmatrix} I & II \\ III & IV \end{bmatrix} \quad (5.2.5b)$$

where

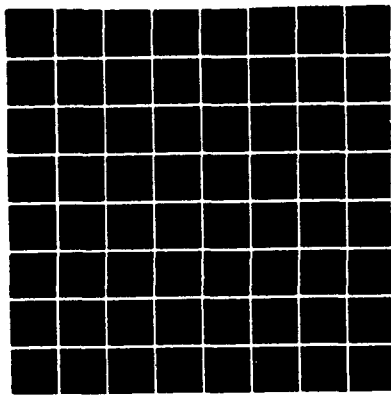
$$I = \cos\theta(\cos^2\tau + \cos\sigma\sin^2\tau) - \sin\theta(1-\cos\sigma)\sin\tau\cos\tau \quad (5.2.6a)$$

$$II = \cos\theta(1-\cos\sigma)\sin\tau\cos\tau - \sin\theta(\sin^2\tau + \cos\sigma\cos^2\tau) \quad (5.2.6b)$$

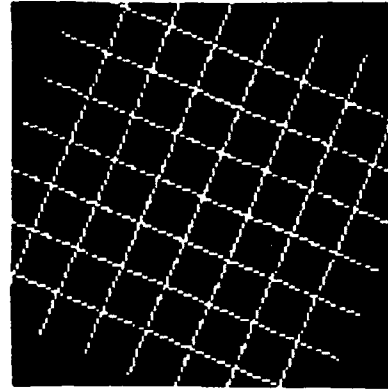
$$III = \sin\theta(\cos^2\tau + \cos\sigma\sin^2\tau) + \cos\theta(1-\cos\sigma)\sin\tau\cos\tau \quad (5.2.6c)$$

$$IV = \sin\theta(1-\cos\sigma)\sin\tau\cos\tau + \cos\theta(\sin^2\tau + \cos\sigma\cos^2\tau) \quad (5.2.6d)$$

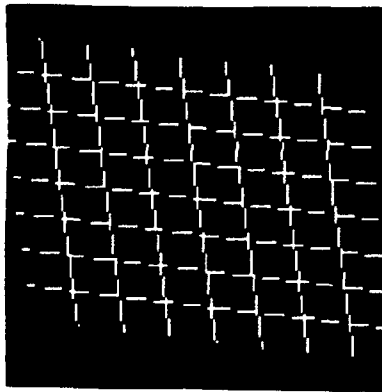
One grid pattern image (Figure 5.1-a) was considered to demonstrate these coordinate transformations. The coordinate transformation was taken to this image with  $\theta = \pi/8$ ,  $\sigma = \pi/4$ , and  $\tau = -\pi/8$ . Figure 5.1-b, Figure 5.1-c, and Figure 5.1-d depict a 2-D rotational coordinate transformation, a orthographical projection coordinate transformation, and both coordinate transformations, respectively.



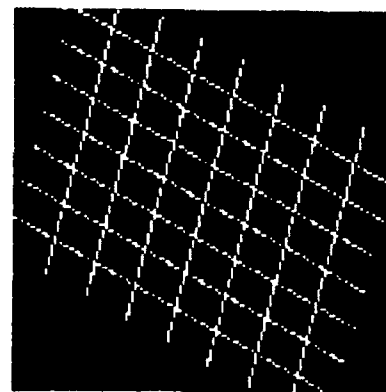
(a)



(b)



(c)



(d)

Figure 5.1: 2-D grid pattern images: (a) Original image, (b) Image obtained after rotating the image(Figure 5.1-a) on the image plane with  $\theta = \pi/8$  in (5.2.1), (c) Image obtained after projecting the image(Figure 5.1-a) orthographically, with  $\sigma = \pi/4$  and  $\tau = -\pi/8$  in (5.2.4), (d) Image obtained after projecting the already rotated image(Figure 5.1-b) orthographically, with  $\sigma = \pi/4$  and  $\tau = -\pi/8$  in (5.2.5).

### 5.3. Fractional Differencing Model With One Fractal Scaling Parameter $c$ .

All features considered in this chapter for the classification purpose can be obtained by fitting a two-dimensional parametric random field models to the given texture. There are various kinds of random field models suggested up to date [4,41,56,85,116], and each random field model has its own advantage and disadvantage based on the purpose of the process. Among the various random field models, the fractional differencing models with one fractal scaling parameter are chosen in this study because of its following properties. First, the fractal scaling parameter  $c$  is known to be a rotational and scaling invariant parameter, thus, with this parameter we have the flexibility to handle the rotated, slanted, and tilted texture surface. Second, unlike the other fractal model based on the fractional Brownian process, this model has a simple estimation scheme, such as least mean square estimation for the parameter  $c$ . Third, with the second order periodic model, this model has good performance in texture synthesis and its ability to simultaneously represent the coarseness and pattern of texture surface with the fractal scaling parameter  $c$  and directional frequency parameters  $\omega_1, \omega_2$ , respectively. Thus, comparing these parameter values, we can classify the texture patterns properly even though some texture patterns shares the same value of one of those parameters. Typical first-order and second-order fractional differencing models with one fractal scaling parameter will be as follows, respectively.

$$y(m_1, m_2) = [(1-z_1^{-1})(1-z_2^{-1})]^{-\frac{c}{2}} \zeta(m_1, m_2) \quad (5.3.1)$$

and

$$y(m_1, m_2) = [(1 - 2\cos\omega_1 z_1^{-1} + z_1^{-2})(1 - 2\cos\omega_2 z_2^{-1} + z_2^{-2})]^{-\frac{c}{2}} \zeta(m_1, m_2) \quad (5.3.2)$$

for  $m_1, m_2 = 0, 1, \dots, N-1$ .

The corresponding DFTs of these functions are

$$Y(k_1, k_2) = [(1 - e^{-j2\pi\frac{k_1}{N}})(1 - e^{-j2\pi\frac{k_2}{N}})]^{-\frac{c}{2}} W(k_1, k_2), \quad (5.3.3)$$

and

$$Y(k_1, k_2) = [(1 - 2\cos\omega_1 e^{-j2\pi\frac{k_1}{N}} + e^{-j4\pi\frac{k_1}{N}}) \cdot (1 - 2\cos\omega_2 e^{-j2\pi\frac{k_2}{N}} + e^{-j4\pi\frac{k_2}{N}})]^{-\frac{c}{2}} W(k_1, k_2), \quad (5.3.4)$$

where  $z_i$  is the delay operator associated with  $m_i$ ,  $\zeta(m_1, m_2)$  is an i.i.d. Gaussian sequence, and  $W(k_1, k_2)$  is the corresponding DFT.

Note that this random function  $y(m_1, m_2)$  is defined on the surface normal plane because this model is based on a 2-D texture model. Thus, it will fit the texture pattern which is isotropically distributed over the plane and this isotropically distributed texture pattern can be obtained by viewing from the surface normal direction. Then, the model for the 3-D rotated texture pattern can be obtained by applying the 2-D rotational and the orthographical projection coordinate transformations.

### 5.3.1. Rotated And Projected Fractional Differencing Model

The random function  $y'(l_1, l_2)$ , defined on the viewing direction image plane, can be obtained by projecting  $y(m_1, m_2)$  onto the image plane orthographically. On

the other hand, the rotated random function  $y''(l_1, l_2)$  can be obtained by rotating the original coordinate axes through the angle  $\theta$ . Thus, if  $l_1$  and  $l_2$  are the axes transformed from  $m_1$  and  $m_2$  based on  $\tau$  and  $\sigma$ , from the coordinate transformation for the orthographical projection (5.2.4), we can have the following first or second-order model.

$$y'(l_1, l_2) = [(1-z_l'^{-1})(1-z_l'^{-1})]^{-\frac{c}{2}} \zeta(l_1, l_2) \quad (5.3.1.1)$$

or

$$y'(l_1, l_2) = [(1-2\cos\omega_1 z_l'^{-1} + z_l'^{-2})(1-2\cos\omega_2 z_l'^{-1} + z_l'^{-2})]^{-\frac{c}{2}} \zeta(l_1, l_2) \quad (5.3.1.2)$$

$$\text{for } l_1, l_2 = 0, 1, \dots, N-1,$$

where  $z_l'$  is the delay operator associated with  $l_i$ , and  $\zeta(l_1, l_2)$  is an i.i.d. Gaussian sequence.

By the definition of DFT,  $W'(k_1, k_2)$  corresponding to white noise sequence  $\zeta'(l_1, l_2)$  is

$$W'(k_1, k_2) = \sum_{m_1=0}^{N-1} \sum_{m_2=0}^{N-1} \zeta'(l_1, l_2) \exp[-j\frac{2\pi}{N}(m_1 k_1 + m_2 k_2)] \quad (5.3.1.3)$$

and, therefore from the coordinate transformation (5.2.4),

$$\begin{aligned} W'(k_1, k_2) = & \sum_{m_1=0}^{N-1} \sum_{m_2=0}^{N-1} \zeta'(l_1, l_2) \exp[-j\frac{2\pi}{N\cos\sigma} [((\sin^2\tau + \cos\sigma\cos^2\tau)k_1 \\ & + (\cos\sigma-1)\sin\tau\cos\tau k_2)l_1 + ((\cos\sigma-1)\sin\tau\cos\tau k_1 \\ & + (\cos^2\tau + \cos\sigma\sin^2\tau)k_2)l_2]] \end{aligned} \quad (5.3.1.4)$$

Thus, we define

$$z'_1 = z_1 \frac{\sin^2 \tau + \cos \sigma \cos^2 \tau}{\cos \sigma} z_2 \frac{(\cos \sigma - 1) \sin \tau \cos \tau}{\cos \sigma} \quad (5.3.1.5a)$$

$$z'_2 = z_1 \frac{(\cos \sigma - 1) \sin \tau \cos \tau}{\cos \sigma} z_2 \frac{\cos^2 \tau + \cos \sigma \sin^2 \tau}{\cos \sigma} \quad (5.3.1.5b)$$

and

$$n_1 = \frac{1}{\cos \sigma} [(\sin^2 \tau + \cos \sigma \cos^2 \tau) k_1 + (\cos \sigma - 1) \sin \tau \cos \tau k_2], \quad (5.3.1.6a)$$

$$n_2 = \frac{1}{\cos \sigma} [(\cos \sigma - 1) \sin \tau \cos \tau k_1 + (\cos^2 \tau + \cos \sigma \sin^2 \tau) k_2] \quad (5.3.1.6b)$$

Then, from the orthographical projection, we can set

$$W'(k_1, k_2) = W(n_1, n_2). \quad (5.3.1.7)$$

Therefore, with these relations, we can have the projected version of  $Y(k_1, k_2)$ , which is the DFT of  $y'(l_1, l_2)$  as follows.

$$Y'(k_1, k_2) = [(1 - e^{-j2\pi \frac{n_1}{N}})(1 - e^{-j2\pi \frac{n_2}{N}})]^{-\frac{c}{2}} W'(k_1, k_2) \quad (5.3.1.8)$$

or

$$Y'(k_1, k_2) = [(1 - 2\cos \omega_1 e^{-j2\pi \frac{n_1}{N}} + e^{-j4\pi \frac{n_1}{N}}) \cdot (1 - 2\cos \omega_2 e^{-j2\pi \frac{n_2}{N}} + e^{-j4\pi \frac{n_2}{N}})]^{-\frac{c}{2}} W'(k_1, k_2) \quad (5.3.1.9)$$

On the other hand, the random function  $y''(l_1, l_2)$ , rotated version of  $y(l_1, l_2)$ , can be obtained by the coordinate transformation (5.2.1) and setting  $y''(l_1, l_2) = y(l'_1, l'_2)$ .

$$y''(l_1, l_2) = [(1 - z''_1)^{-1} (1 - z''_2)^{-1}]^{-\frac{c}{2}} \zeta''(l_1, l_2) \quad (5.3.1.10)$$

or

$$y''(l_1, l_2) = [(1 - 2\cos\omega_1 z''_1^{-1} + z''_1^{-2})(1 - 2\cos\omega_2 z''_2^{-1} + z''_2^{-2})]^{-\frac{c}{2}} \zeta''(l_1, l_2) \quad (5.3.1.11)$$

where  $z''_i$  is the delay operator in direction of  $l'_i$  and  $\zeta''(l_1, l_2)$  is an i.i.d Gaussian noise sequence.

Like earlier, from the definition of DFT, we now define

$$z''_1 = z_1^{\cos\theta} z_2^{\sin\theta} \quad (5.3.1.12a)$$

$$z''_2 = z_1^{-\sin\theta} z_2^{\cos\theta} \quad (5.3.1.12b)$$

and

$$n'_1 = \cos\theta k_1 + \sin\theta k_2 \quad (5.3.1.13a)$$

$$n'_2 = -\sin\theta k_1 + \cos\theta k_2 \quad (5.3.1.13b)$$

Thus, the rotated version of  $Y(k_1, k_2)$ , which is DFT of  $y''(l_1, l_2)$  is

$$Y''(k_1, k_2) = [(1 - e^{-j2\pi \frac{n'_1}{N}})(1 - e^{-j2\pi \frac{n'_2}{N}})]^{-\frac{c}{2}} W''(k_1, k_2) \quad (5.3.1.14)$$

or

$$Y''(k_1, k_2) = [(1 - 2\cos\omega_1 e^{-j2\pi \frac{n'_1}{N}} + e^{-j4\pi \frac{n'_1}{N}}) \cdot (1 - 2\cos\omega_2 e^{-j2\pi \frac{n'_2}{N}} + e^{-j4\pi \frac{n'_2}{N}})]^{-\frac{c}{2}} W''(k_1, k_2) \quad (5.3.1.15)$$

where  $W''(k_1, k_2)$  is the corresponding DFT of  $\zeta''(l_1, l_2)$

Finally, the above two coordinate transformations, the 2-D rotational and the orthographical projection coordinate transformations, can be combined to get the model for the texture pattern obtained after rotating, and slanting the plane with a tilt angle. Thus, the random function  $y'''(l_1, l_2)$ , which represents the texture pattern obtained after rotating and slanting, can be represented by

$$y'''(l_1, l_2) = [(1 - z'''_1)^{-1} (1 - z'''_2)^{-1}]^{-\frac{c}{2}} \zeta'''(l_1, l_2) \quad (5.3.1.16)$$

or

$$y'''(l_1, l_2) = [(1 - 2\cos\omega_1 z'''_1^{-1} + z'''_1^{-2})(1 - 2\cos\omega_2 z'''_2^{-1} + z'''_2^{-2})]^{-\frac{c}{2}} \zeta'''(l_1, l_2) \quad (5.3.1.17)$$

where  $z'''_i$  is the delay operator in direction of  $l''_i$  and  $\zeta'''(l_1, l_2)$  is an i.i.d. Gaussian noise sequence.

And finally we define

$$z'''_1 = z_1^{T_{11}} z_2^{T_{12}} \quad (5.3.1.18a)$$

$$z'''_2 = z_1^{T_{21}} z_2^{T_{22}} \quad (5.3.1.18b)$$

where

$$T_{11} = \frac{1}{\cos\sigma} [\cos\theta(\sin^2\tau + \cos\sigma\cos^2\tau) - \sin\theta(\cos\sigma - 1)\sin\tau\cos\tau], \quad (5.3.1.19a)$$

$$T_{12} = \frac{1}{\cos\sigma} [\sin\theta(\sin^2\tau + \cos\sigma\cos^2\tau) + \cos\theta(\cos\sigma - 1)\sin\tau\cos\tau], \quad (5.3.1.19b)$$

$$T_{21} = \frac{1}{\cos\sigma} [\cos\theta(\cos\sigma - 1)\sin\tau\cos\tau - \sin\theta(\cos^2\tau + \cos\sigma\sin^2\tau)], \quad (5.3.1.19c)$$

$$T_{22} = \frac{1}{\cos\sigma} [\sin\theta(\cos\sigma - 1)\sin\tau\cos\tau + \cos\theta(\cos^2\tau + \cos\sigma\sin^2\tau)] \quad (5.3.1.19d)$$

and

$$n''_1 = T_{11}k_1 + T_{12}k_2, \quad (5.3.1.20a)$$

$$n''_2 = T_{21}k_1 + T_{22}k_2 \quad (5.3.1.20b)$$

Thus, we get the rotated and projected version of  $Y(k_1, k_2)$ , which is DFT of

$y'''(l_1, l_2)$  as follows.

$$Y'''(k_1, k_2) = [(1 - e^{-j2\pi \frac{n''_1}{N}})(1 - e^{-j2\pi \frac{n''_2}{N}})]^{-\frac{c}{2}} W'''(k_1, k_2) \quad (5.3.1.21)$$

or

$$Y'''(k_1, k_2) = [(1 - 2\cos\omega_1 e^{-j2\pi \frac{n''_1}{N}} + e^{-j4\pi \frac{n''_1}{N}}) \cdot (1 - 2\cos\omega_2 e^{-j2\pi \frac{n''_2}{N}} + e^{-j4\pi \frac{n''_2}{N}})]^{-\frac{c}{2}} W'''(k_1, k_2) \quad (5.3.1.22)$$

where  $W'''(k_1, k_2)$  is the DFT of  $y'''(l_1, l_2)$ .

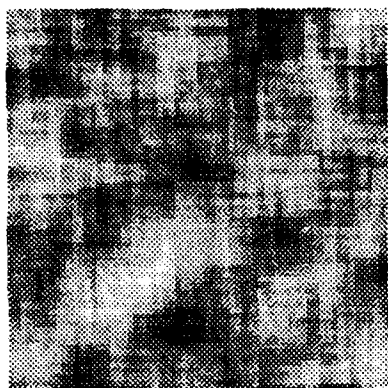
### 5.3.2. Fractal Scale As A 3-D Rotational Invariant Parameter

As shown in the previous section, the random texture  $y(m_1, m_2)$  defined on the surface normal plane can be viewed as the different random texture depending on the viewing direction. And this different looking random texture can be represented by the coordinate transformations with the surface orientation angles  $\sigma$ ,  $\tau$  and the rotation angle  $\theta$ . Thus, the original function  $y(m_1, m_2)$  is transformed to another function, such as  $y'$ ,  $y''$ ,  $y'''$ , after rotating or slanting the texture plane. However, even after rotated and slanted, the transformed random texture function shares the same value of the fractal scaling parameter  $c$  with the original texture function  $y$ . This rotational and scaling invariant property of fractal scaling parameter  $c$  plays an important role for our classification purpose. In other words, by estimating and comparing this rotational and scaling invariant fractal scale parameter, we classify the same but different looking textures due to the 3-D rotation to the same class. Following example (Figure 5.2) is given to demonstrate this 3-D rotational invariant property of the fractal scaling factor  $c$ . In this example, all texture patterns are synthesized with different values of

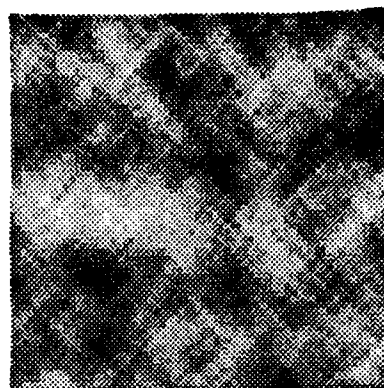
$\sigma$ ,  $\tau$ , and  $\theta$  but same values of  $\omega_1$ ,  $\omega_2$ , and  $c$  based on the transformed second-order fractional differencing periodic models (5.3.2, 5.3.1.2, 11, 17). Figure 5.2-a, b, c, d depict the original texture pattern with  $\omega_1 = 0.2$ ,  $\omega_2 = 0.2$ , and  $c = 0.8$ , the rotated texture with  $\theta = \pi/4$ , the orthographically projected texture with  $\tau = \pi/8$  and  $\sigma = -\pi/4$ , and the rotated and projected texture with  $\theta = \pi/4$ ,  $\sigma = -\pi/4$ , and  $\tau = \pi/8$ , respectively. From this example, we can see that all texture patterns are same to human eyes, even though those are projected from the different viewing directions. However, this similarity can not be caught by the conventional 2-D stochastic model-based approaches such as AR model [41, 125], facet model [179], etc., but can be caught by the fractal scaling parameter  $c$  in fractional differencing model, because all texture patterns in Figure 5.2 shares the same value of  $c$ . A detailed discussion on the estimation method of parameter  $c$  and the classification method with this parameter will be given in the next two sections.

#### 5.4. Estimation Of Parameters

There have been several approaches for estimating parameters in various kinds of fractional differencing time series since Hosking introduced Fractional Differencing model [101]. For example, Granger and Joyeux [89] approximated this model by a high-order auto-regressive process and estimated the differencing parameter by comparing variances for each different choice of it. Lapsa [121] suggested a maximum-likelihood estimator in the frequency domain and showed the consistency of the estimator. This frequency domain analysis was further studied by Eom, and a hybrid method of least-squares and maximum-likelihood estimations was recently proposed to estimate the fractal scaling parameters and the frequency parameters, respectively [67]. In this section, a least-squares or a maximum-



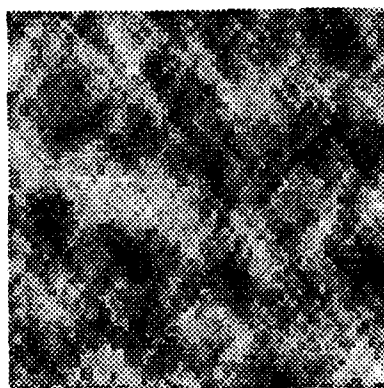
(a)



(b)



(c)



(d)

Figure 5.2: (a) A original texture pattern image with  $\omega_1 = 0.2$ ,  $\omega_2 = 0.2$ , and  $c = 0.8$  in (5.3.2). (b) Image obtained after rotating the image(Figure 5.2-a) on the image plane with  $\theta = \pi/4$  in (5.3.1.2). (c) Image obtained after projecting the image(Figure 5.2-a) orthographically, with  $\sigma = -\pi/4$  and  $\tau = \pi/8$  in (5.3.1.7). (d) Image obtained after projecting the already rotated image(Figure 5.2-b) orthographically, with  $\sigma = -\pi/4$  and  $\tau = \pi/8$  in (5.3.1.11).

likelihood estimation algorithm based on Eom's algorithm will be applied to estimate the parameters in the first-order or the second-order fractional differencing model.

#### 5.4.1. Estimation Of Parameter $c$ In The First-order Fractional Differencing Model

The estimation of fractal scaling parameter  $c$  in the un-transformed first-order fractional differencing model (5.3.1) can be done by a simple least-square estimation scheme in the frequency domain based on a representation of the logarithm of the process which is linear in the parameters as follows. By applying logarithm operator to (5.3.1), we obtain

$$\begin{aligned}\log |Y(k_1, k_2)| &= -\frac{c}{2} [\log |1 - e^{-j2\pi \frac{k_1}{N}}| + \log |1 - e^{-j2\pi \frac{k_2}{N}}|] + \log |W(k_1, k_2)| \\ &= -\frac{c}{2} [\log |2\sin(\frac{\pi k_1}{N})| + \log |2\sin(\frac{\pi k_2}{N})|] + \log |W(k_1, k_2)|\end{aligned}\tag{5.4.1.1}$$

$$\begin{aligned}&= -\frac{c}{2} [\log |2\sin(\frac{\pi k_1}{N})| + \log |2\sin(\frac{\pi k_2}{N})|] - \alpha + V(k_1, k_2) \\ &, \text{ for } k_1, k_2 = 0, 1, \dots, N-1\end{aligned}\tag{5.4.1.2}$$

where  $\alpha = -E[\log |W(k_1, k_2)|]$  and  $V(k_1, k_2) = \log |W(k_1, k_2)| + \alpha$ .

Then  $\eta = (c, \alpha)^T$  can be estimated by minimizing the following cost function.

$$J(\eta, \omega_1, \omega_2) = \sum_{k_1=0}^{N-1} \sum_{k_2=0}^{N-1} (\log |Y(k_1, k_2)| + \frac{c}{2} [\log |2\sin \frac{\pi k_1}{N}| + \log |2\sin \frac{\pi k_2}{N}|] + \alpha)^2 \quad (5.4.1.3)$$

$$= \sum_{k_1=0}^{N-1} \sum_{k_2=0}^{N-1} (\log |Y(k_1, k_2)| - \eta^T Q(k_1, k_2))^2 \quad (5.4.1.4)$$

Here,

$$Q(k_1, k_2) = \begin{bmatrix} -\frac{1}{2} (\log |2\sin \frac{\pi k_1}{N}| + \log |2\sin \frac{\pi k_2}{N}|) \\ -1 \end{bmatrix}. \quad (5.4.1.5)$$

Thus, the estimated values will be

$$[\hat{c}, \hat{\alpha}]^T = \left( \sum_{k_1=0}^{N-1} \sum_{k_2=0}^{N-1} Q(k_1, k_2) Q^T(k_1, k_2) \right)^{-1} \left( \sum_{k_1=0}^{N-1} \sum_{k_2=0}^{N-1} Q(k_1, k_2) \log |Y(k_1, k_2)| \right). \quad (5.4.1.6)$$

#### 5.4.2. Estimation Of Parameters $\omega_1, \omega_2, \sigma, \tau, \theta$ In The Projected Second-Order Fractional Differencing Periodic Model

Consider the transformed fractional differencing periodic model obtained after rotating and projecting (5.3.1.17) and its DFT as follows.

$$Y'''(k_1, k_2) = [(1 - 2\cos\omega_1 e^{-j2\pi \frac{n''_1}{N}} + e^{-j4\pi \frac{n''_1}{N}})]$$

$$\cdot (1 - 2\cos\omega_2 e^{-j2\pi \frac{n''_2}{N}} + e^{-j4\pi \frac{n''_2}{N}})^{-\frac{c}{2}} W'''(k_1, k_2) \quad (5.4.2.1)$$

where  $W'''(k_1, k_2)$  is the DFT of  $y'''(l_1, l_2)$  in (5.3.1.17) and  $n''_i$  is same as defined in (5.3.1.20).

Then, the estimation of parameters in (5.3.1.17) can be done in the frequency domain, modifying the techniques suggested in previous section.

For estimation, all parameters can be estimated directly from the given data  $Y'''(k_1, k_2)$  (5.3.1.22), if we can obtain the likelihood function of  $|Y(k_1, k_2)|$ . Then, since the noise sequence  $\zeta'''(l_1, l_2)$  is assumed to be white Gaussian,  $W'''(k_1, k_2)$  and  $Y'''(k_1, k_2)$  follow the Rayleigh distribution as in Theorem 4.3.1. From these probabilistic properties, the estimation of parameters can be done by a hybrid method of Least Square and Maximum Likelihood estimations, which was suggested by Eom [67]. For LS estimation, if parameters  $\omega_1, \omega_2, \sigma, \tau, \theta$  are set, then  $\eta = (c, \alpha)^T$  can be estimated by minimizing the following cost function as described in section 5.4.1.

$$J(\eta, \omega_1, \omega_2) = \sum_{k_1=0}^{N-1} \sum_{k_2=0}^{N-1} (\log |Y'''(k_1, k_2)| + \frac{c}{2} (\log |2\cos \frac{2\pi n''_1}{N} - 2\cos\omega_1| + \log |2\cos \frac{2\pi n''_2}{N} - 2\cos\omega_2|) + \alpha)^2 \quad (5.4.2.2)$$

$$= \sum_{k_1=0}^{N-1} \sum_{k_2=0}^{N-1} (\log |Y'''(k_1, k_2)| - \eta^T Q(k_1, k_2))^2 \quad (5.4.2.3)$$

where  $\alpha = -E[\log |W'''(k_1, k_2)|]$ ,  $\eta = (c, \alpha)^T$ .

Here,

$$Q(k_1, k_2) = \begin{bmatrix} \frac{-1}{2} (\log |2\cos \frac{2\pi n''_1}{N} - 2\cos \omega_1| + \log |2\cos \frac{2\pi n''_2}{N} - 2\cos \omega_2|) \\ -1 \end{bmatrix} \quad (5.4.2.4)$$

Thus, the estimated values will be

$$[\hat{c}, \hat{\alpha}]^T = \left( \sum_{k_1=0}^{N-1} \sum_{k_2=0}^{N-1} Q(k_1, k_2) Q^T(k_1, k_2) \right)^{-1} \left( \sum_{k_1=0}^{N-1} \sum_{k_2=0}^{N-1} Q(k_1, k_2) \log |Y'''(k_1, k_2)| \right) \quad (5.4.2.5)$$

Also, ML estimators of  $\omega_1$ ,  $\omega_2$ ,  $\sigma$ ,  $\tau$ ,  $\theta$  can be calculated by maximizing the log-likelihood function  $L(Y; \eta, \omega_1, \omega_2)$  with  $\hat{\alpha}$  estimated from above.

$$\begin{aligned} L(Y; \eta, \omega_1, \omega_2) &= \sum_{k_1=0}^{N-1} \sum_{k_2=0}^{N-1} \log |Y'''(k_1, k_2)| - \sum_{k_1=0}^{N-1} \sum_{k_2=0}^{N-1} \log \left( \frac{\rho N^2}{2} \right) \\ &+ \frac{c}{2} N \left( \sum_{k_1=0}^{N-1} \log \left| 2 \left( \cos \frac{2\pi n''_1}{N} - \cos \omega_1 \right) \right| + \sum_{k_2=0}^{N-1} \log \left| 2 \left( \cos \frac{2\pi n''_2}{N} - \cos \omega_2 \right) \right| \right) \\ &- \frac{1}{\rho N^2} \sum_{k_1=0}^{N-1} \sum_{k_2=0}^{N-1} \left( \left| 2 \left( \cos \frac{2\pi n''_1}{N} - \cos \omega_1 \right) \right| \cdot \left| 2 \left( \cos \frac{2\pi n''_2}{N} - \cos \omega_2 \right) \right| \right)^c \\ &\cdot |Y'''(k_1, k_2)|^2 \end{aligned} \quad (5.4.2.6)$$

where  $\rho$  is a variance of  $\zeta'''(l_1, l_2)$  and can be estimated by the following equation in mean square sense.

$$\hat{\rho} = \frac{1}{N^2} \exp \left\{ \gamma - 2\hat{\alpha} - \frac{\pi^2}{6N^2} \right\} \quad (5.4.2.7)$$

where  $\gamma$  is Euler's constant ( $= 0.5772157$ ) [67].

Therefore, the estimation scheme can be summarized as follows:

(Estimation Algorithm)

- Step 1: Choose resonant frequencies  $\omega_1, \omega_2$  in the range  $[0, \pi/2]$ , the surface orientation parameters  $\sigma, \tau$  and the rotational parameter  $\theta$  in the range  $[-\pi/2, \pi/2]$ .
- Step 2: With the given values of  $\omega_1, \omega_2, \sigma, \tau$ , and  $\theta$ , estimate  $c$  and  $\alpha$  by LS estimation algorithm (5.4.2.5).
- Step 3: Using  $\hat{\alpha}$ , compute the estimate of the variance of  $\zeta'''(l_1, l_2), \rho$ , by equation (5.4.2.7).
- Step 4: Using the estimates  $\hat{c}$  and  $\hat{\rho}$  found in Step 2 and 3, maximize the likelihood function given by (5.4.2.6) with respect to  $\omega_1, \omega_2, \sigma, \tau$ , and  $\theta$ .
- Step 5: Using the estimates  $\hat{\omega}_1, \hat{\omega}_2, \hat{\sigma}, \hat{\tau}$ , and  $\hat{\theta}$ , repeat steps 2 to 4 until the estimates have no significant change in successive iterations.

## 5.5. Multi-level 3-D Rotational Invariant Classification Scheme

In this section, a two-level hierarchical classification structure is developed to classify the 3-D rotated texture patterns. In first level of classification scheme, a 3-D rotational invariant feature  $c$  is extracted from the input image data based on the first-order fractional differencing model (5.3.1), and this fractal scale feature is used to classify the textures to the classes whose members are sharing similar value of fractal scaling parameter  $c$ . In second level, each class is divided to the final desired subclasses based on two other texture pattern features,  $\omega_1$  and  $\omega_2$ , and in each class assigned in first level, the input texture image is classified further in more detail with

the features  $\omega_1, \omega_2$  which is extracted based on the rotated and projected fractional differencing periodic model (5.3.1.16). Figure 5.3 shows this hierarchical structured classification scheme. Notice that it is possible for some textures to belong to the different classes simultaneously, depending their variance values of  $c$ . For this classification scheme, the images are separated into test and training sets. The class of textures and the number of classes in training set is assumed to be known *a priori*.

This multi-level classification structure has several advantages over the conventional classification methods. First, this algorithm can save the processing time to classify the texture images. Because this algorithm uses a least mean square estimation to get the fractal scaling feature  $c$  in first-level, the processing time will be reduced comparing with the method which is relying on only a maximum likelihood estimation techniques. MLE algorithm requires long computational time because of its iteration scheme to get the maximum value from the likelihood function. And second, comparing with the classification methods which have only one feature parameter  $c$ , the more accurate classification can be achieved by this algorithm. In other words, even for the case that two texture images have close values of fractal scale (roughness of the surface) but those are same patterns of texture, this algorithm has the ability to classify the textures based on the estimated values of parameters  $\omega_1, \omega_2$  in second level of this classification structure. A more detailed discussion on each level of classification scheme will be given in following sections.

### 5.5.1. The First-Level Of Classification

In this level, the different 3-D rotated texture images are classified into the  $M$  different classes depending on their estimated values of the fractal scale. As discussed in section 5.3.2, this fractal scaling feature is a rotational and scaling invariant feature,

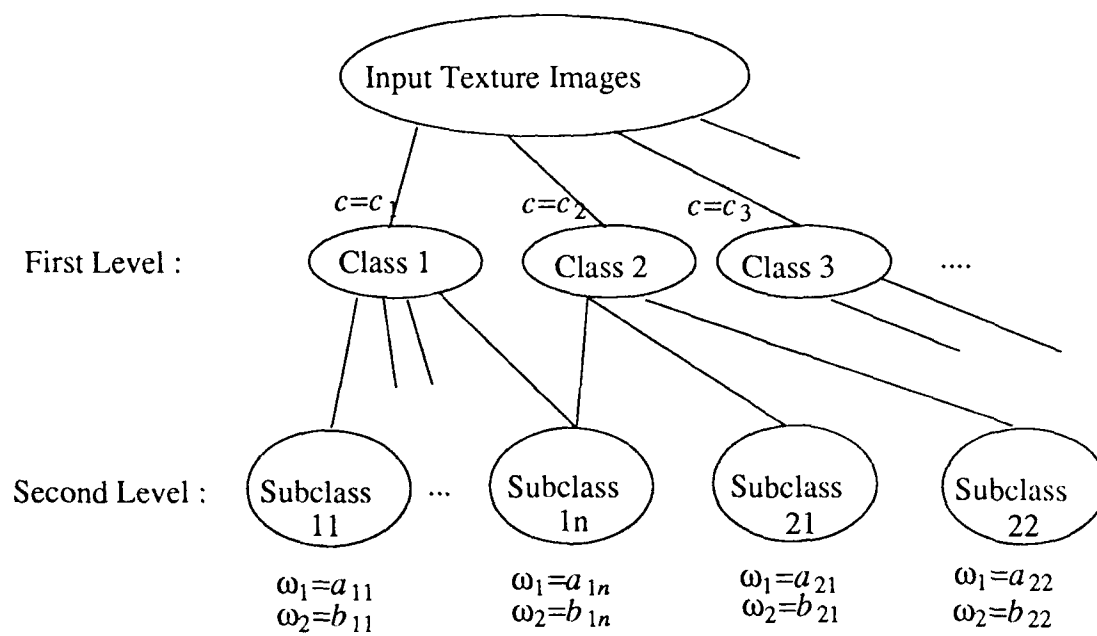


Figure 5.3: Two-level hierarchical classification structure

and represents the roughness of the texture plane surface. In other words, if we consider a first-order fractional differencing model, the transformed image function  $y'''(l_1, l_2)$  obtained after rotating and projecting (5.3.1.16) will have same fractal scale as the original function  $y(m_1, m_2)$  (5.3.1). Therefore, if we want to estimate the fractal scale  $c$  only, we do not need to apply the transformed function but only need to apply the original function which does not contain the rotation parameter  $\theta$ , or the surface orientation parameters  $\tau, \sigma$  in it. Therefore, the estimation of  $c$  parameter can be done by a simple least-square estimate method described in section 5.4.1.

Actual classification is achieved by applying a distance classifier  $d(c, i)$ , which measures a weighted distance between the extracted feature of test image denoted by  $\hat{c}$  and the mean feature of each of  $M$  classes. Then the texture is classified to class  $A_i$  for which such a distance is minimum. That is,

$$i^* = \underset{i}{\text{minimum}} d(c, i), \quad i = 1, \dots, M \quad (5.5.1.1)$$

where

$$d(c, i) = \frac{[\hat{c} - \bar{c}_i]}{\sum_{j=1}^M [\sigma_c^2]^{(j)}} \quad (5.5.1.2)$$

and  $\bar{c}_i$  and  $[\sigma_c^2]^{(i)}$  correspond to the sample mean and variance of the feature  $c$  in class  $A_i$ , respectively.

Then, it should be noticed that class  $A_i$  could consist of several different texture classes in the case that the different textures share the same fractal scale (the roughness of the surface), but have different patterns. This means that sometimes, checking the fractal scale only is not enough to distinguish the different patterns of texture. Thus, we need an additional classification scheme to distinguish these even in the same class  $A_i$ . This additional classification will be done in second level of

classification structure. Here, the number of first-level classes  $M$  is chosen considering the sample means and variances of the fractal scale  $c$  of the sample texture images. For example, if two different texture patterns have close enough sample means of fractal scale each other, such that the range  $[\bar{c} - \sigma_c^2, \bar{c} + \sigma_c^2]$  of one texture is overlapped with the other, these two texture patterns could be classified to the same class in first-level. Thus, it should be noticed that it is possible for a texture to belong to several different classes simultaneously, depending its value of  $c$ .

### 5.5.2. The Second-Level of Classification

This second-level of classification is an optional procedure. If one fractal scale feature is enough to classify the texture in first-level, in other words, if the class  $A_i$  in first-level contains only one member in it, our classification could be terminated in first-level. On the other hand, if the class has several members in it, the classification is continued to the second-level. In second-level, the textures which were already classified to the same class in first-level are split to the different sub-classes, based on the values of pattern features  $\omega_1, \omega_2$  in the second-order fractional differencing periodic function (5.3.1.21). Thus, the estimation of those parameters can be completed by a Maximum Likelihood Estimation (MLE) technique discussed in section 5.4.2, and these extracted features denoted by  $\hat{\Omega}^{(k)} = \{\hat{\omega}_1^{(k)}, \hat{\omega}_2^{(k)}\}$  are used for further classification by measuring another weighted distance between these features and the mean feature of each of the  $N$  subclasses in a particular class  $A_i$ . Similarly to the first-level,

$$k^* = \underset{k}{\text{minimum}} d(\hat{\Omega}^{(k)}, k), \quad k = 1, \dots, N \quad (5.5.2.1)$$

where

$$d(\hat{\Omega}^{(k)}, k) = \sum_{f=\hat{\omega}_1, \hat{\omega}_2} \left\{ \frac{[f - \bar{f}^{(k)}]}{\sum_{j=1}^N [\sigma_f^2]^{(j)}} \right\} \quad (5.5.2.2)$$

and  $\bar{f}^{(k)}$  and  $[\sigma_f^2]^{(k)}$  correspond to the sample mean and variance of subclass (k) features, respectively. Here, it should be noticed that since we have at most several subclasses from a first-level class, we need to compare only a small number of subclasses to complete the classification, instead of checking the feature distance of whole other texture classes. Thus, we can save the total processing time of classification by using this multi-level structure. Therefore, from this multi-level classification method, we could get the accurate classification and save the processing time at the same time.

## 5.6. Experimental Results

For these experiments, nine different classes of texture were taken from Brodatz's standard texture album [28] for the training set. These are, namely, grass[D9], tree bark[D12], straw[D15], herringbone weave[D17], woolen cloth[D19], calf leather[D24], beach sand[D29], water[D37], and raffia[D84]. Figure 5.4 shows the 256×256 original texture images of these.

For the actual training, sixteen 64×64 sized sample image data were taken for each different texture pattern, and the sample mean and variance of parameters,  $c$ ,  $\omega_1$ , and  $\omega_2$  were obtained for each texture class, based on the first and second-order fractional differencing models [Table 5.1]. As we can see from Table 5.1, fractal scale  $c$  itself is not enough to classify the different textures, because some of textures have similar values of  $c$ , even though they are different texture patterns. This is the reason why the classification will be completed in second level by considering

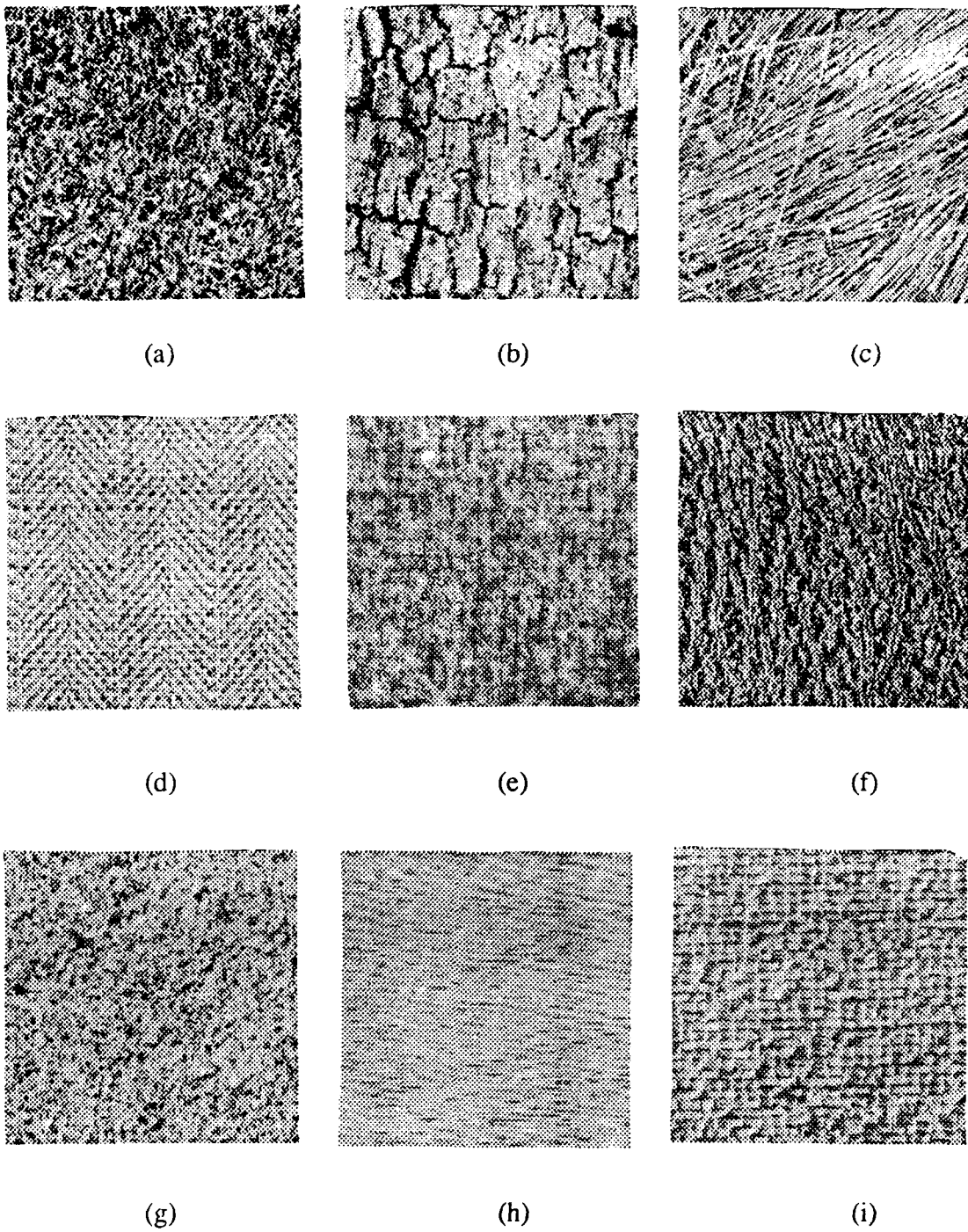


Figure 5.4: 256×256 original texture images of training set: (a) grass (b) tree bark (c) straw (d) herringbone weave (e) woolen cloth (f) calf leather (g) beach sand (h) water (i) raffia

additional parameter values of  $\omega_1$ ,  $\omega_2$ . As mentioned before, since the estimation of  $c$  can be done by simple Least-square estimation and the estimation of  $\omega_1$ ,  $\omega_2$  can be done by Maximum Likelihood estimation, the two-level hierarchical classification structure induces the reasonably reduced processing time preserving the accuracy of the classification. Based on these sample mean and variance values, the number of classes for the first level of classification,  $M = 5$ , were determined. The following table [Table 5.2] shows the final classes for the first level of classification, and the corresponding sample mean and variance of each class. Notice that the herringbone weave texture belongs to the class 2 and 3, because of its high value of variance. Then, for the second level of classification, subclasses can be taken as the members of each class based on the different values of  $\omega_1$  and  $\omega_2$ .

#### 5.6.1. 2-D Rotated Texture Case

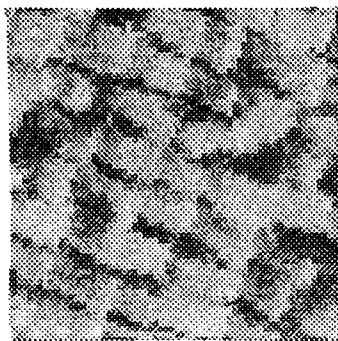
In this experiment, the test input images were taken from the 2-D raffia textures rotated by various angle  $\theta$ s (Figure 5.5). Then, each  $64 \times 64$  texture was classified by the proposed multi-level classification scheme. For the first level, the fractal scale parameter  $c$  was extracted based on the first-order Fractional Differencing model (5.3.1), and the parameters,  $\omega_1$  and  $\omega_2$ , were extracted from the second-order Fractional Differencing periodic model (5.3.1.11). Actual classification of the test images was done in each level by comparing weighted distances (5.5.1.1-2, 5.5.2.1-2) between the extracted features and the data base. The classification results are presented in Table 5.3. Table 5.3 shows the parameter values extracted from each rotated texture pattern and the demonstrates the perfect result of classification based on these values.

Table 5.1: The sample mean and variance of parameter  $c$ ,  $\omega_1$ ,  $\omega_2$ : 16 64×64 sample image data are taken for each different texture classes, and the parameter values are extracted from the first and second-order fractional differencing models (5.3.1-2).

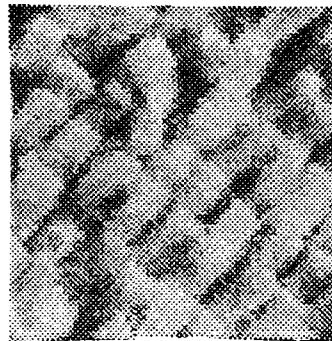
Textures	c		$\omega_1$		$\omega_2$	
	$\bar{x}$	$\sigma^2$	$\bar{x}$	$\sigma^2$	$\bar{x}$	$\sigma^2$
grass	1.209	0.057	0.744	0.078	0.636	0.082
tree bark	1.530	0.073	0.691	0.199	0.601	0.324
straw	0.923	0.053	0.387	0.068	1.209	0.070
herringbone weave	1.003	0.072	1.263	0.114	1.175	0.167
woolen cloth	0.809	0.024	0.852	0.095	0.793	0.098
calf leather	1.064	0.044	1.175	0.114	0.935	0.122
beach sand	1.195	0.038	0.665	0.107	0.571	0.129
water	1.074	0.055	0.083	0.064	0.972	0.132
raffia	1.547	0.062	1.042	0.153	0.988	0.165

Table 5.2: Database of the first level of classification.  $\bar{c}_i$  and  $\sigma_i^2$  are the sample mean and the variance of class  $i$ , respectively.

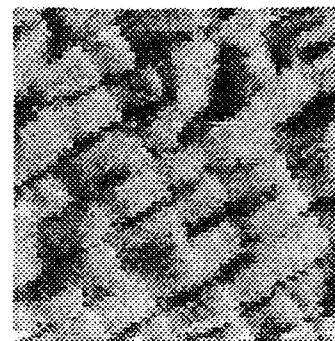
Class	Textures	$\bar{c}_i$	$\sigma_i^2$
1	woolen cloth	0.809	0.024
2	straw, herringbon weave	0.963	0.063
3	herringbon weave, calf leather, water	1.047	0.055
4	grass, beach sand	1.202	0.045
5	tree bark, raffia	1.539	0.067



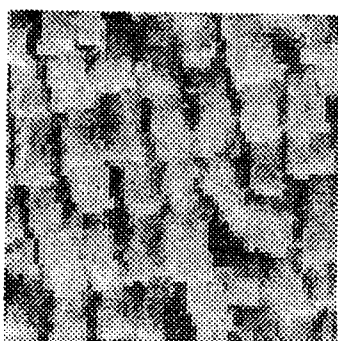
(a)



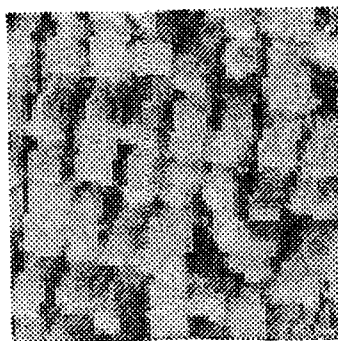
(b)



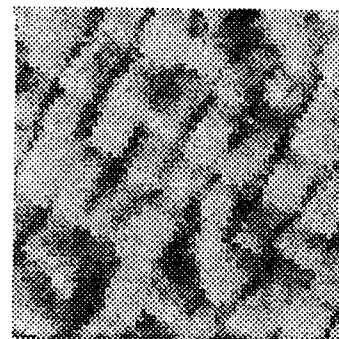
(c)



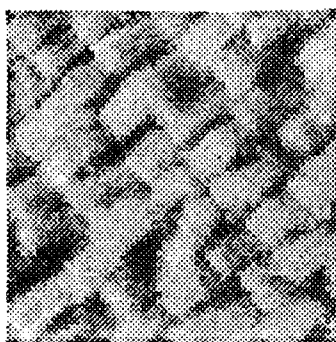
(d)



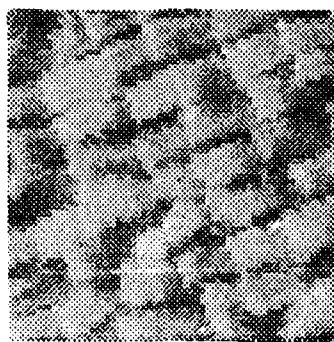
(e)



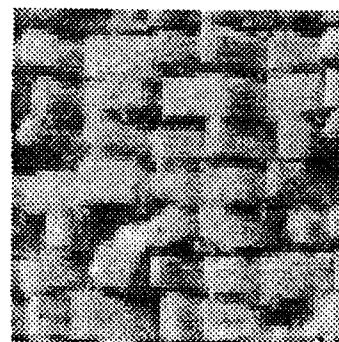
(f)



(g)



(h)



(i)

Figure 5.5: 64×64 raffia texture images rotated by  $\theta$ s: (a)  $\theta = 20^\circ$  (b)  $\theta = 40^\circ$  (c)  $\theta = 60^\circ$  (d)  $\theta = 80^\circ$  (e)  $\theta = 100^\circ$  (f)  $\theta = 120^\circ$  (g)  $\theta = 140^\circ$  (h)  $\theta = 160^\circ$  (i)  $\theta = 180^\circ$

Table 5.3: Classification results from the 2-D rotated texture images. (Result indicates the result class after applying 2-level classification method.)

Angles	$c$	$\omega_1$	$\omega_2$	Result
20	1.523	1.132	1.098	raffia
40	1.517	1.144	1.102	raffia
60	1.535	1.138	1.119	raffia
80	1.537	1.142	1.120	raffia
100	1.532	1.139	1.118	raffia
120	1.529	1.138	1.120	raffia
140	1.527	1.135	1.097	raffia
160	1.533	1.140	1.113	raffia
180	1.525	1.133	1.099	raffia

### 5.6.2. Orthographically Projected Texture Case

Six 64×64 test input images were taken in this experiment from the herringbone weave textures projected orthographically from the various tilted and slanted texture surface (Figure 5.6). Then, each texture was classified by the proposed multi-level classification scheme. Like in previous experiment, for the first level, the fractal scale parameter  $c$  was extracted based on the first-order Fractional Differencing model (5.3.1), and the parameters,  $\omega_1$  and  $\omega_2$ , were extracted from the second-order Fractional Differencing periodic model (5.3.1.2). The parameter values extracted from each projected texture pattern and the classification results from this experiment are presented in Table 5.4. Here, notice that the first test texture was assigned to Class 3 for the first level, and misclassified to the calf leathre texture, because these two texture patterns share the close values of parameters.

Table 5.4: Classification results from the orthographically projected herringbone weave texture images. (Result indicates the result class after applying 2-level classification method.)

Angles	$\hat{c}$	$\hat{\omega}_1$	$\hat{\omega}_2$	Result
$\tau = 0^\circ, \sigma = 15^\circ$	0.997	1.189	1.077	calf leather
$\tau = 0^\circ, \sigma = 30^\circ$	1.012	1.223	1.102	herringbone weave
$\tau = 0^\circ, \sigma = 45^\circ$	1.055	1.218	1.096	herringbone weave
$\tau = 45^\circ, \sigma = 15^\circ$	0.980	1.197	1.113	herringbone weave
$\tau = 45^\circ, \sigma = 30^\circ$	1.023	1.209	1.100	herringbone weave
$\tau = 45^\circ, \sigma = 45^\circ$	1.046	1.207	1.108	herringbone weave

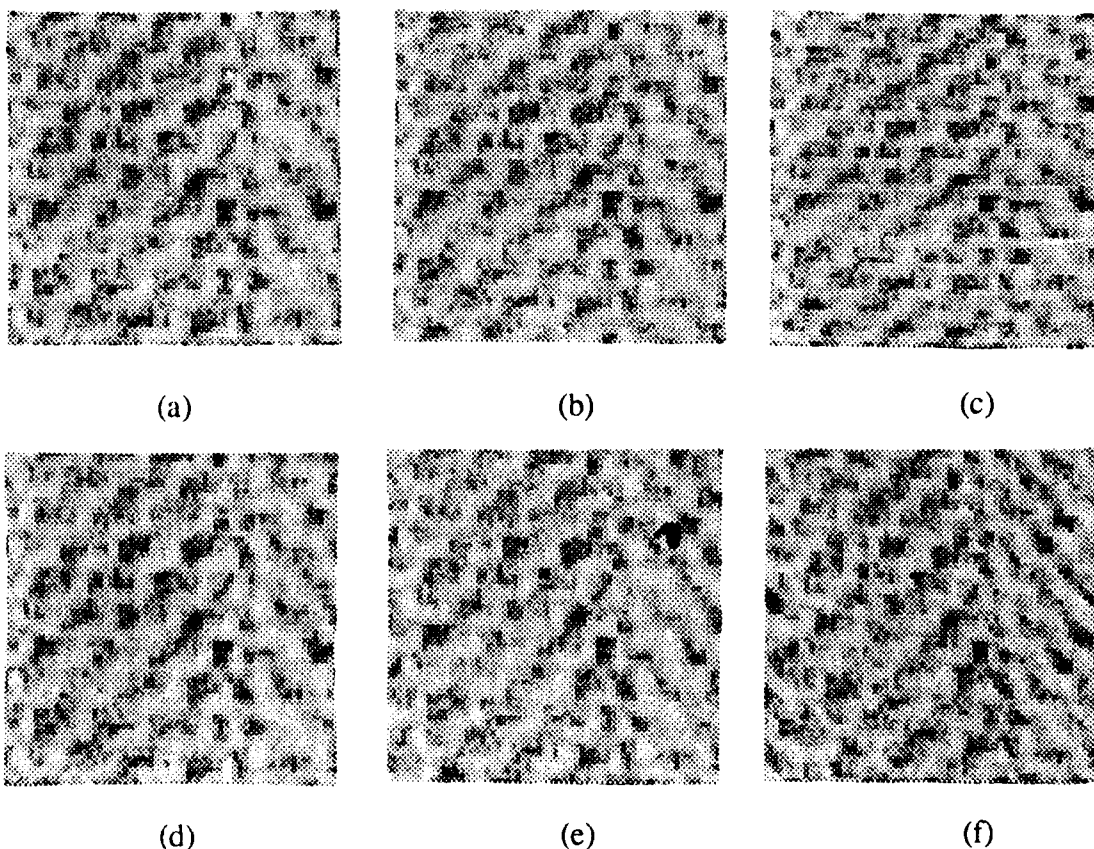


Figure 5.6: 64×64 herringbone texture images projected orthographically from the various tilted and slanted texture surface ( $\tau, \sigma$  are the tilted and slanted angles): (a)  $\tau = 0^\circ, \sigma = 15^\circ$  (b)  $\tau = 0^\circ, \sigma = 30^\circ$  (c)  $\tau = 0^\circ, \sigma = 45^\circ$  (d)  $\tau = 45^\circ, \sigma = 15^\circ$  (e)  $\tau = 45^\circ, \sigma = 30^\circ$  (f)  $\tau = 45^\circ, \sigma = 45^\circ$

### 5.6.3. Rotated And Projected Texture Case

In this experiment, six 64×64 test input images were taken from the straw textures rotated and projected orthographically from the various tilted and slanted texture surface (Figure 5.7). Like in previous experiments, for the first level, the fractal scale parameter  $c$  was extracted based on the first-order Fractional Differencing model (5.3.1), and the parameters,  $\omega_1$  and  $\omega_2$ , were extracted for the second level of classification from the second-order Fractional Differencing periodic model (5.3.1.17). The classification results from this experiment are presented in Table 5.5. Table 5.5 shows the parameter values extracted from each rotated and projected texture pattern and demonstrates the perfect result of classification based on these values.

## 5.7. Conclusions

A new multi-level classification technique was proposed to classify the 3-D rotated texture surface. Unlike most classification schemes which have been suggested to date, this classification method can handle arbitrary 3-D rotated samples of textures, i.e., the accuracy of classification is not affected by the 3-D rotation of the test texture. The proposed multi-level classification scheme consists of two levels of classification procedure. In the first level of classification, a 3-D rotational invariant feature  $c$  (fractal scale) in the first-order Fractional Differencing model was extracted, and based on this value, the test data image was classified to a certain class. In the second level, each class was divided to the final desired subclasses based on two other texture pattern features,  $\omega_1$  and  $\omega_2$ , which were extracted from the second-order Fractional Differencing periodic model. Then the input texture image was classified further in detail with these two pattern features. This multi-level classification has several

Table 5.5: Classification results from the rotated and orthographically projected straw texture images. (Result indicates the result class after applying 2-level classification method.)

Angles	$\hat{c}$	$\hat{\omega}_1$	$\hat{\omega}_2$	Result
$\theta = 0^\circ, \tau = 0^\circ, \sigma = 15^\circ$	0.914	0.365	1.189	straw
$\theta = 45^\circ, \tau = 0^\circ, \sigma = 30^\circ$	0.932	0.371	1.224	straw
$\theta = 90^\circ, \tau = 0^\circ, \sigma = 45^\circ$	0.928	0.373	1.218	straw
$\theta = 0^\circ, \tau = 45^\circ, \sigma = 15^\circ$	0.918	0.368	1.156	straw
$\theta = 45^\circ, \tau = 45^\circ, \sigma = 30^\circ$	0.922	0.375	1.191	straw
$\theta = 90^\circ, \tau = 45^\circ, \sigma = 45^\circ$	0.927	0.377	1.202	straw

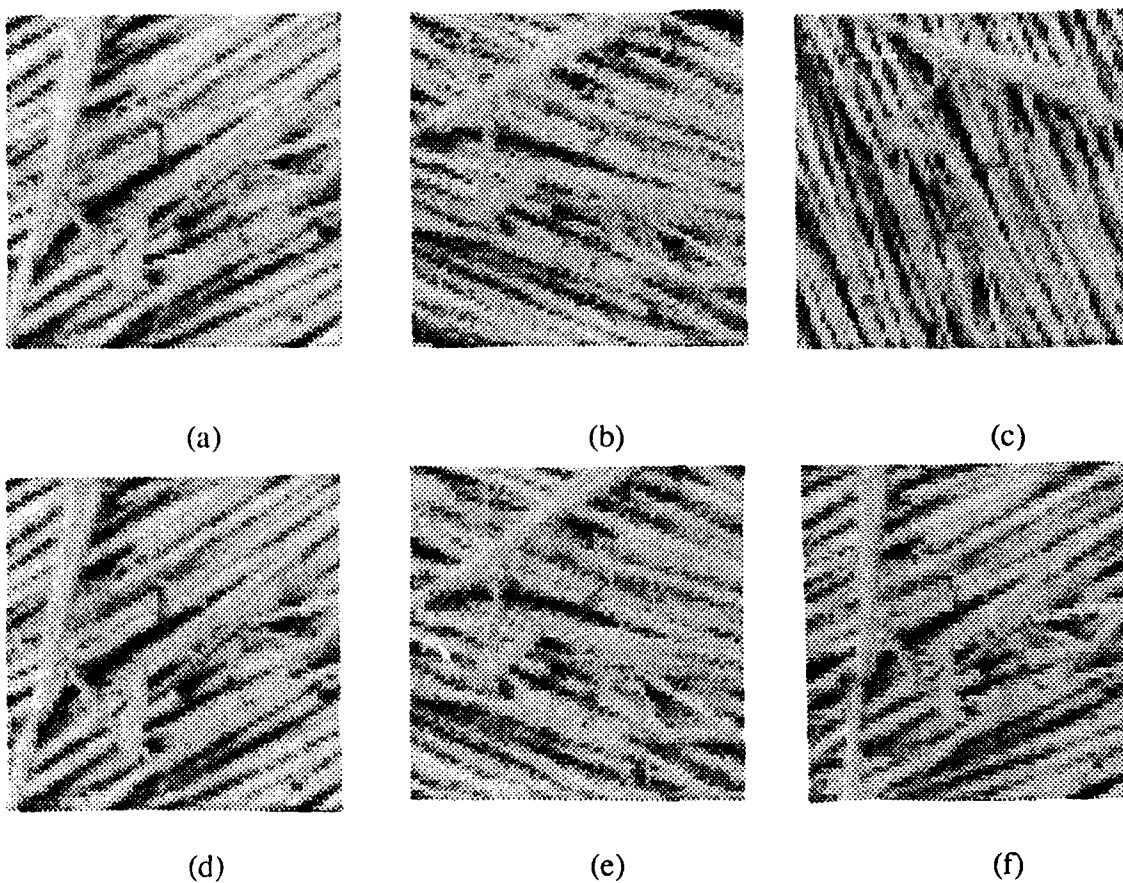


Figure 5.7: 64×64 straw texture images rotated and projected orthographically from the various tilted and slanted texture surface ( $\theta, \tau, \sigma$  are the rotated, tilted and slanted angles.): (a)  $\theta = 0^\circ, \tau = 0^\circ, \sigma = 15^\circ$  (b)  $\theta = 45^\circ, \tau = 0^\circ, \sigma = 30^\circ$  (c)  $\theta = 90^\circ, \tau = 0^\circ, \sigma = 45^\circ$  (d)  $\theta = 0^\circ, \tau = 45^\circ, \sigma = 15^\circ$  (e)  $\theta = 45^\circ, \tau = 45^\circ, \sigma = 30^\circ$  (f)  $\theta = 90^\circ, \tau = 45^\circ, \sigma = 45^\circ$

advantages over the conventional one-level classification methods. First, since this algorithm uses a simple LS estimation to get the fractal scale  $c$  in first level, the processing time of the classification is reduced comparing to the methods that rely on only ML estimation. Second, from the additional texture patterns  $\omega_1, \omega_2$  in second level, the more accurate classification can be achieved compared to the classification methods which have only one feature parameter  $c$ . As a result of a series of experiments involving the differently oriented samples of natural textures, it is concluded that these combined features make possible for this multi-level classification method to have a strong class separability power for arbitrary oriented 3-D texture patterns.

## CHAPTER 6

### CONCLUSION AND FUTURE RESEARCH

#### 6.1. Conclusions

The modeling and analysis of texture pattern of a three dimensional surface have been investigated. Since 3-D natural scene image contains both radiance and texture information, 3-D texture analysis can not be done by either shading analysis or texture analysis only. Also, the distortion of the regular texture pattern due to the 3-D surface orientation makes it difficult to analyze 3-D texture by the conventional stationary random field texture model. Thus, in this thesis, 3-D surface model which can handle both shading and texture information and 3-D texture analyses which are not affected by 3-D surface orientation have been emphasized.

The contribution of the research can be summarized as follows. First, the orthographically projected fractional differencing model was introduced to represent the orthographically projected texture pattern due to the 3-D surface orientation. This model has an ability to synthesize a long-correlated or a short-correlated random texture with various values of fractal scale parameters  $c$  and  $d$ , and the roughness and the distorted texture pattern of the 3-D surface simultaneously.

Second, the estimation scheme of the parameters of the orthographically projected fractional differencing model was developed based on a hybrid method of

the least mean square and maximum likelihood estimations. For the estimation of the fractal scaling parameter, this estimation scheme is much simpler than the fractional Brownian process based model's, because of its discrete process. Rotational and scaling invariant properties of the parameters were presented. Thus, even after performing several linear coordinate transformations, all Gaussian assumptions of random noise were preserved.

Third, a composite model of the Shape-from-shading and the Shape-from-texture has been proposed to represent a natural scene which contains both shading and texture information, considering the scene as the superposition of a deterministic function and a random texture. Surface orientations and the illumination direction were extracted directly from a single natural scene image without any pre-processing. This avoids the possible error cumulation from each process step. Also, comparing with the conventional Shape-from-shading techniques, this composite model gives unique and more reliable solutions for the surface orientation parameter values, because of the additional constraint from the texture function part.

Fourth, a multi-level 3-D rotational invariant classification scheme has been developed, based on the first and second-order fractional differencing models. Multi-level structure of this classification consists of two hierarchical levels. In the first level, the fractal scale which is known to be a rotational and scaling invariant parameter was extracted from the first-order fractional differencing model, and with this value, preliminary classification has been done. In the second level, the more detailed classification has been achieved with additional texture pattern parameters from the second-order fractional differencing model. This hierarchical structure could reduce the total processing time from the simple least mean square estimation scheme for the first level, and at the same time, it could preserve the accuracy of the classification from the second level of classification.

## **6.2. Suggestions For Future Research**

In addition to the pattern analyses of the texture on 3-D surface, which are developed in this thesis, several related works can be suggested as follows.

### **6.2.1. Neural Network Analysis For The Global Optimization Problem**

In the maximum likelihood estimation procedure, the optimization routine maximizes the likelihood function. Since our likelihood function is a complicated non-linear function and the existing approximation techniques for getting the maximum value from the non-linear function require a great many iterations, the computational time is enormous. Recently, based on the parallel processing structure of the computer, some researchers claim that neural network analysis is one of the promising techniques for reducing the computational time for optimization [163]. Therefore, investigating the applicability of neural network analysis to the maximization of the likelihood function will be valuable.

### **6.2.2. Modified Scheme Of The Shape From Shading And Texture**

#### **Method With Weighting Factor**

The proposed composite model of the Shape-from-shading and the Shape-from-texture does not have any weighting factor between both 3-D analysis techniques. However, in situation that the radiance information is more dominant than the texture information, or in the reverse situation, the estimated surface orientations from the

Shape-from-shading or Shape-from-texture technique only can be more reliable. Therefore, if we have a proper criterion to select either technique or the proposed composite model to represent the part of the surface image data, we may improve the results. One of the possible way to do this will be given by checking the fractal scale of the surface. In [176], Pentland described the fractal scaling factor as a measure of the roughness of surface. That is, if the fractal scale  $c \approx 0$ , it represents the smooth surface with gentle random undulations. In contrast, the surface with fractal scale  $c > 0$  are not perceived as smooth, but rather as being rough or three-dimensionally textured. Thus, by checking the estimated value of  $c$ , it can be possible to make decision which technique should be preferred.

### **6.2.3. High Resolution Analysis For The Texture Pattern**

Our proposed texture model in chapter 4 is based on local patch analysis. In the simulation part of this thesis, we used a  $16 \times 16$  sized patch taken from the center of a  $32 \times 32$  sized patch to build the whole image. There is a minimum requirement on the size of each patch for being able to extract meaningful statistical information from the patch. This is the bottleneck for the high resolution analysis. Since the elementary unit for surface orientation is a single patch (we assume each patch to be a plane and consequently the values for the surface orientation parameters  $\sigma$ ,  $\tau$  are constants over the patch), the end result is a low resolution analysis. Therefore, we need to develop a high resolution scheme based on a single pixel instead of a complete patch. Therefore, if we can develop a pixel based model, the synthesis of 3-D texture can be done by just adopting the surface orientation parameter values recursively for each pixel.

#### **6.2.4. Robust Estimation For The Contaminated Gaussian Noise Case**

The estimation procedure which is proposed in this thesis is based on the assumption that the input noise has a pure Gaussian distribution. However, in the real world, pure Gaussian noise does not exist. Therefore, even if we have noise which is made of Gaussian noise mixed with a small portion of other distributed noise, our estimation will not give the right estimated values for the parameters. Therefore, it is favorable to develop a robust estimation scheme for this situation.

#### **6.2.5. Boundary Detection Of The Mixed 3-D Textures With Fractal Scale And Knowledge-Based Post-Cleaning Process**

The natural scene image does not contain a pure 2-D texture pattern which can be represented by the isotropically distributed random texture model, but a projected pattern on the 3-D surface. For example, in Figure 2.2 (tree image), the tree bark pattern around the boundary between the tree and the lawn ground looks more dense than the pattern in the middle of the tree. This makes it difficult to apply the conventional 2-D texture model to get the texture boundary the different textures. However, this 3-D texture boundary can be detected using fractal scaling parameter in fractional differencing model which has been proposed through this thesis because the fractal scale parameter is known to be a rotational and scaling invariant parameter and its value is considered as a measure of the roughness of surface. Thus, we can have the same value of the fractal scale within same 3-D texture pattern, and the higher value of the fractal scale around the texture boundary [46, 173]. Then, the fractal scale image can be generated by applying a proper size of window to the original image,

and the texture boundary can be obtained by thresholding the values of fractal scale in the fractal scale image. Also, this texture boundary image can be improved by deleting false boundaries, correcting wrong boundary directions, and linking the lost boundaries. This post-processing can be done by applying a knowledge-based reasoning process to the obtained boundary image. Here, a set of rules for knowledge-based algorithm can be constructed from the prior knowledge that the texture boundaries are continuous and closed. This boundary detection technique is being developed in detail.

## **LIST OF REFERENCES**

## LIST OF REFERENCES

- [1] Ahuja, N., "Mosaic Models for Images- I. Geometric Properties of Components in Cell-Structure Mosaics," *Information Science*, vol. 23, pp. 69-104, 1981.
- [2] Ahuja, N., "Mosaic Models for Images- II. Geometric Properties of Components in Coverage Mosaics," *Information Science*, vol. 23, pp. 159-200, 1981.
- [3] Ahuja, N., "Mosaic Models for Images- III. Spatial Correlation in Mosaics," *Information Science*, vol. 24, pp. 43-69, 1981.
- [4] Ahuja, N. and A. Rosenfeld, "Mosaic Models for Textures," *IEEE Trans. Pattern Analysis and Machine Intelligence*, vol. PAMI-3, pp. 1-11, Jan. 1981.
- [5] Ahuja, N., "Texture Analysis," in *Encyclopedia of Artificial Intelligence*, ed. L. G. Shapiro, pp. 1101-1115, Wiley & Sons, 1987.
- [6] Aloimonos, J. and M. J. Swain, "Shape from Texture," *Proc. International Joint Conference on Artificial Intelligence*, pp. 926-931, Los Angeles, CA, August 1985.
- [7] Aloimonos, J., "Visual Shape Computation," *Proc. IEEE*, vol. 76, no. 8, pp. 899-916, Aug. 1988.
- [8] Altschuler, M. D., Y. Censor, G. T. Herman, A. Lent, R. M. Lewitt, S. N. Srihari, H. Tuy, and J. K. Udupa, "Mathematical Aspects of Image Reconstruction From Projections," in *Progress in Pattern Recognition*, ed. A. Rosenfeld, pp. 323-375, North-Holland, 1981.
- [9] Bajcsy, R., "Active Perception," *Proc. IEEE*, vol. 76, no. 8, pp. 996-1005, Aug. 1988.
- [10] Ballard, D. H. and C. M. Brown, *Computer Vision*, Prentice Hall, 1982.
- [11] Ballard, D. H. and H. Tanaka, "Transformational Form Perception in 3D: Constraints, Algorithms, Implementation," *Proc. International Joint Conf. on Artificial Intelligence*, pp. 964-968, Los Angeles, CA, August 1985.

- [12] Barrow, H. G. and J. M. Tenenbaum, "Recovering Intrinsic Scene Characteristics From Images," in *Computer Vision Systems*, ed. A. R. Hanson, E. M. Riseman, pp. 3-26, Academic Press, 1978.
- [13] Bertero, M., T. A. Poggio, and V. Torre, "Ill-Posed Problems in Early Vision," *Proc. IEEE*, vol. 76, no. 8, pp. 869-889, Aug. 1988.
- [14] Besag, J., "On the Statistical Analysis of Dirty Pictures," *J. Royal Stat. Soc. B*, vol. 48, no. 3, pp. 259-302, 1986.
- [15] Besl, P. J., "Geometric Modeling and Computer Vision," *Proc. IEEE*, vol. 76, no. 8, pp. 936-958, Aug. 1988.
- [16] Bezdek, J. C., *Pattern Recognition with Fuzzy Objective Function Algorithms*, Plenum Press, 1981.
- [17] Bickel, P. J. and K. A. Doksum, *Mathematical Statistics*, Holden-Day Inc., 1977.
- [18] Bolle, R. M., D. B. Cooper, and B. Cernuschi-Frias, "Three Dimensional Surface Shape Recognition By Approximating Image Intensity Functions With Quadratic Polynomials," *Proc. IEEE PRIP*, pp. 611-617, 1982.
- [19] Bose, N. K., *Applied Multidimensional Systems Theory*, Van Nostrand Reinhold, 1982.
- [20] Bovick, A. C., T. S. Huang, and D. C. Munson Jr., "Generalization of Median Filtering Using Linear Combinations of Order Statistics," *IEEE Trans. Acoustics, Speech, and Signal Processing*, vol. ASSP-31, pp. 1342-1350, 1983.
- [21] Bovick, A. C., T. S. Huang, and D. C. Munson Jr., "Edge-Sensitive Image Restoration Using Order-Constrained Least Square Methods," *IEEE Trans. Acoustics, Speech, and Signal Processing*, vol. ASSP-33, pp. 1253-1263, 1985.
- [22] Bovik, A. C., "On Detecting Edges in Speckle Imagery," *IEEE Trans. Acoustics, Speech, and Signal Processing*, vol. 36, no. 10, pp. 1618-1627, Oct. 1988.
- [23] Box, G. E. P. and G. M. Jenkins, *Time Series Analysis: Forecasting and Control*, Holden-Day, 1969.
- [24] Bozma, H. I. and J. S. Duncan, "Admissibility of Constraint Functions in Relaxation Labeling," *Proc. 2nd International Conf. on Computer Vision*, pp. 328-332, Tampa, FL, Dec. 1988.
- [25] Brady, M., "Computational Approaches to Image Understanding," *ACM Computing Survey*, vol. 14, pp. 3-71, 1982.

- [26] Brillinger, D. R., "Fourier Analysis of Stationary Processes," *Proceedings of the IEEE*, vol. 62, no. 12, pp. -, Dec. 1974.
- [27] Brillinger, D. R., *Time Series, Data Analysis and Theory, Expanded Edition*, Holden Day Inc., 1981.
- [28] Brodatz, P., *Textures: A Photographic Album for Artists and Designers*, Dover Publication, New York, 1966.
- [29] Brodatz, P., P. Chan, and J. S. Lim, "One-Dimensional Processing for Adaptive Image Restoration," *IEEE Trans. Acoustics, Speech and Signal Processing*, vol. ASSP-33, pp. 117-126, Dover Publication, New York, 1985.
- [30] Broida, T. J. and R. Chellappa, "Performance Bounds for Estimating Three-dimensional Motion Parameters From A Sequence of Noisy Images," *J. of the Optical Society of America A*, vol. 6, no. 6, pp. 879-889, June 1989.
- [31] Brooks, M. J. and B. K. P. Horn, "Shape and Source From Shading," *Proc. International Joint Conference on Artificial Intelligence*, pp. 932-936, Los Angeles, CA, August 1985.
- [32] Bruckstein, A. M., "On Shape From Shading," *Computer Vision, Graphics, and Image Processing*, vol. 44, pp. 139-154, 1988.
- [33] Burt, P. J. and E. H. Adelson, "The Laplacian Pyramid as A Compact Image Code," *IEEE Trans. Communications*, vol. COM-31, pp. 532-540, Apr. 1983.
- [34] Burt, P. J., "The Pyramid as a Structure for Efficient Computation," in *Multiresolution Image Processing and Analysis*, ed. A. Rosenfeld, pp. 6-35, Springer-Verlag, New York, 1984.
- [35] Burt, P. J., "Smart Sensing Within A Pyramid Vision Machine," *Proc. IEEE*, vol. 76, no. 8, pp. 1006-1015, Aug. 1988.
- [36] Canny, J., "A Computational Approach To Edge Detection," *IEEE Trans. PAMI*, vol. PAMI-8, pp. 679-697, Nov. 1986.
- [37] Cernuschi-Frias, B., D. B. Cooper, and R. M. Bolle, "Estimation Of Location And Orientation Of 3-D Surface Using A Single 2-D Image," *Proc. IEEE PRIP*, pp. 605-610, 1982.
- [38] Chang, H. and K. Aggarwal, "Design of Two-Dimensional Recursive Filters By Interpolation," *IEEE Trans. Circuits and Systems*, vol. CAS-24, pp. 281-291, June 1977.
- [39] Charniak, E. and D. McDermott, *Intr. To Artificial Intelligence*, Addeson-Wesley, 1985.

- [40] Chaudhuri, B. B., "A Note on Fast Algorithm for Spatial Domain Techniques in Image Processing," *IEEE Trans. SMC*, vol. SMC-13, pp. 1166-1169, Nov./Dec. 1983.
- [41] Chellappa, R. and R. L. Kashyap, "Texture Synthesis Using Spatial Interaction Models," *Proc. of IEEE PRIP*, pp. 226-229, 1982.
- [42] Chellappa, R. and R. L. Kashyap, "Digital Image Restoration Using Spatial Interaction Models," *IEEE Trans. on Acoustics, Speech, and Signal Processing*, vol. ASSP-30, pp. 461-472, June 1982.
- [43] Chellappa, R., "Time Series Models for Multiresolution Images," in *Multiresolution Image Processing and Analysis*, ed. A. Rosenfeld, pp. 102-108, Springer-Verlag, New York, 1984.
- [44] Chellappa, R., "Two-Dimensional Discrete Gaussian Markov Random Field Models For Image Processing," in *Progress in Pattern Recognition 2*, ed. L. N. Kanal & A. Rosenfeld, pp. 79-112, North-Holland, 1985.
- [45] Chen, C-C and R. C. Dubes, "Experiments in Fitting Discrete Markov Random Fields to Textures," *Proc. IEEE Computer Society Conf. on CVPR*, pp. 298-303, June 1989.
- [46] Chen, C-C., J. S. Daponte, and M. D. Fox, "Fractal Feature Analysis and Classification in Medical Imaging," *IEEE Trans. Medical Imaging*, vol. 8, no. 2, pp. 133-142, June 1989.
- [47] Chen, S. S., J. M. Keller, and R. M. Crownover, "Shape from Fractal Geometry," *Artificial Intelligence*, vol. 43, pp. 199-218, 1990.
- [48] Chevalier, M. C., G. Chollet, and Y. Grenier, "Speech Analysis and Restitution Using Time-Dependent Autoregressive Models," *Proc. IEEE ICASSP-85*, pp. 501-504, 1985.
- [49] Choe, Yoonsik and R. L. Kashyap, "A 3-D Texture Model of Natural Scene Image," *Proceeding of The 22nd Asilomar Annual Conference on Signals, System & Computer*, pp. 463-467, Nov. 1988.
- [50] Choe, Yoonsik and R. L. Kashyap, "A Model and Synthesis of Texture on A 3-D Surface," *Proceeding of The 26th Annual Allerton Conf. on Communication, Control, and Computing*, pp. 647-656, Sept. 1988.
- [51] Cohen, F. S. and J-F P. Cayula, "3-D Object Recognition From A Single Image," *SPIE Intelligent Robots and Computer Vision*, vol. 521, pp. 7-15, 1984.

- [52] Cohen, F. S. and D. B. Cooper, "Simple Parallel Hierarchical And Relaxation Algorithms For Segmenting Noncausal Markovian Random Fields," *IEEE Trans. PAMI*, vol. PAMI-9, pp. 195-219, March 1987.
- [53] Cohen, F. S. and Zhigang Fan, "Rotation & Scale Invariant Texture Classification," *Proc. IEEE International Conf. on Robotics & Automation*, pp. 1394-1399, 1988.
- [54] Cohen, F. S. and M. S. Patel, "Rendering Texture On 3D Surfaces," *Proceeding of The 22nd Asilomar Annual Conference on Signals, System & Computer*, pp. -, Nov. 1988.
- [55] Cohen, P. and H. H. Nguyen, "Unsupervised Bayesian Estimation For Segmenting Textured Images," *Proc. 2nd International Conf. on Computer Vision*, pp. 303-309, Tampa, FL, Dec. 1988.
- [56] Cross, G. R. and A. K. Jain, "Markov Random Field Texture Models," *IEEE Trans. PAMI*, vol. PAMI-5, no. 1, pp. 25-39, Jan. 1983.
- [57] Crowley, James L., "A Computational Paradigm for Three Dimensional Scene Analysis," *Proc. of Workshop on Computer Vision*, pp. 170-177, 1984.
- [58] Das, M., M. J. Paulik, and N. K. Loh, "A Two-Dimensional Autoregressive Modeling Technique For Analysis And Classification Of Palmar Shapes," *Proceeding of The 26th Annual Allerton Conf. on Communication, Control, and Computing*, pp. 629-638, Sept. 1988.
- [59] Davis, L. S., L. Janos, and S. M. Dunn, "Efficient Recovery of Shape From Texture," *IEEE Trans. PAMI*, vol. PAMI-5, pp. 485-492, 1983.
- [60] Delp, E. J., R. L. Kashyap, and O. R. Mitchell, "Image Data Compression Using Autoregressive Time Series Models," *Pattern Recognition*, vol. 11, pp. 313-323, 1979.
- [61] Dubes, R. C. and A. K. Jain, "Random Field Models in Image Analysis," *J. Applied Statistics*, vol. 16, no. 2, pp. 131-164, 1989.
- [62] Duda, R. O. and P. E. Hart, *Pattern Classification and Scene Analysis*, John Wiley & Sons, 1973.
- [63] Dudgeon, D. E. and R. M. Mersereau, *Multidimensional Digital Signal Processing*, Prentice-Hall, 1984.
- [64] Eastman, R. D. and A. M. Waxman, "Using Disparity Functions For Stereo Correspondence And Surface Reconstruction," *Computer Vision, Graphics, and Image Processing*, vol. 39, pp. 73-101, 1987.

- [65] El-Gabali, M., M. Shridhar, and M. Ahmadi, "Segmentation of Noisy Images Modelled By Markov Random Fields With Gibbs Distribution," *Int. Conf. ASSP*, pp. 551-554, 1987.
- [66] Enab, Y. M. and J. Y. S. Luh, "Shape From A Single View Using Matching Method," *Pattern Recognition*, vol. 21, no. 4, pp. 313-318, 1988.
- [67] Eom, K-B., "Robust Image Models With Application," Ph.D Thesis, Purdue University, West Lafayette, Indiana, 1986.
- [68] Eom, K. and R. L. Kashyap, "Composite Edge Detection With Random Field Models," *Proc. Int. Conf. Computer Vision (ICCV '87)*, London, England, 1987.
- [69] Eom, K. and R. L. Kashyap, "Texture And Intensity Edge Detection With Random Field Models," *Proc. IEEE Workshop on Computer Vision*, pp. 29-34, 1987.
- [70] Eom, K. and R. L. Kashyap, "Robust Image Modelling Techniques With An Image Restoration Application," *IEEE Trans. Acoustics, Speech, and Signal Processing*, vol. ASSP-36, pp. 1313-1325, 1988.
- [71] Fan, Z. and F. S. Cohen, "Textured Image Segmentation as a Multiple Hypothesis Test," *IEEE Trans. Circuits and Systems*, vol. 35, no. 6, pp. 691-702, June 1988.
- [72] Faux, I. D. and M. J. Pratt, *Computational Geometry For Design And Manufacture*, Ellis Horwood Ltd., 1979.
- [73] Ferrie, F. P. and M. D. Levine, "Where and Why Local Shading Analysis Works," *IEEE Trans. Pattern Analysis and Machine Intelligence*, vol. PAMI-11, no. 2, pp. 198-206, Feb. 1989.
- [74] Forstner, W., "Reliability Analysis of Parameter Estimation in Linear Models with Applications to Mensuration Problems in Computer Vision," *Computer Vision, Graphics, And Image Processing*, vol. 40, pp. 273-310, 1987.
- [75] Frankot, R. T. and R. Chellappa, "An Improved Algorithm for The Shape From Shading Problem," *IISC*, Dec. 1986.
- [76] Frankot, R. T. and R. Chellappa, "A Method For Enforcing Integrability In Shape From Shading Algorithms," *University of Southern California, SIPI Report*, no. 105, 1987.
- [77] Frankot, R. T. and R. Chellappa, "Application of A Shape From Shading Technique To Synthetic Aperture Radar Imagery," *Int. Geoscience and Remote Sensing Symposium*, May 1987.

- [78] Frankot, R. T. and R. Chellappa, "A Method for Enforcing Integrability in Shape from Shading Algorithms," *IEEE Trans. Pattern Analysis and Machine Intelligence*, vol. 10, no. 4, pp. 439-451, July 1988.
- [79] Frankot, R. T. and R. Chellappa, "Estimation of Surface Topography from SAR Imagery Using Shape from Shading Techniques," *Artificial Intelligence*, vol. 43, pp. 271-310, 1990.
- [80] Fu, K. S. and J. K. Mui, "A Survey On Image Segmentation," *Pattern Recognition*, vol. 13, pp. 3-16, 1981.
- [81] Fukunaga, K., *Introduction To Statistical Pattern Recognition*, Academic Press, 1972.
- [82] Gagalowicz, A. and S. D. Ma, "A Model For Textures On 3-D Surfaces," *Proc. 4th Scandinavian Conf. on Image Analysis*, vol. 1, pp. 421-428, June 1985.
- [83] Gamble, E., D. Geiger, T. Poggio, and D. Weinshall, "Integration of Vision Modules and Labeling of Surface Discontinuities," *IEEE Trans. SMC*.
- [84] Geman, S. and C. Graffigne, "Markov Random Field Image Models and Their Applications to Computer Vision," *Proc. Int. Congress of Mathematicians*, pp. 1496-1517, 1986.
- [85] Geman, Stuart and Donald Geman, "Stochastic Relaxation, Gibbs Distributions, and The Bayesian Restoration Of Images," *IEEE Trans. PAMI*, vol. PAMI-6, no. 6, pp. 721-741, Nov. 1984.
- [86] Golub, G. H. and C. F. van Loan, *Matrix Computations*, The Johns Hopkins University Press, 1983.
- [87] Gonzalez, R. C. and P. Wintz, *Digital Image Processing*, Addison-Wesley, 1977.
- [88] Goutsias, J. and J. M. Mendel, "Semi-Markov Random Field Models For Image Segmentation," *Int. Conf. ASSP*, pp. 567-570, 1987.
- [89] Granger, C. V. J. and R. Joyeux, "An Introduction To Long-Memory Time Series Models And Fractional Differencing," *Journal of Time Series*, vol. 1, pp. 15-29, 1980.
- [90] Grenier, Y. and M-C. Chevalier, "Autoregressive Models with Time-Dependent Log Area Ratios," *IEEE Trans. Acoustics, Speech, and Signal Processing*, vol. 36, no. 10, pp. 1602-1612, Oct. 1988.

- [91] Greydon, I. R., "Interpolation Through Integration of Depth and Surface Orientation Maps," *Proc. 4th Scandinavian Conf. on Image Analysis*, vol. 2, pp. 769-776, June 1985.
- [92] Haralick, R. M., K. Shanmugam, and I. Dinstein, "Texture Features for Image Classification," *IEEE Trans. Systems, Man and Cybernetics*, vol. SMC-3, pp. 610-621, 1973.
- [93] Haralick, R. M., "Digital Step Edges From Zero Crossing Of Second Directional Derivatives," *IEEE Trans. PAMI*, vol. PAMI-6, pp. 58-68, Jan. 1984.
- [94] Haralick, R. M. and L. G. Shapiro, "Survey: Image Segmentation Techniques," *Computer Vision, Graphics, and Image Proc.*, vol. 29, pp. 100-132, 1985.
- [95] Haralick, R. M., "Monocular Vision Using Inverse Perspective Projection Geometry: Analytic Relations," *Proc. IEEE Computer Society Conf. on CVPR*, pp. 370-378, June 1989.
- [96] Haralick, Robert M., "Statistical Image Texture Analysis," in *Handbook of Pattern Recognition and Image Processing*, pp. 247-279, Academic Press, Inc., 1986.
- [97] Hartt, K. D., P. A. Kelly, and H. Derin, "The Modeling And Segmentation Of Speckled Images," *Int. Conf. ASSP*, pp. 559-562, 1987.
- [98] Hassner, M. and J. Sklansky, "The Use of Markov Random Fields as Models of Texture," *Computer Graphics And Image Processing*, vol. 12, pp. 357-370, 1980.
- [99] Horn, B. K. P., *Robot Vision*, McGraw-Hill, MIT Press, 1986.
- [100] Horn, B. K. P. and M. J. Brooks, "The Variational Approach to Shape From Shading," *Computer Vision, Graphics, And Image Processing*, vol. 33, pp. 174-128, 1986.
- [101] Hosking, J. R. M., "Fractional Differencing," *Biometrika*, vol. 68, pp. 165-176, 1981.
- [102] Huang, T. S., "Determining Three-Dimensional Motion And Structure From Two Perspective Views," in *Handbook of Pattern Recognition And Image Processing*, pp. 333-353, 1986.
- [103] Huber, P. J., *Robust Statistics*, John Wiley & Sons, Inc., 1981.

- [104] Ikeuchi, K. and B. K. P. Horn, "Numerical Shape From Shading and Occluding Boundaries," *Artificial Intelligence*, vol. 17, pp. 141-184, 1981.
- [105] Ikeuchi, K., "Shape From Regular Patterns," *Artificial Intelligence*, vol. 22, pp. 49-75, 1984.
- [106] Illingworth, J. and J. Kittler, "A Survey of the Hough Transform," *Computer Vision, Graphics, and Image Processing*, vol. 44, pp. 87-116, 1988.
- [107] Jain, A. K., *Fundamentals of Digital Image Processing*, Prentice-Hall, 1989.
- [108] Kanade, T., "Survey: Region Segmentation: Signal vs Semantics," *Computer Graphics and Image Processing*, vol. 13, pp. 279-297, 1980.
- [109] Kanatani, K-I and T-C Chou, "Shape from Texture: General Principle," *Artificial Intelligence*, vol. 38, pp. 1-48, 1989.
- [110] Kanatani, K., "Detection of Surface Orientation and Motion from Texture by a Stereological Technique," *Artificial Intelligence*, vol. 23, pp. 213-237, 1984.
- [111] Kang, H. and J. K. Aggarwal, "Design of Two-Dimensional Recursive Filters by Interpolation," *IEEE Trans. Circuit and Systems*, vol. CAS-24, pp. 281-291, 1977.
- [112] Kashyap, R. L. and A. R. Rao, *Dynamic Stochastic Models From Empirical Data*, Academic Press, 1976.
- [113] Kashyap, R. L., "Analysis and Synthesis of Image Patterns by Spatial Interaction Models," in *Progress in Pattern Recognition*, ed. A. Rosenfeld, pp. 149-186, North-Holland, 1981.
- [114] Kashyap, R. L., R. Chellappa, and N. Ahuja, "Decision Rules for Choice of Neighbors in Random Field Models of Images," *Computer Graphics And Image Processing*, vol. 15, pp. 301-318, 1981.
- [115] Kashyap, R. L., "Univariate and Multivariate Random Field Models for Images," in *Image Modeling*, ed. A. Rosenfeld, pp. 245-258, Academic Press, Inc, 1981.
- [116] Kashyap, R. L. and P. M. Lapsa, "Long-Correlation Models For Random Fields," *Proc. IEEE PRIP*, pp. 663-668, 1982.
- [117] Kashyap, R. L., "Optimal Choice of AR and MA Parts in Autoregressive Moving Average Models," *IEEE Trans. PAMI*, vol. PAMI-4, no. 2, pp. 99-104, March 1982.

- [118] Kashyap, R. L. and R. Chellappa, "Estimation and Choice of Neighbors in Spatial-Interaction Models of Images," *IEEE Trans. Information Theory*, vol. IT-29, no. 1, pp. 60-71, Jan. 1983.
- [119] Kashyap, R. L. and R. Chellappa, "Correction to 'Estimation and Choice of Neighbors in Spatial-Interaction Models of Images'," *IEEE Trans. Information Theory*, vol. IT-29, no. 4, p. 629, July 1983.
- [120] Kashyap, R. L. and A. Khotanzad, "A Stochastic Model Based Technique for Texture Segmentation," *Proc. Int. Conf. Pattern Recognition*, IEEE Computer Society Publication, Montreal, July-Aug. 1984.
- [121] Kashyap, R. L. and P. M. Lapsa, "Synthesis and Estimation of Random Fields Using Long-Correlation Models," *IEEE Trans. PAMI*, vol. PAMI-6, pp. 800-809, Nov. 1984.
- [122] Kashyap, R. L., "Characterization and Estimation of Two-Dimensional ARMA Models," *IEEE Trans. Information Theory*, vol. IT-30, no. 5, pp. 736-745, Sept. 1984.
- [123] Kashyap, R. L. and K-B Eom, "Texture Boundary Detection Based On Long Correlation Model," *Proc. IEEE Int. Conf. Geoscience and Remote Sensing Symposium*, p. 255, Amhurst, MA, 1985.
- [124] Kashyap, R. L. and K-B Eom, "Texture Boundary Detection Based On Long Correlation Model," *Proc. The 23rd Annual Allerton Conference on Control, Communication, and Computers*, pp. 314-323, Oct. 1985.
- [125] Kashyap, R. L., "Image Models," in *Handbook of Pattern Recognition and Image Processing*, pp. 281-310, Academic Press, Inc, 1986.
- [126] Kashyap, R. L. and A. Khotanzad, "A Model-Based Method for Rotation Invariant Texture Classification," *IEEE Trans. PAMI*, vol. PAMI-8, pp. 472-481, 1986.
- [127] Kashyap, R. L. and K-B Eom, "Estimation In Long-Memory Time-Series Model," *Journal of Time Series Analysis*, vol. 9, pp. 35-41, 1988.
- [128] Kashyap, R. L. and K-B Eom, "Robust Image Models and Their Application," in *Advances In Electronics And Electron Physics*, vol. 70, pp. 79-157, 1988.
- [129] Kashyap, R. L. and K.-B. Eom, "Texture Boundary Detection Based on the Long Correlation Model," *IEEE Trans. Pattern Analysis and Machine Intelligence*, vol. PAMI-11, no. 1, pp. 58-67, Jan. 1989.
- [130] Kass, M. and A. Witkin, "Analyzing Oriented Patterns," *Computer Vision, Graphics, And Image Processing*, vol. 37, pp. 362-385, 1987.

- [131] Kassam, S. A. and H. V. Poor, "Robust Techniques for Signal Processing: Survey," *Proceedings of IEEE*, vol. 73, pp. 433-481, 1985.
- [132] Keller, J. M., R. M. Crownover, and R. Y. Chen, "Characteristics of Natural Scenes Related to The Fractal Dimension," *IEEE Trans. PAMI*, vol. PAMI-9, pp. 621-627, Sept. 1987.
- [133] Keller, J. M., S. Chen, and R. M. Crownover, "Texture Description and Segmentation through Fractal Geometry," *Computer Vision, Graphics, and Image Processing*, vol. 45, pp. 150-166, Feb. 1989.
- [134] Kelly, P. A., H. Derin, and K. D. Hartt, "Adaptive Segmentation of Speckled Images Using a Hierarchical Random Field Model," *IEEE Trans. Acoustics, Speech, and Signal Processing*, vol. 36, no. 10, pp. 1628-1641, Oct. 1988.
- [135] Kender, J. R., "Shape From Texture: An Aggregation Transform That Maps A Class Of Textures Into Surface Orientation," *Proc. 6th IJCAI*, pp. 475-480, 1979.
- [136] Kender, J. R., "A Computational Paradigm For Deriving Local Surface Orientation From Local Texture Properties," *Proc. IEEE Workshops on Computer Vision; Representation and Control*, pp. 143-152, 1982.
- [137] Kitagawa, G., "A Nonstationary Time Series Model And Its Fitting By A Recursive Filter," *Journal of Time Series Analysis*, vol. 2, no. 2, pp. 103-117, 1981.
- [138] Koch, M. W. and R. L. Kashyap, "Matching Polygon Fragments," *Pattern Recognition Letters*, no. 10, pp. 297-308, Nov. 1989.
- [139] Kube, P., "Likely Local Shape," *Proc. IEEE Computer Society Conf. on CVPR*, pp. 529-534, June 1989.
- [140] Kung, S-Y, B. C. Levy, M. Morf, and T. Kailath, "New Results in 2-D Systems Theory, Part II: 2-D State-Space Models- Realization and the Notions of Controllability, Observability, and Minimality," *Proc. IEEE*, vol. 65, no. 6, pp. 945-961, June 1977.
- [141] Laarhoven, P. J. M. van and E. H. L. Aarts, *Simulated Annealing: Theory and Applications*, Kluwer Academic, 1987.
- [142] Laffey, T. J., R. M. Haralick, and L. T. Watson, "Topographic Classification Of Digital Image Intensity Surface," *Proc. IEEE Workshop on Computer Vision; Representation and Control*, pp. 171-177, 1982.
- [143] Lawrance, A. J. and N. T. Kottegoda, "Stochastic Modelling of Riverflow Time Series," *J. R. Statist. Soc. A*, vol. 140, pp. 1-47, 1977.

- [144] Lee, C-H and A. Rosenfeld, "Improved Methods of Estimating Shape from Shading Using the Light Source Coordinate System," *Artificial Intelligence*, vol. 26, pp. 125-143, 1985.
- [145] Lee, D., "Some Computational Aspects of Low-Level Computer Vision," *Proc. IEEE*, vol. 76, no. 8, pp. 890-898, Aug. 1988.
- [146] Lee, H. C. and K. S. Fu, "3D Shape From Contour And Selective Confirmation," *Proc. IEEE Workshop on Computer Vision; Representation and Control*, pp. 162-170, 1982.
- [147] Lee, H. C. and K. S. Fu, "A Computer Vision System For Generating Object Description," *Proc. IEEE PRIP*, pp. 466-472, 1982.
- [148] Li, H., "Maximum Entropy Spectrum Estimation With Imprecise Autocorrelation Function Lags By Fuzzy Set Theory," *International Conf. on ASSP*, pp. 2396-2399, Apr. 88.
- [149] Lowe, D. g., "Three-Dimensional Object Recognition from Single Two-Dimensional Images," *Artificial Intelligence*, vol. 31, pp. 355-395, 1987.
- [150] Makhoul, J., "Linear Prediction: A Tutorial Review," *Proceedings of The IEEE*, vol. 63, pp. 561-580, Apr. 1975.
- [151] Mandelbrot, B. B. and J. W. Van Ness, "Fractional Brownian Motions, Fractional Noises and Applications," *SIAM Rev.*, vol. 10, pp. 422-437, 1968.
- [152] Manjunath, B. S., T. Simchony, and R. Chellappa, "Stochastic and Deterministic Networks for Texture Segmentation," USC-SIPI Report No.132, University of Southern California, Los Angeles, CA.
- [153] Manjunath, B. S. and R. Chellappa, "Stochastic Learning Networks for Texture Segmentation," *Proceeding of The 22nd Asilomar Annual Conference on Signals, System & Computer*, pp. -, Nov. 1988.
- [154] Marr, D. and E. Hildreth, "Theory of Edge Detection," *Proc. R. Soc. London. Series B*, vol. 207, pp. 187-217, 1980.
- [155] Marr, D., *Vision*, W. H. Freeman and Co., San Francisco, 1982.
- [156] Moerdler, M. L. and J. R. Kender, "An Integrated System That Unifies Multiple Shape From Texture Algorithms," *Proc. Conf. American Association for Artificial Intelligence*, pp. 723-727, Seattle, July 1987.
- [157] Moerdler, M. L., "Multiple Shape-From-Texture Into Texture Analysis and Surface Segmentation," *Proc. 2nd Internation Conf. on Computer Vision*, pp. 316-320, Tempa, FL, Dec. 1988.

- [158] Morf, M., B. C. Levy, and S-Y Kung, "New Results in 2-D Systems Theory, Part I: 2-D Polynomial Matrices, Factorization, and Coprimeness," *Proc. IEEE*, vol. 65, no. 6, pp. 861-872, June 1977.
- [159] Mortenson, M. E., *Geometric Modeling*, John Wiley & Sons, 1985.
- [160] Mulgaonkar, P. G., L. G. Shapiro, and R. M. Haralick, "Recognizing Three-Dimensional Objects From Single Perspective Views Using Geometric And Relational Reasoning," *Proc. IEEE PRIP*, pp. 479-484, 1982.
- [161] Nasburg, R. E. and R. L. Kashyap, "Robust Parameter Estimation in Dynamic System," *Proc. Information Science and Systems Conf.*, Johns Hopkins University, 1975.
- [162] Netravali, A. N. and B. Prasada, *Visual Communications Systems*, IEEE Press, 1988.
- [163] Pao, Y-H., *Adaptive Pattern Recognition and Neural Networks*, Addison Wesley, 1989.
- [164] Papoulis, A., *Probability, Random Variables, and Stochastic Process*, McGraw-Hill, 1984.
- [165] Pappas, T. N. and N. S. Jayant, "An Adaptive Clustering Algorithm for Image Segmentation," *Proc. 2nd Internation Conf. on Computer Vision*, pp. 310-315, Tempa, FL, Dec. 1988.
- [166] Pavlidis, T., "Algorithms for Shape Analysis of Contours and Waveforms," *IEEE Trans. PAMI*, vol. PAMI-2, no. 4, pp. 301-312, July 1980.
- [167] Pentland, A., "Shape Information From Shading: A Theory About Human Perception," *Proc. 2nd Internation Conf. on Computer Vision*, pp. 404-413, Tempa, FL, Dec. 1988.
- [168] Pentland, A., "Automatic Extraction of Deformable Part Models," Vision Sciences Technical Report 104, M.I.T. Media Lab., July 1988.
- [169] Pentland, A., "The Transform Method for Shape From Shading," Vision Sciences Technical Report 106, M.I.T. Media Lab., July 1988.
- [170] Pentland, A. P., "Local Analysis of The Image Limitations and Uses of Shading," *Proc. IEEE Workshop on Computer Vision; Representation and Control*, pp. 153-161, 1982.
- [171] Pentland, A. P., "Finding The Illumination Direction," *J. Opt. Soc. Am*, vol. 72, pp. 448-455, Apr. 1982.

- [172] Pentland, A. P., "Local Shading Analysis," *IEEE Trans. PAMI*, vol. PAMI-6, pp. 170-187, Mar. 1984.
- [173] Pentland, A. P., "Fractal-Based Description of Natural Scenes," *IEEE Trans. PAMI*, vol. PAMI-6, pp. 661-674, Nov. 1984.
- [174] Pentland, A. P., *From Pixels To Predicates: Recent Advances in Computational and Robotic Vision*, Ablex Publication Co., Norwood, NJ, 1986.
- [175] Pentland, A. P., "Perceptual Organization and The Representation of Natural Form," *Artificial Intelligence*, vol. 28, pp. 293-331, 1986.
- [176] Pentland, A. P., "Shading Into Texture," *Artificial Intelligence*, vol. 29, pp. 147-170, 1986.
- [177] Perry, A. and D. G. Lowe, "Segmentation of Textured Images," *Proc. IEEE Computer Society Conf. on CVPR*, pp. 319-325, June 1989.
- [178] Poggio, T., "Computer Vision," *SPIE Image Pattern Recognition: Algorithm Implementations, Techniques, and Technology*, vol. 755, pp. 54-62, 1987.
- [179] Pong, T-C., R. M. Haralick, and L. G. Shapiro, "The Facet Approach to Shape From Shading," *Proc. of Workshop on Computer Vision*, pp. 143-149, 1984.
- [180] Poulo, R. J., "New Invariants For Three Dimensional Recognition," *Proc. Workshop on Computer Vision*, pp. 158-163, 1984.
- [181] Pratt, W. K., *Digital Image Processing*, John Wiley & Sons, Inc., 1978.
- [182] Rao, A. R. and B. G. Schunck, "Computing Oriented Texture Fields," *Proc. IEEE Computer Society Conf. on CVPR*, pp. 61-68, June 1989.
- [183] Rey, W. J. J., *Introduction to Robust and Quasi-Robust Statistical Methods*, Springer-Verlag, New York, 1983.
- [184] Riseman, E. M. and M. A. Arbib, "Survey: Computational Techniques in the Visual Segmentation of Static Scenes," *Computer Graphics and Image Processing*, vol. 6, pp. 221-276, 1977.
- [185] Robinson, G. S., "Edge Detection By compass Gradient Masks," *Computer Vision, Graphics, and Image Processing*, vol. 6, pp. 492-501, 1977.
- [186] Roesser, R. P., "A Discrete State-Space Model for Linear Image Processing," *IEEE Trans. Automatic Control*, vol. AC-20, no. 1, pp. 1-10, Feb. 1975.
- [187] Ron, G. and S. Peleg, "Multiresolution Shape From Shading," *Proc. IEEE Computer Society Conf. on CVPR*, pp. 350-355, June 1989.

- [188] Rosenfeld, A. and A. Kak, *Digital Picture Processing, Second Edition*, 1 & 2, Academic Press, 1982.
- [189] Rosenfeld, A., "Parallel Image Processing Using Cellular Arrays," *Computer*, pp. 14-20, 1983.
- [190] Rosenfeld, A., "Computer Vision: Basic Principles," *Proc. IEEE*, vol. 76, no. 8, pp. 863-868, Aug. 1988.
- [191] Rosenfeld, Azriel, "Computer Vision," in *Handbook of Pattern Recognition and Image Processing*, pp. 355-368, Academic Press, Inc, 1986.
- [192] Roux, J. Le, "2D Spectral Factorization and Stability Test for 2D Matrix Polynominals Based On The Radon Projection," *Proc. Int. Conf. ASSP*, pp. 1041-1044, Tokyo, 1986.
- [193] Roux, J. Le, "Some Properties of The Lattice Algorithm For The Direct Computation of The Matrical Spectral Factor," *Proc. Int. Conf. ASSP*, pp. 2731-2734, Tokyo, 1986.
- [194] Sanz, J. L. C., E. B. Hinkle, and A. K. Jain, *Radon and Projection Transform-Based Computer Vision*, Springer-Verlag, 1988.
- [195] Schalkoff, R. J., *Digital Image Processing and Computer Vision*, John Wiley & Sons, 1989.
- [196] Shao, M., T. Simchony, and R. Chellappa, "New Algorithms for Reconstruction of A 3-D Depth Map from One or More Images," *Proc. Computer Vision and Pattern Recognition*, pp. 530-535, June 1988.
- [197] Shapiro, L. G., "Recent Progress in Shape Decomposition and Analysis," in *Progress in Pattern Recognition 2*, ed. L. N. Kanal & A. Rosenfeld, pp. 113-123, North-Holland, 1985.
- [198] Sharma, G. and R. Chellappa, "A Model-Based Approach for Estimation of Two-Dimensional Maximum Entropy Power Spectra," *IEEE Trans. Information Theory*, vol. IT-31, no. 1, pp. 90-99, Jan. 1983.
- [199] Sharma, G. and R. Chellappa, "Two-Dimensional Spectrum Estimation Using Noncausal Autoregressive Models," *IEEE Trans. Information Theory*, vol. IT-32, no. 2, pp. 268-275, Mar. 1986.
- [200] Shirai, Y., *Three-Dimensional Computer Vision*, Springer-Verlag, 1987.
- [201] Silverman, J. F. and D. B. Cooper, "Bayesian Clustering for Unsupervised Estimation of Surface and Texture Models," *IEEE Trans. Pattern Analysis and Machine Intelligence*, vol. 10, no. 4, pp. 482-495, July 1988.

- [202] Simchony, T. and R. Chellappa, "Direct Analysis Methods for Solving Poisson Equations in Computer Vision Problems," *University of Southern California SIPI Report*, no. 110, July 1987.
- [203] Simchony, T., R. Chellappa, and Z. Lichtenstein, "Graduated Nonconvexity Algorithm for Image Estimation Using Compound Gauss Markov Field Models," *Univ. of Southern California-SIPI Report*, no. 128, 1988.
- [204] Simchony, T., R. Chellappa, H. Jinchi, and Z. Lichtenstein, "Pyramid Implementation of Optimal Step Conjugate Search Algorithms for Some Computer Vision Problems," *Univ. of Southern California-SIPI Report*, no. 126, 1988.
- [205] Solo, V., "Modeling of Two-Dimensional Random Fields by Parametric Cepstrum," *IEEE Trans. Information Theory*, vol. IT-32, no. 6, pp. 743-750, Nov. 1986.
- [206] Stevens, K. A., "The Visual Interpretation Of Surface Contours," *Artificial Intelligence*, vol. 17, pp. 47-73, 1981.
- [207] Stevens, K. A., "Inferring Shape from Contours Across Surfaces," in *From Pixels to Predicates*, ed. A. Pentland, pp. 93-110, Ablex Publishing Corp., 1986.
- [208] Strat, T. M. and M. A. Fischler, "One-Eyed Stereo: A General Approach to Modeling 3-D Scene Geometry," *IEEE Trans. Pattern Analysis and Machine Intelligence*, vol. 8, no. 6, pp. 730-741, Nov. 1986.
- [209] Tan, H. L., S. B. Gelfand, and E. J. Delp, "A Cost Minimization Approach To Edge Detection Using Simulated Annealing," *Proc. IEEE Computer Society Conf. on CVPR*, pp. 86-91, June 1989.
- [210] Tenenbaum, J. M., M. A. Fischler, and H. G. Barrow, "Scene Modeling: A Structural Basis for Image Description," *Computer Graphics And Image Processing*, vol. 12, pp. 407-425, 1980.
- [211] Terzopoulos, D., "Integrating Visual Information from Multiple Sources," in *From Pixels to Predicates*, ed. A. Pentland, pp. 111-142, Ablex Publishing Corp., 1986.
- [212] Terzopoulos, D., "Image Analysis Using Multigrid Relaxation Methods," *IEEE Trans. Pattern Analysis and Machine Intell.*, vol. PAMI-8, no. 2, pp. 129-139, Mar. 1986.
- [213] Terzopoulos, D., "Visual Depth Map," in *Encyclopedia of Artificial Intelligence*, ed. L. G. Shapiro, pp. 1152-1160, Wiley & Sons, 1987.

- [214] Terzopoulos, D., A. Witkin, and M. Kass, "Constraints on Deformable Models: Recovering 3D Shape and Nonrigid Motion," *Artificial Intelligence*, vol. 36, pp. 91-123, 1988.
- [215] Terzopoulos, D., "The Computation of Visible-Surface Representations," *IEEE Trans. Pattern Analysis and Machine Intelligence*, vol. 10, no. 4, pp. 417-438, July 1988.
- [216] Vilnrotter, F. M., R. Nevatia, and K. E. Price, "Structural Analysis of Natural Textures," *IEEE Trans. Pattern Analysis and Machine Intelligence*, vol. 8, no. 1, pp. 76-89, Jan. 1986.
- [217] Weiss, I., "3-D Shape Representation By Contours," *Proc. International Joint Conf. on Artificial Intelligence*, pp. 969-972, Los Angeles, CA, August 1985.
- [218] Weiss, I., "3D Shape Representation By Contours," *Computer Vision, Graphics, And Image Processing*, vol. 41, pp. 80-100, 1988.
- [219] Wilson, H. R. and J. R. Bergen, "A Four Mechanism Model For Threshold Spatial Vision," *Vision Research*, pp. 19-32, 1979.
- [220] Wilson, R. and M. Spann, *Image Segmentation and Uncertainty*, John Wiley & Sons, Research Studies Press, 1988.
- [221] Witkin, A. P., "Recovering Surface Shape and Orientation From Texture," *Artificial Intelligence*, vol. 17, pp. 17-45, 1981.
- [222] Witkin, A. P., "Scale Space Filtering," in *From Pixels to Predicates*, ed. A. Pentland, pp. 5-19, Ablex Publishing Corp., 1986.
- [223] Won, C. S. and H. Derin, "Segmentation Of Noisy Textured Images Using Simulated Annealing," *Int. Conf. ASSP*, pp. 563-566, 1987.
- [224] Wu, Z., "Multidimensional State-Space Model Kalman Filtering with Application to Image Restoration," *IEEE Trans. Acoustics, Speech, and Signal Processing*, vol. ASSP-33, pp. 1576-1592, 1985.
- [225] Yasuoka, Y. and R. M. Haralick, "Peak Noise Removal By A Facet Model," *Pattern Recognition*, vol. 16, pp. 3-29, 1983.
- [226] Zheng, Q. and R. Chelappa, *A Robust Algorithm For Inferring Shape From A Single Image*, To be published in 1990.
- [227] Zhou, Y., R. Chellappa, and V. Venkateswar, "Edge Detection Using Zero Crossings of Directional Derivatives of A Random Field Model," *Int. Conf. ASSP*, pp. 1465-1468, 1986.

- [228] Zhou, Y. and R. Chellappa, "Linear Feature Extraction Based On A AR Model Edge Detector," *Int. Conf. ASSP*, pp. 555-558, 1987.
- [229] Zhou, Y. T., V. Venkateswar, and R. Chellappa, "Edge Detection and Linear Feature Extraction Using a 2-D Random Field Model," *IEEE Trans. Pattern Analysis and Machine Intelligence*, vol. PAMI-11, no. 1, pp. 84-95, Jan. 1989.
- [230] Zucker, S. W., "Survey: Region Growing: Childhood and Adolescence," *Computer Graphics and Image Processing*, vol. 5, pp. 382-399, 1976.
- [231] Zucker, S. W., "Early Vision," in *Encyclopidia of Artificial Intelligence*, ed. L. G. Shapiro, pp. 1131-1152, Wiley & Sons, 1987.
- [232] Zuniga, O. A. and R. M. Haralick, "Integrated Directional Derivative Gradient Operator," *IEEE Trans. Systems, Man, And Cybernetics*, vol. SMC-17, pp. 508-517, May/June 1987.

## APPENDICES

## Appendix A

### Proof of Theorem 2.1

Intensity function  $x(l_1, l_2)$  can be represented by the following equation.

$$x(l_1, l_2) = \lambda\mu(\mathbf{L} \cdot \mathbf{N}) \quad (\text{A.1})$$

where,  $\lambda\mu$ : albedo (constant for the reflectance)

$\mathbf{L}$ : the illumination direction vector

$\mathbf{N}$ : the surface normal vector

Thus, when  $(l_1, l_2)$  defines the image plane from the viewing direction, the first derivative of image intensity in the direction  $(dl_1, dl_2)$ ,  $dx(l_1, l_2)$  is

$$dx = \lambda\mu(d\mathbf{L} \cdot \mathbf{N} + \mathbf{L} \cdot d\mathbf{N}) \quad (\text{A.2})$$

Assuming  $\mathbf{L}$  is constant,

$$dx = \lambda\mu(\mathbf{L} \cdot d\mathbf{N}) \quad (\text{A.3})$$

Notice that  $d\mathbf{N}$ , the change in  $\mathbf{N}$ , is perpendicular to  $\mathbf{N}$  as it lies in the tangent plane to  $\mathbf{N}$ , and isotropically distributed as same as  $\mathbf{N}$  is. Thus

$$E \left( \sum_{l_1, l_2} d\mathbf{N} \right) = 0 \quad (\text{A.4})$$

and

$$E(dx) = \lambda\mu(\mathbf{L} \cdot E(d\mathbf{N})) \quad (\text{A.5})$$

$$\approx \lambda\mu(L_{l_1} d\hat{N}_{l_1} + L_{l_2} d\hat{N}_{l_2} + L_{l_3} d\hat{N}_{l_3}) \quad (\text{A.6})$$

where  $(d\hat{N}_{l_1}, d\hat{N}_{l_2}, d\hat{N}_{l_3})$  are the average values of change in the surface normal in image direction  $(dl_1, dl_2)$  and  $\mathbf{L}=(L_{l_1}, L_{l_2}, L_{l_3})$  is the illumination direction. That is,

$$d\hat{N}_{l_1} = \frac{1}{n} \sum^n dN_{l_1}, \quad d\hat{N}_{l_2} = \frac{1}{n} \sum^n dN_{l_2} \quad (\text{A.7})$$

Since  $d\hat{N}_{l_3} = 0$ ,

$$E(dx) \approx \lambda\mu(L_{l_1} d\hat{N}_{l_1} + L_{l_2} d\hat{N}_{l_2}) \quad (\text{A.8})$$

Then, introducing  $dr$ , which may be thought of as the expected magnitude of  $dN$ , that is, as  $E(|dN|)$ ,

$$d\hat{N}_{l_1} = l_1 dr, \quad d\hat{N}_{l_2} = l_2 dr \quad (\text{A.9})$$

where  $l_1^2 + l_2^2 = 1$  and  $l_1/l_2 = d\hat{N}_{l_1}/d\hat{N}_{l_2} = dx_{l_1}/dx_{l_2}$ , defining  $(dx_{l_1}, dx_{l_2})$  to be the differential step in the image along which  $dx$  was measured.

Thus, defining  $\hat{L}_{l_1} = \lambda\mu L_{l_1} dr$  and  $\hat{L}_{l_2} = \lambda\mu L_{l_2} dr$ , we can have the following linear regression model, from (A.7), (A.8) and (A.9).

$$\begin{bmatrix} \hat{dx}_1 \\ \hat{dx}_2 \\ \vdots \\ \hat{dx}_n \end{bmatrix} = \begin{bmatrix} dl_{11} & dl_{21} \\ dl_{12} & dl_{22} \\ \vdots & \vdots \\ dl_{1n} & dl_{2n} \end{bmatrix} \begin{bmatrix} \hat{L}_{l_1} \\ \hat{L}_{l_2} \end{bmatrix} \quad (\text{A.10})$$

where  $\hat{dx}_i$  is the average value of  $dx$  over the  $i$ -th patch in direction  $(dl_{1i}, dl_{2i})$ .

■

## Appendix B

### Proof of Theorem 2.2

If we denote the matrix of directions  $(dl_{1i}, dl_{2i})$  by  $\beta$ , and let  $\beta^T$  indicate the transpose of  $\beta$ , then the solution (A.10) in Appendix A is the following least-square estimator.

$$\begin{bmatrix} \hat{L}_{l_1} \\ \hat{L}_{l_2} \end{bmatrix} = (\beta^T \beta)^{-1} \beta^T \begin{bmatrix} \hat{dx}_1 \\ \hat{dx}_2 \\ \vdots \\ \hat{dx}_n \end{bmatrix} \quad (\text{B.1})$$

Here, notice that the above solution is a normalized one. Thus, in order to get the actual values of  $(L_{l_1}, L_{l_2}, L_{l_3})$ , we need to calculate the value of  $\lambda \mu dr$  properly.

$$E(dx^2) = E(\lambda^2 \mu^2 (L_{l_1} dN_{l_1} + L_{l_2} dN_{l_2} + L_{l_3} dN_{l_3})^2) \quad (\text{B.2})$$

$$\begin{aligned} &\approx \lambda^2 \mu^2 (L_{l_1}^2 d\hat{N}_{l_1}^2 + L_{l_2}^2 d\hat{N}_{l_2}^2 + L_{l_3}^2 d\hat{N}_{l_3}^2 + 2L_{l_1} L_{l_2} d\hat{N}_{l_1} d\hat{N}_{l_2} \\ &\quad + 2L_{l_1} L_{l_3} d\hat{N}_{l_1} d\hat{N}_{l_3} + 2L_{l_2} L_{l_3} d\hat{N}_{l_2} d\hat{N}_{l_3}) \end{aligned} \quad (\text{B.3})$$

where  $(d\hat{N}_{l_1}, d\hat{N}_{l_2}, d\hat{N}_{l_3})$  are the average values of  $(dN_{l_1}, dN_{l_2}, dN_{l_3})$ .

Since  $\text{Var}(dN_{l_1}) = \text{Var}(dN_{l_2}) = dr^2$  for sphere model,  $d\hat{N}_{l_1}^2 = l_1^2 dr^2 + dr^2$ ,  $d\hat{N}_{l_2}^2 = l_2^2 dr^2 + dr^2$ , and  $d\hat{N}_{l_3} = dr^2$ ,

$$\begin{aligned} E(dx^2) &\approx \lambda^2 \mu^2 (L_{l_1}^2 (l_1^2 dr^2 + dr^2) + L_{l_2}^2 (l_2^2 dr^2 + dr^2) \\ &\quad + L_{l_3}^2 dr^2 + 2L_{l_1} L_{l_2} l_1 l_2 dr^2) \end{aligned} \quad (\text{B.4})$$

$$\approx \lambda^2 \mu^2 ((l_1 L_{l_1} + l_2 L_{l_2})^2 dr^2 + (L_{l_1}^2 + L_{l_2}^2 + L_{l_3}^2) dr^2) \quad (\text{B.5})$$

If the illumination direction vector  $\mathbf{L}$  is counted as a unit vector, that is,  $L_{l_1}^2 + L_{l_2}^2 + L_{l_3}^2 = 1$ ,

$$E(dx^2) \approx \lambda^2 \mu^2 ((l_1 L_{l_1} + l_2 L_{l_2})^2 dr^2 + dr^2) \quad (\text{B.6})$$

Also, from (2.2.1.1.7), (2.2.1.1.8), and (2.2.1.1.9),

$$\begin{aligned} E(dx)^2 &\approx (\lambda \mu (d\hat{N}_{l_1} L_{l_1} + d\hat{N}_{l_2} L_{l_2}))^2 \\ &\approx (\lambda \mu (l_1 L_{l_1} + l_2 L_{l_2}) dr)^2 \\ &\approx \lambda^2 \mu^2 (l_1 L_{l_1} + l_2 L_{l_2})^2 dr^2 \end{aligned} \quad (\text{B.7})$$

Thus,

$$E(dx^2) - E(dx)^2 \approx \lambda^2 \mu^2 dr^2 \triangleq k^2 \quad (\text{B.8})$$

Therefore, from the definitions of  $\hat{L}_{l_1}$ ,  $\hat{L}_{l_2}$ , and the equation  $L_{l_1}^2 + L_{l_2}^2 + L_{l_3}^2 = 1$ , the illumination direction can be calculated as follows.

$$L_{l_1} = \frac{\hat{L}_{l_1}}{k}, \quad L_{l_2} = \frac{\hat{L}_{l_2}}{k}, \quad L_{l_3} = \sqrt{1 - L_{l_1}^2 - L_{l_2}^2} \quad (\text{B.9})$$

And, from the relation between the  $x$ - $y$ - $z$  coordinate system and the angular coordinate system, we can represent the illumination direction with its tilt and slant angles,  $\tau_L$ ,  $\sigma_L$ . Thus,

$$\tau_L = \tan^{-1} \left( \frac{\hat{L}_{l_2}}{\hat{L}_{l_1}} \right), \quad \sigma_L = \cos^{-1} L_{l_3} \quad (\text{B.10})$$

■

## Appendix C

### Proof of Theorem 2.3

Let  $\sigma_L$  be the phase angle between the viewing direction  $\mathbf{V}$  and the illumination direction  $\mathbf{L}$ ,  $\psi$  be the incident angle between the illumination direction and the surface normal direction, and  $\eta$  be the emittance angle between the viewing direction and the surface normal direction. Then

$$\mathbf{V} \cdot \mathbf{L} = \cos \sigma_L, \quad \mathbf{L} \cdot \mathbf{N} = \cos \psi, \quad \text{and} \quad \mathbf{V} \cdot \mathbf{N} = \cos \eta \quad (\text{C.1})$$

Intensity function  $x(l_1, l_2)$  can be represented by the following equation.

$$x(l_1, l_2) = \lambda \mu (\mathbf{L} \cdot \mathbf{N}) = \lambda \mu \cos \psi, \quad \text{when } \cos \psi \geq 0. \quad (\text{C.2})$$

Then, for each of surface patches, to determine the expected value of image intensity, we need to average  $x(l_1, l_2)$ , and, to determine the expected value of image intensity squared, we need to average  $x^2(l_1, l_2)$  over the image of a hemisphere.

Notice that since not all of the hemisphere is illuminated, we should integrate only over the illuminated region, to avoid areas where  $\cos \psi$  is negative. A suitable spherical coordinate system can be erected with the equator in the plane containing  $\mathbf{L}$  and  $\mathbf{V}$ , with the pole at right angles to this plane, namely at  $\mathbf{O}$ , defined to be a unit vector orthogonal to the plane containing  $\mathbf{L}$  and  $\mathbf{V}$ . Let latitude be  $\tau$  measured from the equator, while longitude is  $\sigma$ , measured along the equator from the point  $\mathbf{V}$  toward  $\mathbf{L}$ . Therefore, the point  $\mathbf{L}$  has longitude  $\sigma_L$  and zero latitude. Simple spherical trigonometry using a triangle with corners  $\mathbf{V}$ ,  $\mathbf{N}$ , and  $\mathbf{O}$ , yields

$$\cos \eta = \cos \tau \cos \sigma \quad (\text{C.3})$$

and from a similar triangle with corners  $\mathbf{L}$ ,  $\mathbf{N}$ , and  $\mathbf{O}$ , we can obtain

$$\cos\psi = \cos\tau \cos(\sigma - \sigma_L) \quad (\text{C.4})$$

The illuminated half of the sphere runs from  $\sigma = -\pi/2 + \sigma_L$  to  $\sigma = +\pi/2 + \sigma_L$ , while the visible half goes from  $\sigma = -\pi/2$  to  $\sigma = +\pi/2$  and the infinitesimal element of area is  $\cos\tau d\sigma d\tau$ .

The integrals that we are interested in are of the form

$$\int_{-\pi/2}^{\pi/2} \int_{-\pi/2 + \sigma_L}^{\pi/2} f(\sigma, \tau) \cos\eta \cos\tau d\sigma d\tau \quad (\text{C.5})$$

where the  $\cos\eta$  term compensates for the foreshortening due to the projection of the spherical surface into the image. We need this factor because we are using a coordinate system on the hemisphere, but are seeking an average over the image of the hemisphere. If we include self-shadowed areas in the computation of the average, we must divide the integral by the whole area,  $\pi$ , of the disc that is the projection of the hemisphere, *on the other hand, if we do not include self-shadowed areas, we divide by the area  $(\pi/2)(1 + \cos\sigma_L)$  of the projection of the illuminated part of the hemisphere.*

Thus, from (C.2) and (C.4),

$$\begin{aligned} E(x) &= \lambda\mu E(\cos\psi) \\ &= \lambda\mu E(\cos\tau \cos(\sigma - \sigma_L)) \end{aligned} \quad (\text{C.6})$$

Here, to get the value of  $E(\cos\psi)$ , we need to evaluate the integral

$$B_1 = \int_{-\pi/2}^{\pi/2} \int_{-\pi/2 + \sigma_L}^{\pi/2} (\cos\eta \cos\psi) \cos\tau d\sigma d\tau \quad (\text{C.7})$$

$$= \int_{-\pi/2}^{\pi/2} \int_{-\pi/2+\sigma_L}^{\pi/2} (\cos\tau \cos\sigma)(\cos\tau \cos(\sigma-\sigma_L)) \cos\tau \, d\sigma d\tau \quad (\text{C.8})$$

$$= \int_{-\pi/2}^{\pi/2} \cos^3\tau d\tau \int_{-\pi/2+\sigma_L}^{\pi/2} \cos(\sigma-\sigma_L) \cos\sigma \, d\sigma \quad (\text{C.9})$$

$$= \frac{2}{3}(\sin\sigma_L + (\pi-\sigma_L)\cos\sigma_L) \quad (\text{C.10})$$

Therefore,

$$E(x) = \frac{2\lambda\mu}{3\pi}(\sin\sigma_L + (\pi-\sigma_L)\cos\sigma_L), \quad (\text{C.11})$$

or

$$E(x) = \frac{4\lambda\mu}{3\pi(1+\cos\sigma_L)}(\sin\sigma_L + (\pi-\sigma_L)\cos\sigma_L), \quad (\text{C.12})$$

depending on whether we average over all image regions, including self-shadowed parts, or not.

Similarly, to get the value of  $E(x^2)$ , we need to evaluate the integral

$$B_2 = \int_{-\pi/2}^{\pi/2} \int_{-\pi/2+\sigma_L}^{\pi/2} \cos\eta \cos^2\psi \cos\tau \, d\sigma d\tau \quad (\text{C.13})$$

$$= \int_{-\pi/2}^{\pi/2} \int_{-\pi/2+\sigma_L}^{\pi/2} (\cos\tau \cos\sigma)(\cos\tau \cos(\sigma-\sigma_L))^2 \cos\tau \, d\sigma d\tau \quad (\text{C.14})$$

$$= \int_{-\pi/2}^{\pi/2} \cos^4\tau d\tau \int_{-\pi/2+\sigma_L}^{\pi/2} \cos^2(\sigma-\sigma_L) \cos\sigma \, d\sigma \quad (\text{C.15})$$

$$= \frac{\pi}{8}(1+\cos\sigma_L)^2 \quad (\text{C.16})$$

Therefore,

$$E(x^2) = \frac{(\lambda\mu)^2}{8}(1+\cos\sigma_L)^2, \quad (\text{C.17})$$

or

$$E(x^2) = \frac{(\lambda\mu)^2}{4}(1+\cos\sigma_L), \quad (\text{C.18})$$

depending on whether we average over all image regions, including self-shadowed parts or not.

■

## REPORT DOCUMENTATION PAGE

Form Approved  
OMB No. 0704-0188

Public reporting burden for this collection of information is estimated to average 1 hour per response, including the time for reviewing instructions, searching existing data sources, gathering and maintaining the data needed, and completing and reviewing the collection of information. Send comments regarding this burden estimate or any other aspect of this collection of information, including suggestions for reducing this burden, to Washington Headquarters Services, Directorate for Information Operations and Reports, 1215 Jefferson Davis Highway, Suite 1204 Arlington, VA 22202-4302, and to the Office of Management and Budget Paperwork Reduction Project (0704-0188), Washington, DC 20503.

1. AGENCY USE ONLY (Leave blank)		2. REPORT DATE 1 Dec. 1990	3. REPORT TYPE AND DATES COVERED Interim Technical; Jan. 89 - Dec. 90	
4. TITLE AND SUBTITLE Modeling, Estimation and Pattern Analysis of Random Texture on 3D Surface			5. FUNDING NUMBERS  DAAL03-89-K-0032	
6. AUTHOR(S) Yoonsik Choe and R.L. Kashyap				
7. PERFORMING ORGANIZATION NAME(S) AND ADDRESS(ES) Purdue University School of Electrical Engineering West Lafayette, IN 47907			8. PERFORMING ORGANIZATION REPORT NUMBER	
9. SPONSORING / MONITORING AGENCY NAME(S) AND ADDRESS(ES) U. S. Army Research Office P. O. Box 12211 Research Triangle Park, NC 27709-2211			10. SPONSORING / MONITORING AGENCY REPORT NUMBER  ARO 26656.6-MA	
11. SUPPLEMENTARY NOTES The view, opinions and/or findings contained in this report are those of the author(s) and should not be construed as an official Department of the Army position, policy, or decision, unless so designated by other documentation.				
12a. DISTRIBUTION / AVAILABILITY STATEMENT  Approved for public release; distribution unlimited.			12b. DISTRIBUTION CODE	
13. ABSTRACT (Maximum 200 words) To recover 3-D structure from a shaded and textural surface image involving textures, neither the Shape-from-shading nor the Shape-from-texture analysis is enough, because both radiance and texture information coexist within the scene surface. A new 3-D texture model is developed by considering the scene image as the superposition of a smooth shaded image and a random texture image. To describe the random part, the orthographical projection is adapted to take care of the non-isotropic distribution function of the intensity due to the slant and tilt of a 3-D texture surface, and the Fractional Differencing Periodic (FDP) model is chosen to describe the random texture, because this model is able to simultaneously represent the coarseness and the pattern of the 3-D texture surface, and enough flexible to synthesize both long-term and short-term correlation structures of random texture. For estimating the parameters, a hybrid method which uses both the least square and the maximum likelihood estimates is applied and the estimation of parameters and the synthesis are done in frequency domain. Fractal scaling parameter plays a major role for classifying and/or segmenting the different texture patterns tilted and slanted due to the 3-dimensional rotation, because of its rotational and scaling invariant properties. A new classification method and a segmentation scheme for the 3-D rotated texture patterns is developed.				
14. SUBJECT TERMS Computer vision, texture, shape-from-shading, fractional model, pattern analysis			15. NUMBER OF PAGES 175	
			16. PRICE CODE	
17. SECURITY CLASSIFICATION OF REPORT UNCLASSIFIED	18. SECURITY CLASSIFICATION UNCLASSIFIED	19. SECURITY CLASSIFICATION OF ABSTRACT UNCLASSIFIED	20. LIMITATION OF ABSTRACT UL	